Title

Signal Detection and Analysis for Graviational Wave Astronomy

ISBN

9798288866333

Author

Leslie, Nathaniel Allen

Publication Date

2025-05-15

Peer reviewed|Thesis/dissertation

Signal Detection and Analysis for Graviational Wave Astronomy

by

Nathaniel Allen Leslie

A dissertation submitted in partial satisfaction of the

requirements for the degree of

Doctor of Philosophy

in

Physics

in the

Graduate Division

of the

University of California, Berkeley

Committee in charge:

Professor Liang Dai, Chair
Professor Uroš Seljak
Professor Adrian Lee

Spring 2025

Signal Detection and Analysis for Graviational Wave Astronomy

Abstract

Signal Detection and Analysis for Graviational Wave Astronomy

by

Nathaniel Allen Leslie

Doctor of Philosophy in Physics

University of California, Berkeley

Professor Liang Dai, Chair

I provide an introduction to the field of gravitational wave data analysis, including a summary of the history and future of gravitational wave detection, a derivation of wave solutions to the linearized Einstein equations, a discussion of observable parameters of the sources of gravitational waves, and a discussion of how gravitational waves create strain in Michelson interferometers and how that strain data is analyzed to extract those observable parameters. I present mode-by-mode relative binning, a new algorithm for fast and accurate likelihood estimation for gravitational waveform models with higher modes and precession effects. This method reduces the runtime of full parameter estimation from weeks to hours. I also discuss a new analytic gravitational waveform model for binaries undergoing small center-of-mass acceleration, including those in hierarchal triple systems. I present a Fisher analysis quantifying the detectability of this acceleration at various source chirp masses. Finally, I demonstrate how multi-messenger measurements of double white dwarf systems can be used to break the degeneracy between chirp mass and the impact of tides on orbital evolution. This can enable measurements of either tidal locking or moment of inertia of the white dwarfs without prohibitively expensive radial velocity measurements.

To my parents

who supported me, loved me unconditionally, and gave me the resources I needed to succeed.

To my teachers

who inspired me and exemplified the kind of inspiration I hope to pass on to the next generation.

To my friends

who have brought both wisdom and joy to my life.

To my sister, Danielle

who has made me laugh and helped me grow as a person.

To the love of my life, Miranda

who has been the perfect partner in every way.

Contents

List of Figures

List of Tables

Acknowledgments

I would like to thank Quentin Baghi, Biwei Dai, Jim Fuller, Lingyuan Ji, Minas Karamanis, Marius Millea, Jokob Robnik, Uroš Seljak, Peter Yoachim, and Winston Yin for discussions and assistance with the work in this thesis. I thank and recognize Geraint Pratten, Malcolm Lazarow, Kevin Burdge, and Liang Dai who made substantial contributions to the work in this thesis. I especially thank my advisor, Liang Dai, for his advice, encouragement, and support.

I acknowledge financial support from NSF Physics Frontier Center Award 202027, the Network for Neutrinos, Nuclear Astrophysics, and Symmetries (N3AS), National Science Foundation grant PHY-1630782, the Hearts to Humanity Eternal (H2H8) Graduate Research Grant, and many Graduate Student Instructor positions in the UC Berkeley Physics Department.

I would like to thank the instructors for whom I served as a Graduate Student Instructor: Marjorie Shapiro, Adrian Lee, Mike Zaletel, Hartmut Häffner, Austin Hedeman, Irfan Siddiqi, Holger Mueller, and Uroš Seljak, who have taught me so much about teaching. I especially thank Austin Hedeman, who has given me a great deal of advice, guidance, and support in my career aspirations. I also thank Uroš Seljak, who has trusted me with the opportunity to give lectures for his data science course, Bayesian Data Analysis and Machine Learning for Physical Sciences, which has given me invaluable experience.

I'd like to thank all of my friends for the fun, the memories, and the countless ways they have helped me grow throughout my academic journey. There are too many cherished friends to name them all here, but I'd like to acknowledge two friends whose support was essential for my graduate school success. I thank Winston Yin, a pillar of support and friendship as we embarked on very similar academic journeys, taking the same courses for the same research subfield, and leaving that subfield around the same time to work for the same advisor. I also thank Calvin Leung, who gave me the courage to switch fields, and always lifted me up whenever I felt discouraged.

I'd like to thank my parents, Ted and Keri Leslie, who always believed in my potential, and dedicated their lives to my success. They always supported me in any way that they could, and pushed me to learn and build my skills as long as I can remember, all while loving me unconditionally. They are the most instrumental assistants to my success. I'd also like to thank my sister, Danielle, who has grown alongside me, for always believing in me.

Finally, I'd like to thank my amazing fiancée Miranda for consistent support, encouragement, and cherished companionship. She has brought me untold happiness and satisfaction in my life, giving me the energy to succeed in whatever I put my mind to. She loves me just as much as I love her.

Chapter 1

Introduction

1.1 History and Future of Gravitational Wave Detection

For centuries, humans have used electromagnetic astronomy to learn about the universe. But in 2015, the LIGO (Laser Interferometry Gravitational-wave Observatory) collaboration began the era of gravitational-wave astronomy with the first direct detection of gravitational waves emitted by the merger of two black holes in an event known as GW150914 [118]. These detection of gravitational waves confirmed the predictions of Albert Einstein roughly a century earlier in 1916, when he showed that linearizing the field equations in his new theory of general relativity implied the existence of gravitational waves that travel at the speed of light [73, 74].

Over the next few decades following Einstein's prediction of gravitational waves, the mathematical theory of gravitational waves was refined, and by the early 1960s, linearized general relativity with the quadrupole approximation could be used to calculate the dynamics of orbiting binary systems that emitted gravitational waves [146, 145]. Later that decade, Joseph Weber was the first to try to experimentally detect gravitational waves by building massive resonant aluminum bars, now called Weber bars, and measuring small changes in their length [195]. While his initial papers claimed to detect a number of events, these detections turned out to be erroneous; the sensitivity of his detectors was far too weak to detect gravitational waves.

Around the same time, many discussed the possibility of using laser interferometry to detect gravitational waves, and prototypes were constructed, but none approached the necessary sensitivity. In 1979, the National Science Foundation funded Caltech and MIT to research and develop laser interferometers, which led to the founding of the LIGO project in 1984, which sought to build kilometer-scale Michelson-style interferometers to detect gravitational waves at sensitivities predicted by theory. Over the next two decades, the project expanded to the LIGO Scientific Collaboration, including the British/German GWO Collaboration, which was building GEO600, a 600 m long detector in Hannover, Germany [197].

In 2002, LIGO completed the construction of two 4 km long interferometers, one in Livingston Louisiana, and the other in Hanford, Washington. The two LIGO interferometers and GEO600 began coincident operation, but not yet at initial design sensitivity. In 2004, Advanced LIGO, a plan to improve sensitivity beyond the initial design was approved, and in 2006, LIGO achieved the initial design sensitivity. In 2007, the Virgo Collaboration began observing with the Virgo interferometer [14] in Pisa, Italy, entering a joint data analysis agreement with LIGO. Advanced LIGO was completed in 2014, and on September 14, 2015, LIGO Hanford and LIGO Livingston confirmed the first detection of gravitational waves from the merger of two black holes.

LIGO detected six more binary black hole mergers with the Hanford and Livingston detectors [116] before finally making a joint detection with Virgo on August 14, 2017 [7]. With three detectors, scientists were able to get a much tighter measurement of the sky location of the source, and they were able to test the nature of gravitational wave polarizations for the first time. But only three days later, LIGO and Virgo detected the closest and loudest event to date: a merger of two neutron stars [8]. Within 2 seconds, the Fermi Gamma-ray Burst Monitor independently detected a gamma-ray burst; the temporal and spacial alignment of the two events confirming that both were produced from the same event [5]. Because of the improved sky localization, an extensive observing campaign was immediately launched, discovering a kilonova transient signal only 11 hours later, also coming from the same source [9]. This multi-messenger event confirmed many predictions of GR, including demonstrating that gravitational waves travel at the speed of light with a fractional error less than 10^{-14}. Observing the merger of neutron stars also enabled us to place constraints on the equation of state of ultra-high density nuclear matter.

Today, nearly 100 events have been confirmed by the LIGO-Virgo-KAGRA collaboration, which has since added the Japanese KAGRA detector. The current observing run O4, which began in 2023, just announced that it has recorded over 200 more candidate events [116]. These include interesting events such as GW230529 [3], which detected a low mass black hole in the so-called "mass gap", where X-ray measurements had previously suggested no black holes existed [141, 75].

Thanks to these extraordinary discoveries, future larger and more sensitive detectors have been planned to make even more rapid discoveries. The U.S. plans to build a new scaled-up version of LIGO called Cosmic Explorer, with two 40 km interferometers, which will have dramatically enhanced sensitivity, and event rates up to millions per year [160]. The European community is preparing to design a 10 km triangular underground detector called the Einstein Telescope, which should have particularly high sensitivity at low frequencies, helping to better measure neutron star and mass-gap black hole events [38].

Just like we need different types of telescopes to observe the entire electromagnetic spectrum, we need different types of gravitational wave detectors to observe the entire gravitational wave spectrum. Kilometer-scale laser interferometers are only particularly sensitive in the $1\,\mathrm{Hz} - 1\,\mathrm{kHz}$ range. This allows for the detection of the mergers of black holes and neutron stars, but many other sources are believed to produce gravitational waves at different frequencies.

Before merger, binary systems of supermassive black holes (black holes $10^5 - 10^{10}$ times more massive than the Sun) emit strong gravitational waves in the nHz range, far too low frequency to be detected by LIGO. In 2023, the NANOGrav consortium has been able to detect a stochastic signal of these extremely low-frequency gravitational waves by analyzing correlations in a 15-year data set of pulsar burst times [16]. The signal is consistent with the expectations from a supermassive black hole background, but it could also be due to a more exotic cosmological source, such as the decay of topological defects formed during an early-universe phase transition [29].

Because white dwarfs have less mass than neutron stars or black holes, they do not reach high enough frequencies to be detected by kilometer-scale interferometers before they merge. To detect them, the interferometers would have to be much larger and more insulated from low-frequency sources of noise, like seismic noise. Space-based gravitational wave observatories like LISA (Laser Interferometer Space Antenna) [18] and Tianqin [123] plan to address both of these issues together. Both missions plan to launch a triangle of three spacecraft that direct lasers at each other and measure their phase, orbiting at astronomical distances (Tianqin: $\sqrt{3} \times 10^5$ km orbiting the Earth, LISA: 2.5×10^8 km orbiting the Sun behind the Earth's orbit). Both plan to measure the mHz-range gravitational waves emitted by the tens of millions of double white dwarf systems in the Milky Way, and potentially the mergers of supermassive black holes. Both have completed pathfinder missions, and both plan to complete and launch in the mid-2030s.

1.2 Gravitational Waves

1.2.1 Physics of Gravitational Waves

Gravitational waves are waves in a small perturbation $h_{\mu\nu}$ to the spacetime metric $g_{\mu\nu}$ away from the Minkowski (flat) spacetime metric $\eta_{\mu\nu}$. This relationship is shown in Equation 1.1.

$$g_{\mu\nu} = \eta_{\mu\nu} + h_{\mu\nu} \tag{1.1}$$

In general, the metric must be symmetric, so the perturbation $h_{\mu\nu}$ is also symmetric. We study these perturbations under conditions when they are very small ($|h_{\mu\nu}| \ll 1$), so that we may perform a first-order perturbative expansion on the equations of motion, neglecting terms of quadratic order and higher in $h_{\mu\nu}$. This is a reasonable approximation for the metric far from the source.

The equations of motion are the Einstein equations:

$$R_{\mu\nu} - \frac{1}{2} g_{\mu\nu} R = \frac{8\pi G}{c^4} T_{\mu\nu}, \tag{1.2}$$

which are derived by taking the variation of the gravitational action with respect to the metric. G is Newton's gravitational constant and c is the speed of light. $T_{\mu\nu}$ is the stress-energy tensor, which describes density and flux of energy and momentum of matter. The

Ricci tensor $R_{\mu\nu}$ and the Ricci scalar R are defined in terms of the metric through the Christoffel symbols $\Gamma^{\rho}_{\mu\nu}$ and the Riemann tensor $R^{\mu}_{\nu\rho\sigma}$:

$$\Gamma^{\rho}_{\mu\nu} = \frac{1}{2} g^{\rho\sigma}(\partial_{\mu} g_{\sigma\nu} + \partial_{\nu} g_{\sigma\mu} - \partial_{\sigma} g_{\mu\nu}), \tag{1.3a}$$

$$R^{\mu}_{\nu\rho\sigma} = \partial_{\rho}\Gamma^{\mu}_{\nu\sigma} - \partial_{\sigma}\Gamma^{\mu}_{\nu\rho} + \Gamma^{\mu}_{\alpha\rho}\Gamma^{\alpha}_{\nu\sigma} - \Gamma^{\mu}_{\alpha\sigma}\Gamma^{\alpha}_{\nu\rho}, \tag{1.3b}$$

$$R_{\mu\nu} = R^{\alpha}_{\mu\alpha\nu}, \tag{1.3c}$$

$$R = g^{\mu\nu} R_{\mu\nu}. \tag{1.3d}$$

If we substitute Equation 1.1 into the Einstein equations (Equation 1.2), drop all terms of quadratic order and higher in $h_{\mu\nu}$, and simplify, we can obtain the following result:

$$\Box \bar{h}_{\mu\nu} + \eta_{\mu\nu}\partial_{\alpha}\partial_{\beta}\bar{h}_{\alpha\beta} - \partial^{\alpha}\partial_{\mu}\bar{h}_{\nu\alpha} - \partial^{\alpha}\partial_{\nu}\bar{h}_{\mu\alpha} = -\frac{16\pi G}{c^4} T_{\mu\nu}, \tag{1.4}$$

where $\Box = \partial^{\mu}\partial_{\mu}$ is the d'Alembertian operator and we define

$$\bar{h}_{\mu\nu} = h_{\mu\nu} - \frac{1}{2}\eta_{\mu\nu} h, \tag{1.5a}$$

$$h = \eta^{\mu\nu} h_{\mu\nu}. \tag{1.5b}$$

In general relativity, we have the freedom to choose coordinates in which to describe our system. Specifically, the theory of general relativity is invariant under a diffeomorphic coordinate transformation, i.e. a differentiable bijection with a differentiable inverse. We can simplify Equation 1.4 by performing such a diffeomorphism:

$$x^{\mu} \to x'^{\mu}(x), \tag{1.6}$$

which performs the following transformation to the metric:

$$g_{\mu\nu}(x) \to g'_{\mu\nu}(x') = \frac{\partial x^{\rho}}{\partial x'^{\mu}} \frac{\partial x^{\sigma}}{\partial x'^{\nu}} g_{\rho\sigma}(x). \tag{1.7}$$

We can greatly simplify Equation 1.4 by judiciously choosing such a specific diffeomorphism or *gauge fixing*. If we define this diffeomorphism in terms of a coordinate-dependent coordinate shift $\xi^{\mu}(x)$:

$$x^{\mu} \to x'^{\mu} = x^{\mu} + \xi^{\mu}(x), \tag{1.8}$$

then we can transform the following term, which appears as a part of Equation 1.4:

$$\partial^{\nu}\bar{h}_{\mu\nu} \to \left(\partial^{\nu}\bar{h}_{\mu\nu}\right)' = \partial^{\nu}\bar{h}_{\mu\nu} - \Box\xi_{\mu}. \tag{1.9}$$

Let the value of this term in some initial coordinates be $f_{\mu}(x) = \partial^{\nu}\bar{h}_{\mu\nu}$. We can make this term vanish by choosing the following solution for ξ_{μ}:

$$\xi_\mu(x) = \int d^4y\, G(x-y)\, f_\mu(y), \tag{1.10}$$

where $G(x)$ is a Green's function of the d'Alembertian operator, i.e. it satisfies

$$\Box_x G(x-y) = \delta^4(x-y). \tag{1.11}$$

This transformation is referred to as fixing to the Lorentz gauge [125]. After this transformation, because $\partial^\nu \bar{h}_{\mu\nu} = 0$, three terms on the left hand side of Equation 1.4 vanish (note that $h_{\mu\nu}$ is symmetric), giving us a wave equation for gravitational waves:

$$\Box \bar{h}_{\mu\nu} = -\frac{16\pi G}{c^4} T_{\mu\nu}. \tag{1.12}$$

The Lorentz gauge condition removes 4 degrees of freedom from $h_{\mu\nu}$, but it doesn't fully fix the gauge, as Green's functions of the d'Alembertian operator are not unique. Outside the source, where $T_{\mu\nu} = 0$, we have the following free space wave equation:

$$\Box \bar{h}_{\mu\nu} = 0. \tag{1.13}$$

In this region, we are able to remove 4 more degrees of freedom by imposing the *transverse-traceless gauge*:

$$h^{\mu 0} = 0, \quad h^i_i = 0, \quad \partial^i h_{ij} = 0. \tag{1.14}$$

where i and j strictly refer to spatial components of the metric perturbation [125]. Note that the second condition, which sets the trace of $h_{\mu\nu}$ to zero, makes $\hat{h}_{\mu\nu} = h_{\mu\nu}$. A general symmetric $h_{\mu\nu}$ has 10 degrees of freedom, and fixing the Lorentz gauge reduces to 6 degrees of freedom. In this gauge, we are left with two degrees of freedom, which correspond to two polarizations of gravitational waves.

The solutions to Equation 1.13 are plane waves that propagate at the speed of light:

$$h_{\mu\nu}(x) \propto e^{i(\vec{k}\cdot\vec{x}-\omega t)}, \tag{1.15}$$

where $\omega = c|\vec{k}|$.

When we apply the transverse-traceless gauge conditions, the third condition of Equation 1.14 forces the tensor coefficients of these plane waves to be perpendicular to the direction of propagation. For example, if we choose $\vec{k}$ to be in the $\hat{z}$ direction, then the solution is a two-polarization gravitational wave traveling in the z direction:

$$h_{\mu\nu} = \begin{pmatrix} 0 & 0 & 0 & 0 \\ 0 & h_+ & h_\times & 0 \\ 0 & h_\times & -h_+ & 0 \\ 0 & 0 & 0 & 0 \end{pmatrix} e^{(i(\frac{\omega}{c}(z-ct))}, \tag{1.16}$$

where we take the real part for a physical wave.

1.2.2 Sources of Gravitational Waves

In this section, we will analyze a simplified treatment of the sources of gravitational waves, highlighting the key properties of the gravitational waves and how they depend on properties of the source. From the context of data analysis, knowing those key properties in observed gravitational waves makes the corresponding properties of the source observable.

Near the sources of gravitational waves, Equation 1.1 with $|h_{\mu\nu}| \ll 1$ is not a reasonable approximation, and the Einstein equations (Equation 1.2) are too difficult to solve analytically. To understand the physics of the sources of these gravitational waves, we take a number of approaches. They can either be solved numerically [152, 50, 24] or via perturbative expansion, like the post-Newtonian scheme [33, 82], which is perturbative in a parameter $\epsilon^2 \sim (v/c)^2 \sim \Phi/c^2$, where v is the typical velocity of an object in the system, and Φ is the Newtonian potential. The lowest order post-Newtonian expansion gives the *quadrupole formula*, the simplest expression for the amplitude of a gravitational wave [169, 52]:

$$h_{jk} = \frac{2G}{c^4 r}\frac{d^2 Q_{jk}}{dt^2}, \tag{1.17}$$

where r is the distance from the source and Q_{ij} is the mass quadrupole or the second moment of the mass distribution defined as

$$Q_{jk} = \int \rho(x)\,[x_j x_k - \frac{1}{3}\delta_{ij} r^2]\, d^3x. \tag{1.18}$$

From this formula, one can work out that gravitational waves are primarily generated by dynamic mass quadrupoles, or two massive objects moving around each other. We can learn some key features of gravitational radiation by calculating this amplitude for a simple system of two masses orbiting each other in a circular orbit in the xy-plane with angular frequency Ω_{orb}, depicted in Figure 1.1. This treatment neglects travel-time effects, and it only handles a specific case, but many of the conclusions do generalize.

If the initial configuration is given in Figure 1.1, then mass 1 is at position $\vec{x}_1 = (d_1\cos(\Omega t), d_1 \sin(\Omega t))$ and mass 2 is at position $\vec{x}_2 = (-d_2\cos(\Omega t), -d_2\sin(\Omega t))$. Substituting these positions for point masses m_1 and m_2 into Equations 1.17 and 1.18, we obtain the following expression for the gravitational wave:

$$h_{\mu\nu} = -\frac{4G\mu d^2 \Omega_{\mathrm{orb}}^2}{c^4 r}\begin{pmatrix} 0 & 0 & 0 & 0 \\ 0 & \cos(2\Omega_{\mathrm{orb}} t) & \sin(2\Omega_{\mathrm{orb}} t) & 0 \\ 0 & \sin(2\Omega_{\mathrm{orb}} t) & -\cos(2\Omega_{\mathrm{orb}} t) & 0 \\ 0 & 0 & 0 & 0 \end{pmatrix}, \tag{1.19}$$

where $\mu = \frac{m_1 m_2}{m_1+m_2}$ is the reduced mass of the system.

Note the similarity with Equation 1.16. One key point is that the gravitational wave's frequency is twice the orbital frequency: $\Omega_{\mathrm{GW}} = 2\Omega_{\mathrm{orb}}$. We can also determine the amplitude of these gravitational waves.

As an intriguing exercise, we can investigate the feasibility of generating detectable man-made gravitational waves. Let's consider a case of two equal mass objects being rotated

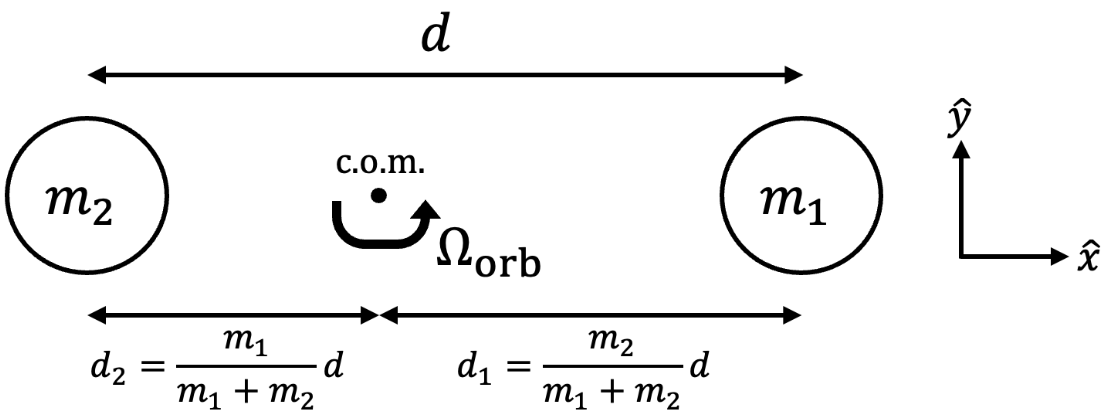

Figure 1.1: A depiction of two masses m_1 and m_2 orbiting each other.

around each other in a centrifuge-like machine. We would need large masses spun at high frequency separated by a large distance. We can limit how small r can be by requiring that we measure in the far-field regime, where $r \gtrsim \lambda \sim \frac{2\pi c}{\Omega_{\text{GW}}} = \frac{\pi c}{\Omega_{\text{orb}}}$.

We can compute the result for a very extreme case. If we take two aircraft carriers ($m \sim 10^9\,\text{kg}$) at a distance of 1 km and spin them at 1000 Hz, we get

$$h \sim 4.3 \times 10^{-27} \left(\frac{m}{10^9\,\text{kg}}\right)\left(\frac{d}{1\,\text{km}}\right)^2\left(\frac{f}{1\,\text{kHz}}\right)^3. \tag{1.20}$$

Even this extreme scenario is too weak to detect, it's about a million times weaker than GW150914 was when the signal reached Earth. One might instead consider astrophysical binaries, which orbit each other gravitationally. Using Kepler's 3rd law, the distance between them is determined by their mass and orbital frequency: $d = (GM/\Omega_{orb}^2)^{1/3}$. Substituting this into the amplitude in Equation 1.19 gives

$$h \sim \frac{(G\mathcal{M})^{5/3}}{c^4 r}\Omega_{orb}^{2/3}, \tag{1.21}$$

where the *chirp mass* $\mathcal{M}$ is defined as

$$\mathcal{M} = \frac{(m_1 m_2)^{3/5}}{(m_1 + m_2)^{1/5}}. \tag{1.22}$$

We see that the largest gravitational waves come from extremely massive objects orbiting at high frequency, so they must be the densest objects in the universe–compact remnants of stars, such as white dwarfs, neutron stars, and black holes. We can also see that the lowest order gravitational wave amplitude depends on a composite mass parameter $\mathcal{M}$ called the chirp mass. The amplitude also determines the energy carried away by the gravitational waves, and therefore the rate of orbital decay of the source system, so this quantity is the primary mass observable in gravitational wave parameter estimation, which we discuss further in Section 1.3.

1.2.3 Detection of Gravitational Waves

In this section, we discuss the detection of gravitational waves through ground-based L-shaped Michelson interferometers such as LIGO and Virgo. Triangle-shaped detectors like LISA, Tianqin, and Einstein Telescope plan to operate slightly differently, but they are conceptually similar.

Recall that a gravitational wave is made up of two polarizations, h_+ and $h_\times$. Through inspection of Equation 1.16, we can see that the h_+ polarization distorts the metric, causing x distances to increase while y distances decrease and vice versa. If one performs a basis change, one could see that the $h_\times$ polarization performs this effect on the $\hat{x} + \hat{y}$ and $\hat{x} - \hat{y}$ directions: the same effect rotated by 45°. This effect is visualized in Figure 1.2.

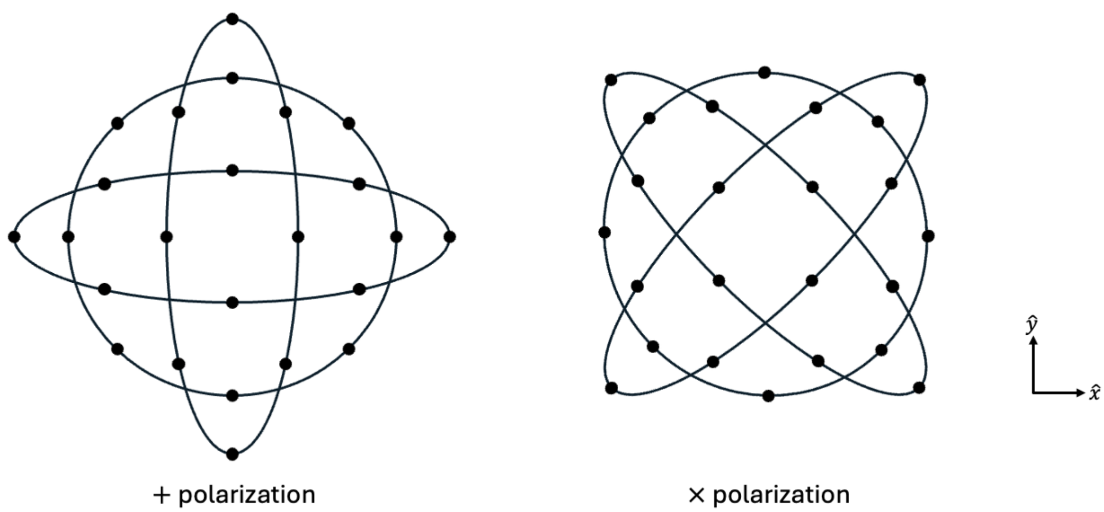

Figure 1.2: A depiction of the effect of plus (left) and cross (right) polarizations of a gravitational wave with exaggerated amplitude on a ring of particles in free fall. The ring of particles, which is perfectly circular in flat space, is compressed and stretched back and forth as a gravitational wave passes.

A Michelson interferometer, shown in Figure 1.3, is able to detect this effect on much smaller scales by comparing the length of its two arms. For LIGO, the arms are 4 km long. As a gravitational wave passes by, it will increase the travel time of the light down one of the arms relative to the other and produce an interference pattern.

By measuring the interference pattern, the interferometer is able to measure the relative difference in arm length, called the strain:

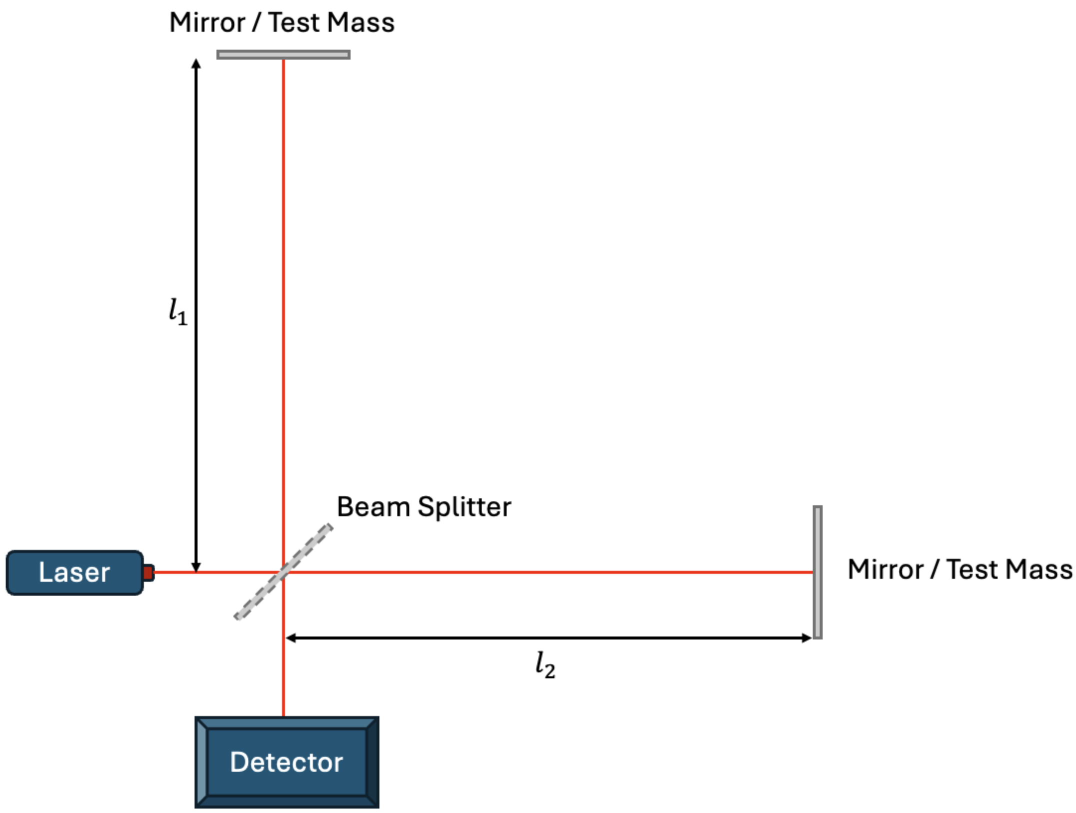

Figure 1.3: A diagram of a Michelson interferometer. A laser beam is split into two by a beam splitter, and the two streams travel back and forth down long arms and are merged back together to form an interference pattern in a detector. The interference pattern is sensitive to small relative changes in arm length, which are caused by gravitational waves.

$$h = \frac{l_2 - l_1}{L}, \tag{1.23}$$

where L is the rest length of each arm and l_1 and l_2 are the lengths of each arm.

With some geometric calculation, one can work out that the strain produced by gravitational waves is a linear combination of the two gravitational wave polarizations, with coefficients F_+ and $F_\times$, which are called the detector response coefficients.

$$h = F_+ h_+ + F_\times h_\times \tag{1.24}$$

The detector response coefficients depend on the orientation of the interferometer relative to the source and the axes that define the polarizations. This means the sensitivity of the detector depends on geometry, and these detectors actually have blind spots. These detectors are maximally sensitive to gravitational waves traveling perpendicular to the plane of the detector, and they are entirely insensitive to gravitational waves traveling directly in the plane of the detector parallel to the beam splitter as shown in Figure 1.3. For this reason, gravitational wave detectors are built with different orientations.

1.3 Gravitational Wave Data Analysis

Strain data contains information about the astrophysical sources that produced the gravitational wave, and proper data analysis allows us to extract the properties of those sources. We can infer the parameters of a source through the process of Bayesian inference.

1.3.1 Bayesian Inference

General relativity allows us to predict how gravitational waves will affect the detector strain, but unfortunately, we cannot measure that directly. Real data is contaminated by noise, making our measurements imprecise, so our true knowledge of the parameters of gravitational waves will be a probability distribution. We would like a probability of parameters Θ given the data d, but that is impossible to model. But with models for a signal and noise, we can compute the probability of the data d given parameters Θ. If we would like to reverse a conditional probability, we want to use Bayes theorem:

$$P(\Theta|d) = \frac{P(d|\Theta)P(\Theta)}{P(d)}. \tag{1.25}$$

The denominator $P(d)$, often called the marginal probability, can be computed by integrating the numerator over all parameter values: $P(d) = \int P(d|\Theta)P(\Theta)d^n\Theta$, but in practice, this term is often just an irrelevant normalization constant. The term $P(\Theta)$ captures our previous beliefs about what values Θ takes on, so $P(\Theta)$ is called the prior probability or just the prior. $P(\Theta|d)$ describes the probability distribution after we have learned or updated from the data, so it is called the posterior. Finally, we call $\mathcal{L} = P(d|\Theta)$ the *likelihood*.

The prior is a seemingly arbitrary, but necessary piece of Bayesian inference. Oftentimes there are symmetry arguments that justify an expression for the prior, like orienting the direction of orbit of a black hole binary uniformly on a sphere, but some have theoretical prior distributions, like the black hole masses, about which we are still learning [3]. The prior choice impacts the posterior, and this is an important aspect of Bayesian inference to study [55].

For gravitational wave data, the posterior cannot be analytically computed for all values of Θ. Instead, the goal is to compute a set of samples drawn from the posterior distribution. If we have a good measurement, then the posterior tends to be essentially zero everywhere except for a small region localized near the "true" value of the parameters. Gathering samples usually requires using a sampling algorithm that explores a high-dimensional parameter space extensively, yet efficiently, accepting and rejecting samples until a few thousand are obtained.

The only remaining piece is the likelihood $\mathcal{L} = P(d|\Theta)$. Evaluating the likelihood requires a model for the signal, which allows us to extract the information about the parameters. The simplified low-order model discussed above in Section 1.2.2 gives polarizations that depend on distance to the source, chirp mass, and orbital frequency. The detector response coefficients in Equation F_+ and $F_\times$ depend on sky location and source orientation.

Actual data analysis uses more sophisticated models that allow us to measure more parameters more precisely. As mentioned earlier, more sophisticated models solve the Einstein equations in more detail. But because they need to be evaluated for many different parameters while a sampler maps the posterior, they need to be relatively fast to compute. Full numerical relativity simulations are far too costly, but there are many approximate models that can be evaluated extremely quickly. These include the Taylor family, which uses the post-Newtonian expansion described briefly in Section 1.2.2 [44], the effective one-body (EOB) family, which maps the two-body system into a single test particle moving in an effective external metric [43, 68, 138], and the Phenom family, which combines post-Newtonian expansions with interpolations of numerical relativity solutions [103, 121, 150].

We will derive an explicit formula for the likelihood in Section 1.3.4. This also requires a description of the noise, which we will discuss in Section 1.3.2.

1.3.2 Stationary Gaussian Noise

Michelson interferometer style detectors each gather a time series of strain data $h(t)$ while they are operational. This data is gathered at some sampling rate F_s, which is 4096 Hz for LIGO. The strain data does not purely measure the effect of gravitational waves, as the strain is also impacted by many noise sources, including shot noise from photon detection, seismic noise, and thermal noise in detector elements [2]. There are also transient "events" or "glitches" of noise of known and unknown origin [4, 48]. This noise $n(t)$ gets added to the true gravitational wave signal $h(t)$ to produce the measured strain data $d(t)$:

$$d(t) = h(t) + n(t). \tag{1.26}$$

In order to analyze this data, we often would like to better understand the nature of the noise. Often, a few simplifying assumptions are made. The first is that the noise is Gaussian, or that it follows a multivariate Gaussian distribution: $n(t) \sim \mathcal{N}(0, \mathbf{C})$, with zero mean and some covariance $\mathbf{C}$. The second assumption is that the noise is stationary, meaning the noise covariance only depends on the time delay between two times. This also means that the covariance, which fully characterizes the data distribution, is unaffected by a time shift:

$$C_{ij} = \langle n(t_i)n(t_j)\rangle = \langle n(t_i + \tau)n(t_j + \tau)\rangle. \tag{1.27}$$

If we don't expect the statistical properties of the noise sources to change as time goes on, this is a good assumption. These two assumptions are not exactly correct, and better detection can be done with non-Gaussian, non-stationary data modeling [207]. But for this work, we will use this simpler model, which models the noise pretty well.

With Gaussian and stationary noise, it is usually preferred to analyze systems in the frequency domain, where the noise covariance is diagonal. To transform a time series, say $d(t)$, to the frequency domain, we analyze a specific chunk of data of length T. Because the data is sampled at sampling frequency F_s, there are $N_{\mathrm{FFT}} = T \cdot F_s$ data points $d(t_j)$ at times $t_j = j/F_s$ for $j = 0, 1, ..., N_{\mathrm{FFT}} - 1$. We get the corresponding frequency series data $\tilde{d}(f_k)$ by performing a discrete Fourier transform:

$$\tilde{d}(f_k) = \frac{1}{F_s} \sum_{j=1}^{N_{\mathrm{FFT}}} d(t_j) e^{-2\pi i f_k t_j}, \tag{1.28}$$

where the frequencies are $f_k = k/T$ for $k = 0, 1, ..., N_{\mathrm{FFT}} - 1$. By direct substitution into Equation 1.28, one can show that $\tilde{d}(F_s - f_k) = \tilde{d}(f_k)^*$, so we only need to save the first half of the values up to the Nyquist frequency $F_s/2$ to provide complete information. Here we explicitly include a tilde to denote a corresponding frequency domain series, but for the rest of this work, we will implicitly assume that functions of f are the frequency domain counterparts.

In the frequency domain, the Gaussian and stationary noise at each frequency is an independent one-dimensional Gaussian variable, whose real and imaginary parts follow the same distribution:

$$\mathfrak{Re}\{n(f)\}, \mathfrak{Im}\{n(f)\} \sim \mathcal{N}(0, \frac{T}{4} S_n(f)), \tag{1.29}$$

where $S_n(f)$ is called the Power Spectral Density (PSD) of the noise. One can estimate the PSD by using Welch's method.

1.3.3 Estimating a PSD with Welch's Method

To use Welch's method, you need to collect multiple segments of data without a detectable signal. As most of the data in LIGO does not contain detectable signal, you can just break a long segment of data into n chunks. Without signal, you just have multiple realizations of noise, which you can transform into the frequency domain using Equation 1.28:

$$\{n_i(t)\}_{i=1,\dots,n} \underset{\mathrm{FFT}}{\rightarrow} \{n_i(f)\}_{i=1,\dots,n}. \tag{1.30}$$

By computing the magnitude squared of these and averaging over the n chunks, you can get a good estimate of the average power (amplitude squared) of the noise at each frequency:

$$\langle |n(f)|^2 \rangle \approx \sum_{i=1}^{n} |n_i(f)|^2. \tag{1.31}$$

From Equation 1.29, we know that

$$\begin{aligned}\langle|n(f)|^2\rangle &= \left\langle \mathfrak{Re}\{n(f)\}^2 \right\rangle + \left\langle \mathfrak{Im}\{n(f)\}^2 \right\rangle \\ &= \frac{T}{2} S_n(f),\end{aligned} \tag{1.32}$$

as $\left\langle \mathfrak{Re}\{n(f)\} \right\rangle = \left\langle \mathfrak{Im}\{n(f)\} \right\rangle = 0$. So Welch's method gives

$$S_n(f) \approx \frac{2}{T} \sum_{i=1}^{n} |n_i(f)|^2. \tag{1.33}$$

1.3.4 Gravitational Wave Likelihood

With this PSD, which we can calculate, we are able to evaluate the explicit *likelihood* or probability that a data set $d(f)$ would arise given a true underlying signal $h(f)$. We just evaluate the Gaussian PDF for the noise as described in Equation 1.29:

$$\begin{aligned}P(d(f)|h(f)) = \mathcal{L} &= \prod_f \left[\frac{4}{\sqrt{2\pi} T S_n(f)} \exp\left(-\frac{(\mathfrak{Re}\{d(f)\} - \mathfrak{Re}\{h(f)\})^2}{\frac{T}{2} S_n(f)} \right) \right] \\ &\quad \times \left[\frac{4}{\sqrt{2\pi} T S_n(f)} \exp\left(-\frac{(\mathfrak{Im}\{d(f)\} - \mathfrak{Im}\{h(f)\})^2}{\frac{T}{2} S_n(f)} \right) \right] \\ &= \prod_f \frac{8}{\pi T^2 S_n^2(f)} \exp\left(-\frac{|d(f) - h(f)|^2}{\frac{T}{2} S_n(f)} \right),\end{aligned} \tag{1.34}$$

where the sum is performed over all independent frequencies up to the Nyquist frequency $f_{\mathrm{Nyq}} = F_s/2$. It is often preferred to work with the natural logarithm of this likelihood:

$$\ln \mathcal{L} = \sum_f -\frac{|d(f) - h(f)|^2}{\frac{T}{2} S_n(f)} + \ln \mathcal{L}_0, \tag{1.35}$$

where $\ln \mathcal{L}_0$ is an often neglected term that does not depend on $h(f)$ or $d(f)$. We will drop this term from now on. We often write this likelihood in terms of inner products in the following way:

$$\ln \mathcal{L} = -\frac{1}{2}\langle d|d\rangle + \langle d|h\rangle - \frac{1}{2}\langle h|h\rangle, \tag{1.36}$$

where the inner product is defined as

$$\langle a|b\rangle = \sum_f \frac{a^*(f) b(f)}{\frac{T}{4} S_n(f)}. \tag{1.37}$$

Usually we also drop the $-\frac{1}{2}\langle d|d\rangle$ term in the log likelihood because it doesn't depend on the signal h, so we finally get

$$\ln \mathcal{L} = \langle d|h\rangle - \frac{1}{2}\langle h|h\rangle. \tag{1.38}$$

Finally, if you have multiple independent detectors (or independent channels in a triangular detector), the likelihood is the product of the individual likelihoods for each detector (channel), so the full log likelihood comes from summing Equation 1.38 over all detectors (channels). With this likelihood, a prior $P(\Theta)$, a waveform model $h(\Theta)$, and gravitational wave data d, one can use a sampler to gather posterior samples using Equation 1.25, and constrain the parameters of the source that produced that data.

1.4 New Work in this Thesis

The remainder of this thesis covers new work in the field of gravitational wave data analysis. Each chapter covers a different topic in a generally self-contained manner, so they may be read independently.

Chapter 2 [114] concerns the method of mode-by-mode relative binning, a new method for calculating fast and accurate likelihoods for specialized waveforms. As mentioned above in Section 1.3.1, Bayesian inference requires a large number of likelihood evaluations to produce posteriors, which means the likelihoods must be fast to produce posteriors in a reasonable amount of time. Evaluating the likelihood in Section 1.3.4 can be prohibitively slow, so approximate methods exist to speed up the evaluation, and these methods need to retain accuracy in order to produce accurate posteriors. One such method is known as relative binning [205], which allows for fast and accurate likelihood estimation for quadrupolar waveform models that do not model the effects of spin-orbit precession.

The original relative binning method provides extremely inaccurate likelihoods when used on models with precession and higher modes because a key assumption of the original relative binning method is not correct. The original relative binning method assumes that the ratio of two waveforms that share similar parameters is smooth in frequency space, and uses a piecewise linear interpolant for that ratio. When a waveform includes more than the quadrupole mode, which is necessary for modeling precession, this assumption is no longer correct. Instead mode-by-mode relative binning develops a few schemes for applying this piecewise linear interpolant to each mode separately. Chapter 2 provides the details of these schemes, demonstrating the improved speed and accuracy on a variety of real and mock data.

Chapter 3 [112] concerns a new gravitational waveform model for a binary system whose center of mass is accelerating. This is the case in a hierarchical triple system, where two tightly bound compact objects are orbiting a distant third body. Our model falls into the "Taylor" family of gravitational waveform models, but we include the impact of the acceleration of the source to first order, with the wave phase computed to 3rd post-Newtonian order. We investigate the conditions under which our first-order perturbative treatment of the acceleration is accurate and we perform a Fisher analysis to quantify the detectability of acceleration in next generation gravitational wave detectors.

Chapter 4 [113] concerns tidal effects on the evolution of binary systems of double white dwarfs. Double white dwarf systems will be detectable both through visible light optical astronomy [110, 111] and future space-based gravitational wave detectors [18, 123, 107]. Chapter 4 explains how multi-messenger data analysis, that is, an analysis including both optical-band lightcurve data and gravitational wave data, will allow us to gain unique insights into both white dwarf structure and the impact of tides on orbital evolution.

With only photometric data, there is a measurement degeneracy between the system's chirp mass and the impact of tides upon the first derivative of orbital frequency. We investigate a number of ways of breaking this degeneracy with and without using gravitational wave data, considering both broad sky surveys and focused high cadence observations on the EM side. We test the feasibility of these approaches on multi-messenger mock data based on real observations.

Chapter 2

Mode-by-mode Relative Binning

2.1 Introduction

Astrophysical information about gravitational wave sources is commonly extracted via parameter inference within the Bayesian framework. This process requires thorough sampling of a high-dimensional parameter space (e.g. with a total of 10–15 source parameters), and hence a huge number (typically on the order of 10^7–10^8) of likelihood evaluations. To map either the likelihood function or the posterior distribution, it is important to accurately evaluate the likelihood function on manageable timescales.

Brute-force calculation of the likelihood is often costly. In order to be compatible with Fast Fourier Transform (FFT), it requires evaluating the frequency-domain model waveform on a uniformly sampled, sufficiently fine grid that has $\sim T\,f_{\mathrm{max}}$ frequencies, where f_{max} is the highest frequency that includes information and T is the duration of the gravitational wave signal in the sensitive frequency band of the detector. The computational cost can be especially prohibitive if T is long or if f_{max} is large. Even non-uniform frequency sampling still requires a large number of grid points, as the waveform phase typically evolves over a large number of cycles across the sensitive frequency band. For GW parameter inference with sophisticated waveform models, model calls at individual frequencies often dominate the runtime. For many frequency domain waveform models, the computational time of a likelihood evaluation scales nearly linearly with the number of queried frequencies [51].

A number of methods have been developed to approximate the likelihood with fewer frequency evaluations, trading an insignificantly amount of accuracy degrade for substantial speedup. Reduced order quadrature (ROQ) [51] is one such method, which pre-computes a reduced basis for a given waveform model, and approximates any physical waveform with an interpolant in the linear space spanned by this basis. This method only needs as many independent evaluations as there are basis elements, and has been applied to reduce the computational time of a variety of waveform models [179, 155, 178, 131].

Relative binning [205, 67, 78], originally developed for non-precessing waveforms in the dominant (2, 2) radiation mode, is another method to achieve the same goal. In relative binning, the *ratio* between a given waveform and an appropriately chosen fiducial waveform is considered. If the fiducial waveform is a decent fit of the data, only waveforms that resemble the fiducial one need to be examined in parameter inference, for which the waveform ratio conveniently has a milder frequency dependence. For this reason, the waveform ratio can be well approximated as a piecewise-linear function in the frequency domain, which only requires waveform model calls at the edges of a reduced number of frequency bins.

For simple waveform models with only one harmonic such as `IMRPhenomD` [103], this method has been shown to require fewer waveform evaluations than ROQ for the same error tolerance [205], and has been routinely used in independent analysis of public LIGO/Virgo data [208, 193, 163, 164, 137]. An earlier and somewhat similar method referred to as heterodyne, which also samples the ratio between two waveforms using fewer grid points, was proposed in Ref. [62].

Many gravitational wave sources carry a strong imprint of the effects of precession of the orbital plane, which are neglected in simpler models like `IMRPhenomD`. These precession effects are often accounted for by effective precession parameters that well approximate the effects with minimal additional complexity or dimensionality [172, 85, 187]. However, more sophisticated waveform models that fully incorporate the effects of spin-orbit precession with misaligned spins and higher harmonic modes [93, 104, 150, 138, 192] have begun to be widely applied in parameter inference. Compared to many of the non-precessing models, which only incorporate the dominant (2, 2) radiation mode, these advanced models have yielded better fits to numerical simulations [84], better fits to the detected LIGO/Virgo gravitational wave signals [56], higher SNR, more precision, and more accuracy in parameter estimation for injected signals [100, 176, 89], and in some cases have led to the intriguing discovery of new solutions [127, 11, 58, 136].

Additionally, information in higher modes is crucial in tracking the recoil kicks of the GW sources [49], and this information should be reliably extractable once LIGO/Virgo reach their design sensitivities [191].

In the original implementation of relative binning presented in Ref. [205], the key assumption is that the ratio between a waveform under examination over a fiducial one has significantly smoother frequency dependence than the waveform themselves do. The quality of this assumption however degrades for precessing waveforms with the full symphony of harmonics, as both the precession-induced wobbling of the binary orbital plane and the superposition of multiple harmonics give rise to additional oscillations with the frequency in the observed waveform. It is pivotal to realize that a precessing waveform can be decomposed into a linear combination of contributions from individual radiation harmonics in the co-precessing frame [173], and our schemes deal with ratios evaluated for these modes individually and hence only have to sample functions that are smoother in the frequency space. Our scheme builds a likelihood from piecewise linear interpolants of these smooth quantities. As an explicit example, we demonstrate this strategy using the phenomenological waveform model `IMRPhenomXPHM` [150, 84, 151].

In this chapter, we present two improved relative binning schemes specially designed for precessing waveforms with multiple harmonics, which we jointly refer to as the Mode-by-mode Relative Binning (MRB). We give explicit formulae to approximate the likelihood, and we introduce practical algorithms to choose appropriate frequency bins. We find theoretical speedup of MRB relative to the original relative binning method by up to an order of magnitude, which is due to a reduced number of frequency bins required, for the same tolerable *absolute* accuracy ~ 0.1 in the log likelihood.

The rest of the chapter is organized as follows. In Section 2.2, we review the "twisting-up" procedure for building precession waveforms and introduce the basic definitions that will be used in the MRB schemes. In Section 2.3, we present the technical details of the two MRB schemes, including introducing piecewise linear approximation for quantities that are smooth functions of the frequency, as well as new methods to optimize the frequency bins. In Section 2.4, we study the required number of frequency bins as a function of accuracy tolerance by applying MRB to real and injected gravitational wave signals, with a comparison to the old relative binning method without using mode decomposition. Finally, we provide discussion of our results in Section 2.5 and concluding remarks in Section 2.6.

2.2 Mode Decomposition for Precessing Waveforms

To understand how relative binning can be best applied to waveforms that describe precessing binary systems, we start by discussing the general structure of precessing waveforms. Many precessing models with higher modes are built using an approximate mapping from a non-precessing system to a precessing system, often referred to as the "twisting-up" procedure [173, 171]. This includes state-of-the-art phenomenological [104, 150] and effective one body [138] waveform models. Under the twisting-up scheme, the non-precessing waveforms resemble the gravitational radiation emitted by a non-precessing source, as if an imaginary observer is fixed relative to the wobbling orbital plane of the binary [173].

The specific prescription for twisting-up the non-precessing waveforms that we use is developed in [171] and is fully detailed for the `IMRPhenomXPHM` model in [150]. Here, we note the most important aspects of this prescription that will allow us to explain our schemes. A general waveform model outputs the frequency domain waveform of both polarizations, i.e. $h_+(f)$ and $h_\times(f)$. Models that use the twisting-up procedure include a prescription for a non-precessing waveform as what a fictitious observer would see in the co-precessing frame. This non-precessing waveform can be decomposed into building blocks, $h^L_{\ell,m'}(f)$, following the spin-weighted spherical harmonic expansion. Since the binary orbital timescale is typically significantly shorter than the timescale of spin-orbit precession, the precession effects on the waveform can be well captured by a time-dependent Euler rotation of the non-precessing waveform [171]. After transforming from the time domain into the frequency domain under the stationary phase approximation, the model also provides three frequency-dependent Euler angles, $\alpha(f)$, $\beta(f)$ and $\gamma(f)$, which parameterize a rotation from the frame co-precessing with the orbital angular momentum vector (the L-frame) to the approximately inertial frame defined by the total angular momentum vector (the J-frame). Using the definitions introduced in Ref. [150], it is a straightforward derivation that both polarizations can be expressed as a linear combination of the L-frame modes $h^L_{\ell,m'}$. We follow their convention that m is used to label the J-frame modes, and m' is used to label the L-frame modes.

$$h_+(f) = \sum_{\ell,m'} C^+_{\ell,m'}(f)\, h^L_{\ell,m'}(f), \tag{2.1a}$$

$$h_-(f) = \sum_{\ell,m'} C^\times_{\ell,m'}(f)\, h^L_{\ell,m'}(f). \tag{2.1b}$$

Often, only a few subdominant modes are included in this sum as the contribution of almost all higher order modes are negligibly small. The dominant $(\ell,\, m') = (2,\, 2)$ mode is always included, and the leading subdominant modes $(\ell,\, m') = (2,\, 1)$ and $(\ell,\, m') = (3,\, 3)$ are usually included. Our implementation and the `LALSuite` implementation [117] of the `IMRPhenomXPHM` model use these modes and the $(\ell,\, m') = (3,\, 2)$ and $(\ell,\, m') = (4,\, 4)$ modes. Hence, the overall waveform observed in the inertial frame is reduced to a short list of basis modes, which have simpler frequency dependence individually.

The frequency-dependent coefficients $C^+_{\ell,m'}(f)$ and $C^\times_{\ell,m'}(f)$ incorporate an in-plane rotation by a frequency-independent angle ζ, which depends on the orientation of the binary, to correct for the difference between the computed spin-weighted spherical harmonics defined with respect to the total angular momentum vector, and the conventional parameterization of the waveform defined with respect to the reference orbital angular momentum vector.

$$C^+_{\ell,m'}(f) = \cos(2\zeta)\, \tilde{C}^+_{\ell,m'}(f) + \sin(2\zeta)\, \tilde{C}^\times_{\ell,m'}(f), \tag{2.2a}$$

$$C^\times_{\ell,m'}(f) = \cos(2\zeta)\, \tilde{C}^\times_{\ell,m'}(f) - \sin(2\zeta)\, \tilde{C}^+_{\ell,m'}(f). \tag{2.2b}$$

The tilded coefficients are specified in terms of the frequency-dependent Euler angles $\alpha(f)$, $\beta(f)$ and $\gamma(f)$, as well as θ_{JN}, the constant angle between the total angular momentum vector and the line of sight:

$$\tilde{C}^+_{\ell,m'}(f) = \frac{1}{2}\, e^{im'\gamma(f)} \sum_m \left(A^\ell_{m,-m'}(f) + (-1)^\ell \left[A^\ell_{m,m'}(f)\right]^* \right), \tag{2.3a}$$

$$\tilde{C}^\times_{\ell,m'}(f) = \frac{i}{2}\, e^{im'\gamma(f)} \sum_m \left(A^\ell_{m,-m'}(f) - (-1)^\ell \left[A^\ell_{m,m'}(f)\right]^* \right), \tag{2.3b}$$

where * stands for complex conjugation, and we introduce the following coefficient to describe the mixing between the L-frame modes and the J-frame modes under precession:

$$A^\ell_{m,m'}(f) = e^{-im\alpha(f)}\, d^\ell_{m,m'}(\beta(f))\, {}_{-2}Y_{\ell,m}(\theta_{JN}, 0). \tag{2.4}$$

Here, $d^\ell_{m,m'}(\beta(f))$ is the Wigner small d-matrix element evaluated at the Euler angle $\beta(f)$, and ${}_{-2}Y_{\ell,m}$ is the spin-weighted spherical harmonic.

Finally, like in Equation 1.23, the observed strain $h(f)$ at a given detector is a linear combination of the two wave polarizations $h_+(f)$ and $h_\times(f)$. The linear coefficients are given by the detector response coefficients, F_+ and $F_\times$, which are dependent on the sky position of the gravitational wave source and the orientation of the detector at the time of the gravitational wave event. The detector response coefficients depend on three extrinsic parameters: right ascension α, declination δ, and the polarization angle ψ. In the frequency domain, the arrival time t_0 of the event introduces a phase that scales linearly with the frequency.

$$h(f) = \left(F_+(\alpha, \delta, \psi)\, h_+(f) + F_\times(\alpha, \delta, \psi)\, h_\times(f)\right)\, e^{-2\pi i f t_0}. \tag{2.5}$$

The overall result is that the strain observed at a given detector can be cast into the following linear combination of the non-precessing modes,

$$h(f) = \sum_{\ell,m'} C_{\ell,m'}(f)\, h^L_{\ell,m'}(f)\, e^{-2\pi i f t_0}, \tag{2.6}$$

where

$$C_{\ell,m'}(f) = F_+(\alpha, \delta, \psi)\, C^+_{\ell,m'}(f) + F_\times(\alpha, \delta, \psi)\, C^\times_{\ell,m'}(f). \tag{2.7}$$

Two additional definitions are convenient for discussion in the following sections. First, we can absorb the arrival time dependence into the L-frame mode to define the time-dependent quantity

$$\hat{h}_{\ell,m'}(f) = h^L_{\ell,m'}(f)\, e^{-2\pi i f t_0}, \tag{2.8}$$

for which we simply have

$$h(f) = \sum_{\ell,m'} C_{\ell,m'}(f)\, \hat{h}_{\ell,m'}(f), \tag{2.9}$$

Second, we can incorporate the coefficient $C_{\ell,m'}$ and define the full mode component

$$h_{\ell,m'}(f) = C_{\ell,m'}(f)\, h^L_{\ell,m'}(f)\, e^{-2\pi i f t_0}. \tag{2.10}$$

The observed waveform then has the simple decomposition

$$h(f) = \sum_{\ell,m'} h_{\ell,m'}(f). \tag{2.11}$$

2.3 Mode-by-mode Relative Binning Schemes

As mentioned in Section 2.1, the original relative binning scheme assumes that the full waveform divided by a fiducial waveform is smooth in frequency space so that it can be well approximated by a piecewise linear interpolant. This scheme was developed for non-precessing waveform models that only account for the dominant (2, 2) mode. When applied to these waveform models, the assumption of the original relative binning scheme is only that the ratio of the (2, 2) mode evaluated for any given parameters over the (2, 2) mode evaluated at a fiducial set of parameters is a smooth function of the frequency. If the original relative binning method is applied to a precessing waveform comprised of multiple modes, this assumption is being extended to the sum of all modes, which is a stronger assumption. Instead, we improve our accuracy by not extending this assumption and only applying it to individual *non-precessing* modes.

At a fixed orbital frequency, the various L-frame modes produced by a binary source have different frequencies, and hence their superposition exhibit interference features. This leads to a jagged ratio for the overall waveform, $h(f)$, as a function of the frequency, as we exemplify in the top panel of Figure 2.1. The lower three panels in Figure 2.1, by contrast, show the smoother quantities $h_{\ell,m'}$, defined in Eq. (2.10), $\hat{h}_{\ell,m'}$, defined in Eq. (2.8), and $C_{\ell,m'}$, defined in Eq. (2.7), which are associated with individual L-frame modes. We will instead approximate these quantities or their ratios over fiducial counterparts by piecewise linear interpolants in our two schemes.

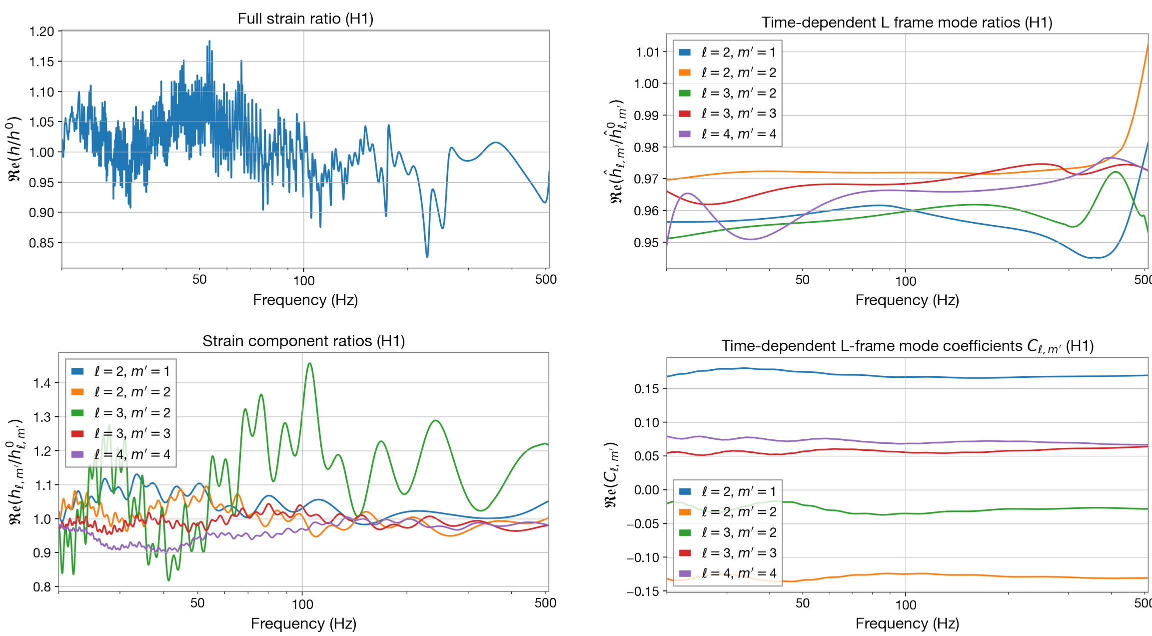

Figure 2.1: Functional smoothness as a function of frequency for the components or ratios that are approximated by piecewise linear functions in different relative binning methods. Shown are the real part of these complex-valued quantities, evaluated at the LIGO Hanford detector as an example. The fiducial waveform and one sample waveform are chosen from the posterior samples collected from our `MultiNest` run on the gravitational wave event GW190814. The harmonics (ℓ, m) shown are the 5 modes that are included by default in the waveform model `IMRPhenomXPHM`. The original relative binning method linearizes the full waveform ratios, as shown in the top left panel. Mode-by-mode relative binning linearizes the time-dependent L-frame mode ratios and their coefficients (right two panels) under Scheme 1, and the strain component ratios (bottom left panel) under Scheme 2.

2.3.1 Scheme 1

In the first scheme, we handle each time-dependent L-frame mode $\hat{h}_{\ell,m'}(f)$ as we handle the full waveform in the original relative binning method. To this end, we decompose the fiducial waveform as

$$h^0(f) = \sum_{\ell,m'} C^0_{\ell,m'}(f)\, \hat{h}^0_{\ell,m'}(f). \tag{2.12}$$

In this scheme, we suitably create frequency bins which we label by b. Within each frequency bin, the ratio of the time-dependent L-frame mode over some fiducial one is well approximated by a linear interpolant:

$$r_{\ell,m'}(f) = \frac{\hat{h}_{\ell,m'}(f)}{\hat{h}^0_{\ell,m'}(f)} \approx r^0_{\ell,m'}(h,b) + r^1_{\ell,m'}(h,b)\ (f - f_c(b))\,, \tag{2.13}$$

where $f_c(b)$ is the frequency at the bin center. The coefficients $r^0_{\ell,m'}(h,b)$ and $r^1_{\ell,m'}(h,b)$, defined for every frequency bin, are found by computing the waveform ratio at the bin edges. The speedup of relative binning hence comes from the fact that it suffices to evaluate at the bin edges for an excellent approximation of the likelihood. To obtain the full waveform $h(f)$, we also need the frequency dependent coefficients, which we also linearize within each frequency bin:

$$C_{\ell,m'}(f) \approx C^0_{\ell,m'}(h,b) + C^1_{\ell,m'}(h,b)\,(f - f_c(b))\,. \tag{2.14}$$

The constant coefficient in the piecewise linear interpolant of C ($C^0_{\ell,m'}(h,b)$) is not to be confused with the fiducial C ($C^0_{\ell,m'}(f)$). We disambiguate by showing that the former is a function of bin b and waveform h, and the latter is a function of frequency f. Likewise, the coefficients $C^0_{\ell,m'}(h,b)$ and $C^1_{\ell,m'}(h,b)$ can be computed from $C_{\ell,m'}(f)$ evaluated at the bin edges. In practice, we find that both quantities are smooth functions of the frequency, as shown in Figure 2.1. We then need to compute the likelihood in terms of these linearized ratios and coefficients. The log likelihood for the data series, $d(f)$, given a signal series $h(f)$, is given by:

$$\ln L = \mathfrak{Re}\, Z[d,h] - \frac{1}{2} Z[h,h], \tag{2.15}$$

where $Z[\cdots]$ is the notation for the standard complex-valued overlaps defined via a summation over only positive frequencies $f > 0$:

$$Z[d,h] = 4 \sum_f \frac{d(f)\, h^*(f)}{S_n(f)/T}, \tag{2.16a}$$

$$Z[h,h] = 4 \sum_f \frac{|h(f)|^2}{S_n(f)/T}, \tag{2.16b}$$

where $S_n(f)$ is one-sided power spectral density (PSD) of the detector noise, and T is the length of time series analyzed.

To approximate the above overlaps, we introduce a number of summary data for each frequency bin. The A coefficients are used in the overlap $Z[d,h]$ and are associated with a single L-frame mode because they are linear in the strain h. The B coefficients are used in the overlap $Z[h,h]$ and are associated with a pair of L-frame modes because they are quadratic in the strain h.

$$A^0_{\ell,m'}(b) = 4\sum_{f\in b}\frac{d(f)\,\hat{h}^{0*}_{\ell,m'}(f)}{S_n(f)/T} \tag{2.17a}$$

$$A^1_{\ell,m'}(b) = 4\sum_{f\in b}\frac{d(f)\,\hat{h}^{0*}_{\ell,m'}(f)}{S_n(f)/T}\,(f-f_c(b)) \tag{2.17b}$$

$$B^0_{\ell,m',\tilde{\ell},\tilde{m}'}(b) = 4\sum_{f\in b}\frac{\hat{h}^{0}_{\ell,m'}(f)\,\hat{h}^{0*}_{\tilde{\ell},\tilde{m}'}(f)}{S_n(f)/T} \tag{2.17c}$$

$$B^1_{\ell,m',\tilde{\ell},\tilde{m}'}(b) = 4\sum_{f\in b}\frac{\hat{h}^{0}_{\ell,m'}(f)\,\hat{h}^{0*}_{\tilde{\ell},\tilde{m}'}(f)}{S_n(f)/T}\,(f-f_c(b)) \tag{2.17d}$$

These summary data only depend on the data series $d(f)$ and the chosen fiducial waveform, and hence can be computed in advance of the large number of likelihood evaluations required in the sampling process. To obtain the log likelihood at each sampled set of waveform parameters, we approximate the overlaps up to linear order in $(f - f_c(b))$, using the following sums over frequency bins

$$\begin{aligned} Z[d,h] = \sum_b \sum_{\ell,m'} \big[& A^0_{\ell,m'}(b)\, r^{0*}_{\ell,m'}(h,b)\, C^{0*}_{\ell,m'}(h,b) \\ & + A^1_{\ell,m'}(b)\,\left(r^{1*}_{\ell,m'}(h,b)\, C^{0*}_{\ell,m'}(h,b) + r^{0*}_{\ell,m'}(h,b)\, C^{1*}_{\ell,m'}(h,b)\right)\big]\,, \end{aligned} \tag{2.18a}$$

$$\begin{aligned} Z[h,h] = \sum_b \sum_{\ell,m'} \sum_{\tilde{\ell},\tilde{m}'} \Big\{ & B^0_{\ell,m',\tilde{\ell},\tilde{m}'}(b)\, r^0_{\ell,m'}(h,b)\, r^{0*}_{\tilde{\ell},\tilde{m}'}(h,b)\, C^0_{\ell,m'}(h,b)\, C^{0*}_{\tilde{\ell},\tilde{m}'}(h,b) \\ & + B^1_{\ell,m',\tilde{\ell},\tilde{m}'}(b)\,\Big[C^0_{\ell,m'}(h,b)\, C^{0*}_{\tilde{\ell},\tilde{m}'}(h,b)\,\left(r^0_{\ell,m'}(h,b)\, r^{1*}_{\tilde{\ell},\tilde{m}'}(h,b) + r^{0*}_{\tilde{\ell},\tilde{m}'}(h,b)\, r^1_{\ell,m'}(h,b)\right) \\ & + r^0_{\ell,m'}(h,b)\, r^{0*}_{\tilde{\ell},\tilde{m}'}(h,b)\,\left(C^0_{\ell,m'}(h,b)\, C^{1*}_{\tilde{\ell},\tilde{m}'}(h,b) + C^{0*}_{\tilde{\ell},\tilde{m}'}(h,b)\, C^1_{\ell,m'}(h,b)\right)\Big]\Big\}\,. \end{aligned} \tag{2.18b}$$

To summarize, the summary data Eq. (2.17) can be pre-computed from the data and the chosen fiducial waveform; then to approximate the log likelihood using Eq. (2.18) and Eq. (2.15), $r^0_{\ell,m'}(h,b)$, $r^1_{\ell,m'}(h,b)$, $C^0_{\ell,m'}(h,b)$, and $C^1_{\ell,m'}(h,b)$ only need to be evaluated at the bin edges.

2.3.2 Scheme 2

Scheme 1 involves the multiplication of two quantities, both of which are separately approximated as piecewise linear functions. One might wonder if this strategy accumulates excessive errors. Hence, we consider an alternative scheme, which we refer to as Scheme 2. In this scheme, we linearize the ratio of the entire mode component over its fiducial counterpart. To do so, we decompose the fiducial waveform $h^0(f)$ as in Eq. (2.11):

$$h^0(f) = \sum_{\ell,m'} h^0_{\ell,m'}(f) \tag{2.19}$$

Within the frequency bin b, we make the approximation

$$r_{\ell,m'}(f) = \frac{h_{\ell,m'}(f)}{h^0_{\ell,m'}(f)} \approx r^0_{\ell,m'}(h,b) + r^1_{\ell,m'}(h,b)\,(f - f_c(b))\,. \tag{2.20}$$

This quantity is also much smoother than the ratio for the observed waveform, which is linearized in the original relative binning method, as one can see in Figure 2.1. In this scheme, our summary data are very similar, but they use the full fiducial mode components:

$$A^0_{\ell,m'}(b) = 4\sum_{f\in b} \frac{d(f)\,h^{0*}_{\ell,m'}(f)}{S_n(f)/T} \tag{2.21a}$$

$$A^1_{\ell,m'}(b) = 4\sum_{f\in b} \frac{d(f)\,h^{0*}_{\ell,m'}(f)}{S_n(f)/T}\,(f - f_c(b)) \tag{2.21b}$$

$$B^0_{\ell,m',\tilde{\ell},\tilde{m}'}(b) = 4\sum_{f\in b} \frac{h^0_{\ell,m'}(f)\,h^{0*}_{\tilde{\ell},\tilde{m}'}(f)}{S_n(f)/T} \tag{2.21c}$$

$$B^1_{\ell,m',\tilde{\ell},\tilde{m}'}(b) = 4\sum_{f\in b} \frac{h^0_{\ell,m'}(f)\,h^{0*}_{\tilde{\ell},\tilde{m}'}(f)}{S_n(f)/T}\,(f - f_c(b)) \tag{2.21d}$$

Now that there is only one linearized quantity, the overlaps have shorter expressions:

$$Z[d,h] = \sum_b \sum_{\ell,m'} \left[A^0_{\ell,m'}(b)\,r^{0*}_{\ell,m'}(h,b) + A^1_{\ell,m'}(b)\,r^{1*}_{\ell,m'}(h,b)\right], \tag{2.22a}$$

$$\begin{aligned} Z[h,h] = \sum_b \sum_{\ell,m'} \sum_{\tilde{\ell},\tilde{m}'} \Big[& B^0_{\ell,m',\tilde{\ell},\tilde{m}'}(b)\,r^0_{\ell,m'}(h,b)\,r^{0*}_{\tilde{\ell},\tilde{m}'}(h,b) \\ & + B^1_{\ell,m',\tilde{ell},\tilde{m}'}(b)\left(r^0_{\ell,m'}(h,b)\,r^{1*}_{\tilde{\ell},\tilde{m}'}(h,b) + r^{0*}_{\tilde{\ell},\tilde{m}'}(h,b)\,r^1_{\ell,m'}(h,b)\right)\Big]\,. \end{aligned} \tag{2.22b}$$

Again, the pre-computed summary data Eq. (2.21) can be substituted into Eq. (2.22) to compute the overlaps Eq. (2.16) up to linear order in $(f - f_c(b))$. The coefficients $r^0_{\ell,m'}(h,b)$

and $r^1_{\ell,m'}(h,b)$ only require evaluating the model waveform at the edges of the frequency bins. Although Scheme 2 have simpler expressions than Scheme 1, it is not meaningfully faster in terms of the computation runtime, as all evaluations needed for computing $C_{\ell,m'}(f)$ and $\hat{h}_{\ell,m'}(f)$ are also needed for computing $h_{\ell,m'}(f)$.

2.3.3 Bin Selection

Previously, a prescription to determine the frequency bins for the original relative binning method is presented in Ref. [205]. Motivated by the post-Newtonian expansion, this prescription selects frequency bins to bound the differential phase changes assuming a phenomenological ansatz in the form of a sum over power-law phases. Although the prescription has the advantage that it is independent of the specific compact binary coalescence signals under analysis, it may not be the optimized bin selection on the event-by-event basis. In particular, for high binary masses, the merger and ringdown signals may dominate the sensitive frequency band of the detector, and the corresponding gravitational wave signal may be poorly described by the post-Newtonian expansion.

In this work, we present a new bin selection algorithm that is adaptive to any given gravitational wave signal under investigation. Since the linearized quantities associated with individual modes have smoother frequency dependence than the observed waveform, we can afford fewer frequency bins to achieve a comparable accuracy for the log likelihood. Since the bottleneck in the computational time cost is still the large number of likelihood evaluations, we can afford to adjust the frequency bins event by event via an algorithm that is more time-consuming than the one that is adopted in Ref. [205]. We choose a representative waveform (different from the fiducial waveform) for an estimate of the binning errors. We can then test out various binning choices on this representative waveform. Methods for choosing this waveform are discussed in Section 2.5.

Our algorithm determines the frequency bins by starting with the entire frequency range as a single bin and iteratively bisecting the frequency bins. In this iterative process, we compute, for each existing frequency bin, the error contribution to the log likelihood due to mode-by-mode relative binning. We keep bisecting the bins until the overall absolute error in the log likelihood is smaller than a empirically set threshold. We iterate the whole procedure and update the target number of bins to the number of bins achieved in the previous run, until the resulting number of bins and the target number of bins converge. This algorithm is detailed in Algorithm 1.

The algorithm consistently converges to a fixed number of bins independent of the initial target number of bins (targetN), so we set this number arbitrarily to 200. By varying the total allowed error η on the test parameters, we trade computational cost (number of bins) for accuracy. We tested similar algorithms that unevenly divide the bins, but found that such methods are slower and did not improve accuracy.

Algorithm 1 Bin Selection

```
function GETBINS(η, targetN=200, testParams)
    targetBinError = η/targetN
    candidateBins = BISECTBINSEARCH(targetBinError, testParams, fullFrequencyGrid)
    nBins = NUMBEROFBINS(candidateBins)
    if nBins = targetN then
        return candidateBins
    else
        return GETBINS(η, targetN=nBins, testParams)
    end if
end function

function BISECTBINSEARCH(targetBinError, testParams, candidateBin)
    if LOGLIKELIHOODERROR(testParams, candidateBin) ≤ targetBinError then
        return candidateBin
    else if candidateBin is minimum size then
        return candidateBin
    else
        return BISECTBINSEARCH(targetBinError, testParams, leftHalf) + BISECTBINSEARCH(targetBinError, testParams, rightHalf)
    end if
end function
```

2.4 Testing Methods and Results

We tested the accuracy and efficiency of both mode-by-mode relative binning schemes on several real and synthetic compact binary coalescence events. We computed likelihoods of the `IMRPhenomXPHM` model using `LALSuite` [117] and gathered posterior samples using the `MultiNest` sampler [76].

To test our method, we consider gravitational wave signals with either strong spin-orbit precession or large contributions from the subdominant modes, or a combination of both, as their parameter estimation can be greatly improved with `IMRPhenomXPHM` or other precessing models with higher modes that exploit the twisting-up procedure. Precession occurs most dramatically in binaries that have large spin vectors misaligned with the binary orbital angular momentum vector (i.e. large in-plane spin components) [20]. Odd parity subdominant modes such as (3, 3) are important when there is a large asymmetry between the two components, e.g. when the mass ratio $q = m_2/m_1 < 1$ is small. Also, subdominant modes are larger in the late stage of the merger. For low mass mergers, the most sensitive LIGO/Virgo frequency band corresponds to the early inspiral of the merger. On the contrary, for heavy mass mergers, the most sensitive frequency band corresponds to the merger stage when subdominant modes are stronger. For these reasons, we study events with large in-plane spin components, or a small mass ratio q, or a large total mass.

We consider one real LIGO/Virgo event, GW190814, and four injected events. GW190814 is chosen because the original analysis shows strong Bayesian evidence favoring a model that includes the (3, 3) mode over one that has only the dominant (2, 2) mode [11]. The four injections are chosen as the following. Two are chosen to resemble the inferred source properties of two interesting LIGO/Virgo detections for which new source solutions have been recently reported from independent reanalyses using the `IMRPhenomXPHM` model: GW151226 [6, 58] and GW190521 [10, 136]. Both of these newly found solutions indicate a large spin misaligned with the orbital angular momentum on the primary mass and a low mass ratio $q < 1$. The GW151226 reanalysis showed that the new low-q solution were absent from the posterior distribution of the source parameters when either the higher modes or the precession effects were neglected [58]. The original analysis of GW190521 used the `IMRPhenomPv3HM` model [104], which had higher modes and precession, but not the improved calibration of the subdominant modes, and particularly not in the low-q regime [10, 136]. The other two injections are artificially made to have a high total mass and large in-plane spins: one with a high mass ratio $q < 1$ and another with a low mass ratio. The parameters used for the injections are listed in Table 2.1.

To start with, we need posterior source parameters for which we can evaluate the log likelihood both approximately using our new mode-by-mode binning method and exactly. The samples are collected using `MultiNest` with `nlive` = 2000. For these runs, the log likelihoods are evaluated using the original relative binning method of Ref. [205]. We use the parameter choice $\epsilon = 0.03$ for the maximum allowed differential phase (see Eq. 10 of Ref. [205] for the definition of ϵ), which is sufficient for obtaining accurate posterior samples. For the injected events, the injected parameters are used to set the fiducial waveform. For the real GW190814 event, fiducial parameters are found using `scipy`'s `differential_evolution` [182], a global optimization routine to (approximately) find the maximum likelihood fit to the data.

We obtain the strain data containing GW190814, as well as those used as the noisy background for our injections, from the public database GWOSC [13]. For each event, we collect a 16-second time series centered on the GPS time listed in Table 2.1 with a sampling rate of 1024 Hz. The injections are added at the 8 second mark into the noisy 16-second time series. PSDs are measured using Welch's method from a 128-second time series centered at the same GPS time with overlapping 16 s segments. We only include frequencies from 20 Hz to 512 Hz in the likelihood evaluation, as there is negligible SNR contribution outside this frequency range.

We make a comparison between the original relative binning method using the original bin selection algorithm (with the parameter $\epsilon = 0.03$ as defined in Ref. [205]), and the mode-by-mode relative binning method using our new bin selection (for a range of η values), evaluating for 2000 parameter combinations randomly drawn from the posterior distribution

Table 2.1: The parameters injected for the 4 injections used in this work, and the fiducial parameters for GW190814 found by using the global optimization algorithm `differential_evolution` provided in `scipy`. We generated waveforms using the `IMRPhenomXPHM` model with these parameters and injected them at the 8 s mark of a 16 s stream centered at the GPS time collected at a sampling rate of 1024 Hz. The parameter κ is defined in Appendix C of Ref. [150]

	High q	Low q	GW151226-like	GW190521-like	GW190814 (fid.)
Primary mass m_1 $[M_\odot]$	30.0	100.0	29.3	168.0	24.4
Secondary mass m_2 $[M_\odot]$	20.0	10.0	4.3	16.0	2.7
$\chi_{1,x}$	0.700	0.700	0.600	0.641	0.024
$\chi_{1,y}$	0.000	0.000	-0.200	0.000	0.039
$\chi_{1,z}$	0.000	0.000	0.500	-0.559	0.002
$\chi_{2,x}$	0.000	0.000	0.000	0.000	-0.305
$\chi_{2,y}$	0.700	0.700	0.000	0.000	-0.574
$\chi_{2,z}$	0.000	0.000	0.000	0.000	-0.067
Luminosity distance D_L [Mpc]	496.91	496.91	457.00	400.00	283.28
Line of sight $\theta_{\rm JN}$ [rad]	1.200	1.200	0.403	0.500	2.408
κ	0.200	0.200	0.000	0.000	2.730
Right ascension α [rad]	3.000	3.000	3.831	3.340	0.412
Declination δ [rad]	0.100	0.100	-0.819	0.600	-0.574
Polarization angle ψ [rad]	0.500	0.500	2.698	0.000	2.962

	High q	Low q	GW151226-like	GW190521-like	GW190814 (fiducial)
GPS time	1242443867.4	1242443867.4	1135137260.6	1242443867.4	1249852257.0

derived for each event or injection. The bin selection algorithm uses a random posterior sample selected as the test waveform. We study the absolute errors in the log likelihood computed for these samples, which are shown in Figure 2.2.

Figure 2.2 shows the cumulative distribution function (CDF) for the absolute error in the log likelihood for the 2000 posterior samples collected for each event. We compare the original relative binning method with mode-by-mode relative binning, testing both our approximation schemes and varying η. The varying numbers of bins result from using different η values. The number of frequency bins is one less than the number of required frequency-domain waveform evaluations, which dominate the runtime, so the bin number is a good proxy for the runtime. In all examples we show, the original relative binning method uses the same number of frequency bins because the bin selection prescription only depends on the frequency range and the maximum differential phase ϵ, which do not change from event to event.

In Section 2.4.1, we investigate the tolerable size of the absolute error in the log likelihood for obtaining accurate posterior distributions. Conservatively, we conclude that the log likelihood error should be no greater than ~ 0.1 as random errors with a standard deviation of 0.1 appear to have unnoticeable effect in the posterior.

For the high q injection, and using only 148 bins with Scheme 1, the errors with mode-by-mode relative binning (MRB) are smaller than those with the original relative binning method using 1027 bins at all percentiles. Using about 300 bins, both Scheme 1 and Scheme 2 are able to achieve this. Notably, these three cases have the log likelihood error no greater than 0.1 for all samples.

Similarly, for the low q injection, the MRB error derived from about 125 bins strictly outperforms that of the original relative binning. The error distribution has a larger standard deviation than in the high q case, but this is due to most of low error samples having even smaller errors.

For all methods, the samples for the GW151226-like injection have larger errors, but using 117 bins with Scheme 1 the error is less than 0.1 for 60% of the samples, and using more bins the spread of the worse errors is significantly reduced, and the error is nearly always less than 0.2 for roughly twice the number of bins.

The GW190521-like injection is the only example studied here where Scheme 2 achieves lower errors than Scheme 1 does using comparable number of bins. Nevertheless, Scheme 1 achieves lower errors than the original relative binning scheme with 430 bins. For the GW190814 event, 90% of the errors are less than 0.1, when using 300–400 bins with both Scheme 1 and Scheme 2. The errors are roughly a factor of two to four larger using only 73 bins under Scheme 1. In the 317 bin case, Scheme 1 reduces the error by nearly an order of magnitude at one third of the computational cost when compared with original relative binning.

Overall, both MRB schemes achieve lower errors with fewer bins at all percentiles above 50% when compared with the original relative binning method. In all cases, MRB achieves a median absolute error of 0.1 using substantially reduced number of bins.

2.4.1 Target Log Likelihood Error

The absolute error in the log likelihood from mode-by-mode relative binning should be small enough not to bias the obtained posterior distribution for the source parameters. In this section, we study the impacts of log likelihood errors on the posterior distributions, using the high-q injection as an example.

Our posterior samples have been obtained using the original relative binning method with finite likelihood errors. To obtain the exact (full FFT) posterior distribution, we use the method of importance sampling (IS). Let sample i have the exact posterior

$$P_{\mathrm{exact}}[i] = \frac{L_{\mathrm{exact}}[i]\, p_i[i]}{Z}, \tag{2.23}$$

where $L_{\mathrm{exact}}[i]$ is the exact likelihood, $p[i]$ is the prior, and Z is the evidence. Using the original relative binning method, we have

$$P_{\mathrm{ORB}}[i] = \frac{L_{\mathrm{ORB}}[i]\, p_i[i]}{Z}, \tag{2.24}$$

where $L_{\mathrm{ORB}}[i]$ is the relative binning likelihood. Importance sampling requires that samples are weighted by the ratio of the desired distribution over the sampled one, so to get samples of the exact posterior, each sample has the weight

$$w[i] = \frac{P_{\mathrm{exact}}[i]}{P_{\mathrm{ORB}}[i]} = \frac{L_{\mathrm{exact}}[i]}{L_{\mathrm{ORB}}[i]} = e^{\ln L_{\mathrm{exact}}[i] - \ln L_{\mathrm{ORB}}[i]}. \tag{2.25}$$

We can also use importance sampling to simulate specific errors in the log likelihood. The distribution of the log likelihood errors due to either relative binning method is approximately Gaussian, so we can model these errors as Gaussian random variables. Let these errors be called $\delta[i]$; one is drawn for each sample from a Gaussian distribution. Then our simulated log likelihood with this error is

$$\ln L_{\mathrm{sim}}[i] = \ln L_{\mathrm{exact}}[i] + \delta[i]. \tag{2.26}$$

So following Eq. (2.25), the weight for the sample from this simulated distribution is

$$w_{\mathrm{sim}}[i] = \frac{L_{\mathrm{sim}}[i]}{L_{\mathrm{ORB}}[i]} = e^{\ln L_{\mathrm{exact}}[i] - \ln L_{\mathrm{ORB}}[i] + \delta[i]}. \tag{2.27}$$

The above weights can be used to generate altered posteriors for comparison with an exact posterior. Such comparisons along with a histogram of the log likelihoods are shown for our high q posterior in Figure 2.3. When the errors have a standard deviation of 0.1, they make virtually no visible impact in the posterior whatsoever. The simulated posteriors with log likelihood errors of standard deviation 0.5 and 1.0 have small inconsistencies, but their contours are generally unaltered in shape. However, once the standard deviation of the simulated error reaches 2.0, the contours are substantially distorted.

Additionally, in the left panel of Figure 2.4, the actual posterior gathered from the original relative binning method and the importance weighted exact (full FFT) posterior do not differ at all. As can be seen in the blue histogram in the right panel of Figure 2.4, the spread of the original relative binning errors log likelihood is a about 0.1.

In this example, we see that original relative binning error with a spread of about 0.1 is sufficiently small to not impact the posterior. Additionally the effect of the Gaussian error was negligible on the posterior at the same scale, and minimal up to an order of magnitude higher. Because this is only one event, we will be conservative, and use 0.1 as our target threshold, which is well justified by all of these results.

2.5 Discussion

In all cases except the GW190521-like injection, Scheme 1 outperforms Scheme 2. We believe this is because the quantities linearized in Scheme 1 are usually smoother functions of the frequency than those linearized in Scheme 2, which reduces the required number of bins for a given accuracy goal. This can be seen in Figure 2.1. In fact, the ratio linearized in Scheme 2 is related to the one linearized in Scheme 1 through

$$\begin{aligned}[r_{\ell,m'}(f)]_{\text{Scheme 2}} &= \frac{h_{\ell,m'}(f)}{h^0_{\ell,m'}(f)} = \frac{C_{\ell,m'}(f)\hat{h}_{\ell,m'}(f)}{C^0_{\ell,m'}(f)\hat{h}^0_{\ell,m'}(f)} \\ &= \frac{C_{\ell,m'}(f)}{C^0_{\ell,m'}(f)} \left[r_{\ell,m'}(f)\right]_{\text{Scheme 1}} . \end{aligned} \tag{2.28}$$

The ratio linearized in Scheme 1 is similar to the ratio linearized in the original relative binning method applied to non-precessing waveform models. The L-frame mode components are equivalent to the J-frame components for a non-precessing waveform, and it has already been demonstrated that the ratio of non-precessing waveforms are smooth in the frequency space. However, the ratio $C_{\ell,m'}(f)/C^0_{\ell,m'}(f)$ can exhibit large oscillations or even sharp peaks when the denominator $C^0_{\ell,m'}(f)$ becomes small. This situation may arise because the coefficient $C_{\ell,m'}(f)$ is a linear combination of terms that may nearly cancel (see construction of $C_{\ell,m'}(f)$ in Section 2.2).

However, it can also happen that Scheme 2 outperforms Scheme 1. When the aforementioned issue regarding $C^0_{\ell,m'}(f)$ does not arise, Scheme 2 may have an advantage because there are fewer quantities to be linearized so as to avoid compounding error. This appears to be the case in the GW190521-like injected event. The linearized quantities evaluated for one posterior sample of this event are compared in Figure 2.5. In this example, Scheme 1 is not advantageous over Scheme 2 in terms of frequency-space smoothness of the linearized quantities.

Overall, we conclude that Scheme 1 is more robust because it accounts for the difficult case of small $C^0_{\ell,m'}(f)$, and more often yields better relative binning results, especially in the case of GW190814. In practice, the preferred scheme can be empirically determined alongside the process of choosing suitable fiducial and test waveforms.

To use mode-by-mode relative binning in practice, one has to set a fiducial waveform for computing the summary data, and a test waveform for determining the frequency bins. If the experimental collaboration has already provided full parameter inference results for the event under analysis, the reported parameters can be used as the fiducial parameters. If the signal under analysis is uncovered by a search pipeline, crude source masses and spins are typically reported, and can be used as the initial choice for the fiducial parameters. If not all parameters are reported, or are only reported for simplified waveform models, then the fiducial parameters can be obtained via global maximization of the exact likelihood. For well measured parameters, global optimization should be performed within the small vicinity of the reported values. For poorly measured parameters, optimization can performed over the entire physically allowed region.

If global optimization using the exact likelihood is computationally too slow, it is feasible to couple the relative binning approximation to the optimization. If the likelihood errors from using the initial choice of ficudial parameters are still too large, the fiducial parameters can be iteratively updated, just like what has been practiced using the original relative binning method [205, 67]. As a matter of fact, there is great flexibility in setting the fiducial parameters, as many extrinsic parameters enter the individual modes only through frequency *independent* factors which do not degrade the accuracy of mode-by-mode relative binning.

Our results are minimally affected when changing which sample is used as the test waveform for the selection of frequency bins. This suggests that any set of test parameters in the support of the posterior distribution would be satisfactory. In practice, we recommend obtaining the test parameters by running a few iterations of a sampler starting from the fiducial parameters. The test parameters can be obtained by a few Metropolis-Hastings iterations, or a few steps of a more sophisticated sampler running on the exact log likelihood.

2.6 Chapter 2 Conclusion

Faster likelihood evaluations are an important aspect of speeding up gravitational wave parameter inference. We have developed the mode-by-mode relative binning method as an efficient approximation of the likelihood function, and have demonstrated its enhanced accuracy and theoretical speedup compared with the original relative binning method that does not take advantage of the multi-modal structure of the waveform.

The initial implementation of this method can be found in our git repository at `https://github.com/nathaniel-leslie/modebymode-relative-binning`, but a more optimized version has been implemented in `bilby` [21] as `bilby.gw.likelihood.RelativeBinningGravitationalWaveTransientNextGenerationModebyMode`. By counting waveform evaluations, which dominate runtime, this mode-by-mode relative binning method should run faster than comparable reduced-order quadratures. An ROQ has been built for `IMRPhenomXPHM` using a code called PyROQ [156]. To evaluate the likelihood with ROQ, one must evaluate the linear and quadratic overlaps, which correspond to Eq. (2.16a) and Eq. (2.16b) respectively. Each overlap requires an interpolant to be evaluated, which requires the number of waveform evaluations that is equal to the number of basis functions for each interpolant. In Table III of [156], it is shown that the total number of basis functions in their ROQ for `IMRPhenomXPHM` with a signal up to 1024 Hz ranged from 600 to 1100, depending on the parameter ranges. As shown in Figure 2.2, mode-by-mode relative binning can achieve the conservative target of absolute errors in the log likelihood error being around 0.1 on all test events with only around 100–200 frequency bins.

Another benefit of mode-by-mode relative binning is the ability to vary η to flexibly trade speed for accuracy. This only requires recomputing bins by rerunning Algorithm 1 with a new value of η, which takes a few seconds. If one achieves sufficient accuracy for a specific problem and can afford to sacrifice some, η can be increased, which reduces bin count and runtime. Similarly, if one requires higher accuracy and can afford some additional runtime, η can be decreased, which increases bin count and runtime but also improves accuracy.

Our conclusions about runtime are based on the reduction in the number of waveform evaluations, and nearly equivalently, the number of frequency bins. As we have mentioned previously, this is justified by the observation that waveform evaluation calls dominate the computational time of the likelihood evaluation. In the code used in this work, and for the `IMRPhenomXPHM` waveform model as an example, we have computed the L-frame modes $h^L_{\ell,m'}(f)$ and the Euler angles $\alpha(f)$, $\beta(f)$, and $\gamma(f)$ by calling the available `LALSuite` routines [117]. These routines take approximately 3/4 of the time of a full likelihood evaluation using the full `LALSuite` routines for obtaining h_+ and $h_\times$. The remaining time is primarily spent on computing the twisting factors $C^+_{\ell,m'}$ and $C^\times_{\ell,m'}$, which involves a significant amount of evaluations of trigonometric functions and scales linearly with the bin number. Our current Python implementation of mode-by-mode relative binning is still inefficient due to overhead; it takes a few milliseconds to compute these twisting factors even for a few frequencies. The existing `LALSuite` routines for obtaining $h_+(f)$ and $h_\times(f)$ are sufficient for implementing the original relative binning method, which do not require computations of the twisting factors in Python. For this method, with 1027 bins, each likelihood evaluation takes roughly $\sim$ 4-5 ms on a 2018 MacBook Pro with a 2.6 GHz Intel i7 processor. The time that it takes to evaluate the L-frame modes and Euler angles at the original bins is also about 3/4 of this time. For the 133 bin evaluation shown in the GW190814 pane of Figure 2.2, the L-frame modes and Euler angles took approximately 0.7 ms. Assuming optimized implementation of the twisting factors, the same extrapolation suggests that sub-millisecond likelihood evaluations are achievable.

The `bilby` implementation of mode-by-mode relative binning has been used in forecasts of parameter estimation capabilities of next generation detectors in [25]. With this implementation in such a widely used gravitational wave parameter estimation package, anyone studying gravitational wave data from systems with higher modes and precession effects can use this method for fast and accurate parameter estimation.

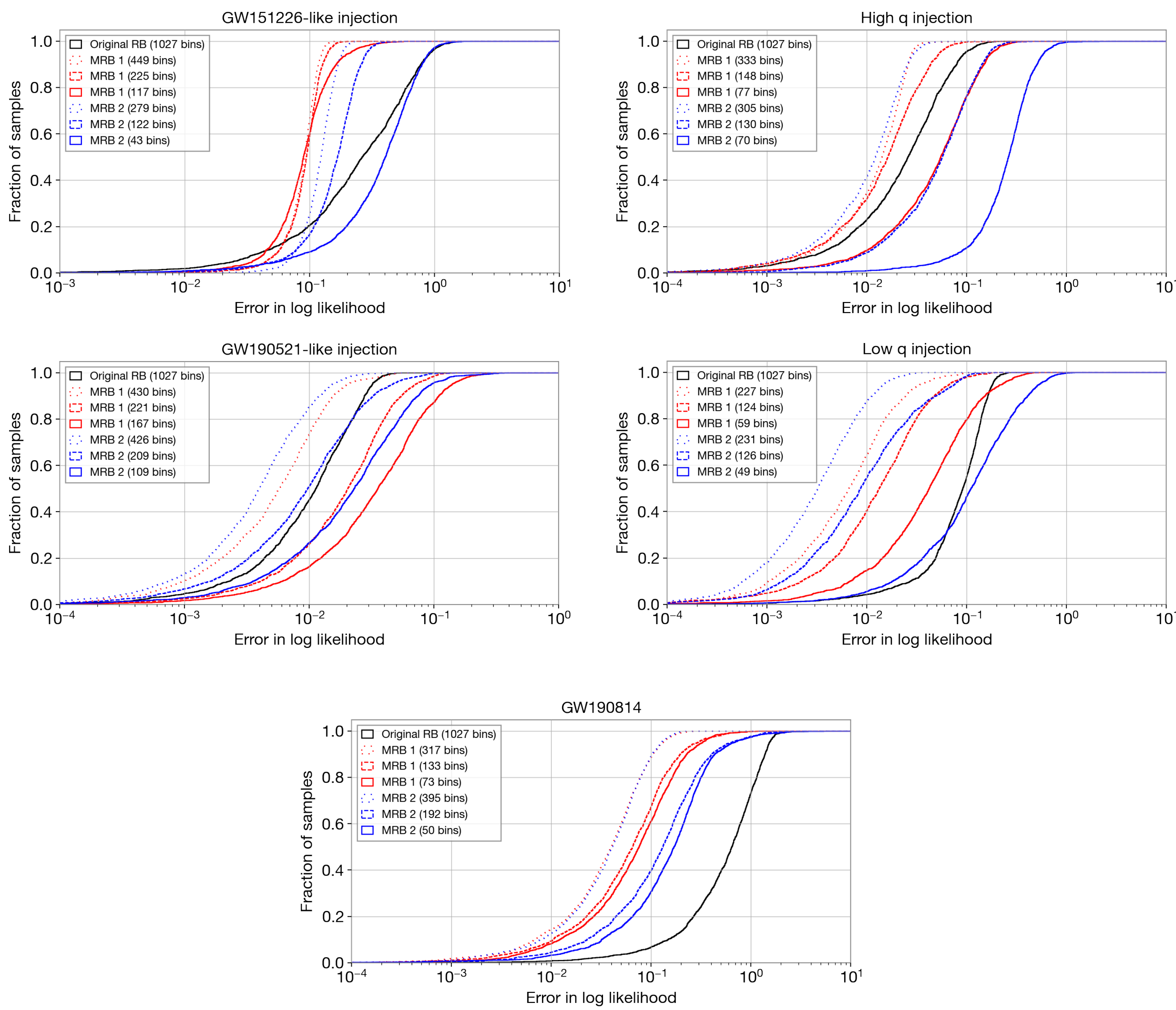

Figure 2.2: CDFs for the *absolute* error in the log likelihood from the original relative binning and the mode-by-mode relative binning (MRB), evaluated for 2000 posterior samples collected for four synthetic signals and one real signal we analyze. Different lines for the same scheme correspond to different values of η, which result in different numbers of bins. Both MRB schemes are able to outperform the original relative binning for the worst samples with fewer bins.

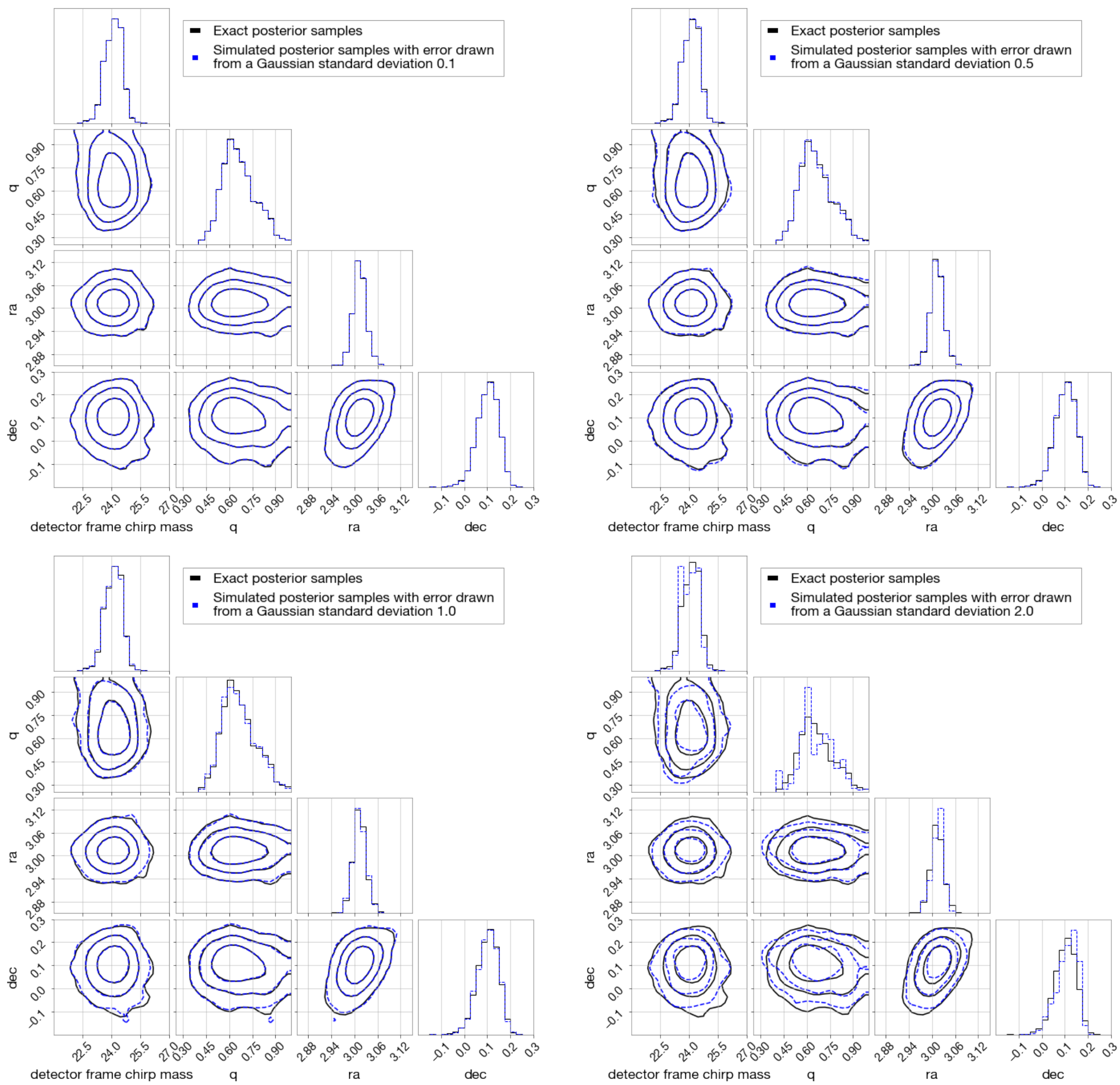

Figure 2.3: Each panel shows the effect of zero-mean Gaussian random errors of various standard deviations added to the log likelihood on posterior distributions for the high-q injection. The contours enclose 68%, 95%, and 99.7% of the two-dimensional joint posterior samples.

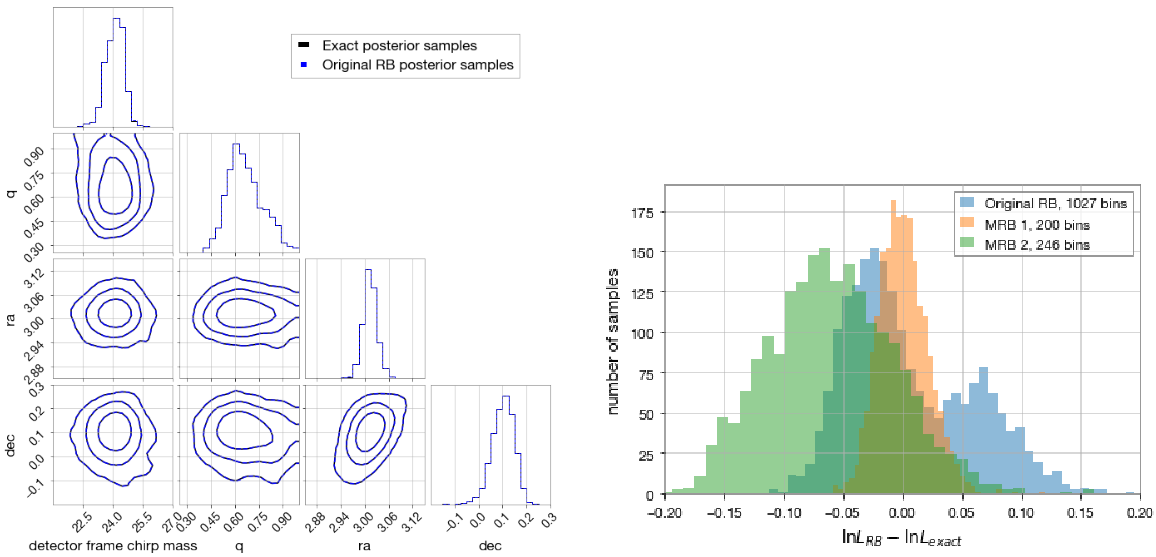

Figure 2.4: These panels visualize the errors from the various relative binning methods on the high-q injection. The left panel compares the posterior samples obtained from the original relative binning to the importance weighted posterior samples using the exact log likelihood. The right panel shows the log likelihood errors for original relative binning, and our two relative binning schemes for the choice of $\eta = 0.1$. The errors are not entirely dissimilar from Gaussian, and the original relative binning error shown makes no noticeable effect on the posterior distribution.

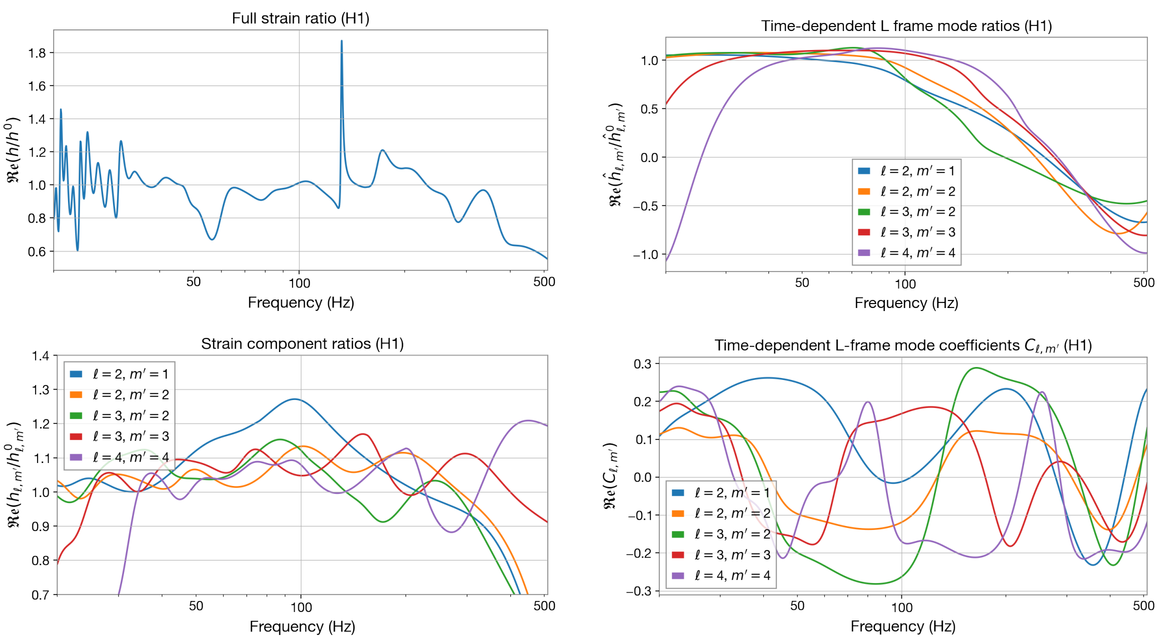

Figure 2.5: Same as Figure 2.1 but for the GW190521-like injection. This is an example where Scheme 1 is not advantageous over Scheme 2. Again, mode-by-mode relative binning linearizes the time-dependent L-frame mode ratios and their coefficients (bottom two panels) under Scheme 1, and linearizes the strain component ratios (second panel) under Scheme 2.

Chapter 3

A Gravitational Waveform Model for an Accelerating Source

3.1 Introduction

Gravitational waves (GWs) from inspiraling and merging compact binaries have been detected in large quantities by the LIGO-Virgo-KAGRA (LVK) collaboration [116]. This experimental success is enabled not only by improvement of detector sensitivity [64, 126, 169], but also by advances in developing highly accurate analytic [69, 33] and numerical [53, 180] gravitational waveform models for the two-body problem in general relativity (GR).

The common approach for GW detection and parameter inference [59, 99, 169] requires readily available waveform models that follow the binary's motion to high accuracy over many orbits [139, 140, 165]. Progress in the GR two-body problem has enabled rapid generation of accurate waveform models for bound two-body orbits, based on which robust, scalable analyses of the strain time series at interferometers have been implemented [139, 31, 120]. On the other hand, discovery of novel GW sources can be hindered by a lack of accurate waveform models.

One type of system that is still absent from the current GW source catalog are hierarchical triple systems, where two compact objects in a bound orbit themselves orbit a third distant mass [72, 190, 135, 158]. Accurately calculating secularly evolving three-body orbits in GR and rapidly generating the corresponding waveform templates for the entire three-body system is a topic of ongoing numerical investigations [35, 83]. The inspiralling two-body GW signal, however, can be treated perturbatively as its motion secularly evolves due to the third body.

The focus of this chapter will be gravitational waves from a simple case of hierarchical triple systems. Our investigation is motivated by the detection of GW190814 [11], an inspiral-merger event of a $23\,M_{\odot}$ black hole (BH) and a $2.5\,M_{\odot}$ compact object. The nature of the less massive compact object is puzzling: it is either the lightest BH known to exist or an exceptionally massive neutron star (NS). To offer an explanation for how GW190814 might have formed, some recent studies (e.g. [91, 122]) have investigated if it might be the end state of a hierarchical triple system, in which two NSs merged to form the $2.5\,M_\odot$ object. This setting may also be relevant for events with similar mass ratios with a component in the mass gap (e.g. GW200210 [12]). In Ref. [122], it is argued that roughly 10% of binary NS mergers might occur near a massive third body if such a triple mechanism is the origin of mergers that involve a mass-gap object. If the signature of a tertiary mass around merging NS binaries can be detected in the GW signal, it would be a discovery of three-body interactions as a dynamical origin of these LVK GW sources.

There is also motivation to study binary BHs (BBHs) whose center-of-mass (CoM) accelerates during inspiral events. Studies of BBH formation in active galactic nuclei and globular clusters often predict nontrivial CoM motions [181, 129, 27, 19, 202, 189]. Studies of single-binary scattering have demonstrated that GW sources can form during chaotic three-body interactions [168, 167, 88]. The hypothesis that events like GW190814 arise from hierarchical triples hinges on double merger events, which have also been observed in single-binary BH scattering simulations [166].

In this chapter, we present an analytic gravitational waveform model for two inspiraling compact objects whose CoM has a small acceleration due to the gravitational pull of a tertiary body. CoM acceleration imprints a non-trivial distortion to the wave phase, whereas a constant CoM velocity simply imparts a Doppler shift and is fully degenerate with the orbital frequency, source distance, and source masses [66]. We specialize to the case in which the third body is sufficiently distant compared to the compactness of the binary so that the inspiraling binary as a whole simply follows two-body geodesic motion. In the free-falling frame of the binary, the internal inspiral motion of the binary is assumed to be well described by the usual two-body dynamics in GR. In this situation, tertiary tidal perturbations on the binary orbital phase is assumed to be negligible over LVK signal timescales, and hence the CoM acceleration manifests as a time-dependent delay for the detected GWs.

There are previous studies that address CoM acceleration for GW sources, but our full analytic waveform model has yet to appear in the literature. Accelerating sources have been considered in sources for the Laser Interferometer Space Antenna (LISA); for example, concerning extreme-mass-ratio-inspirals near a supermassive BH [204], comparable mass binaries embedded in an environment [97, 157, 200], double white-dwarf binaries near a tertiary star [201], a compact binary wobbling due to a circumbinary planet [184], and apparent acceleration of a source due to a time-dependent redshift [185]. The Newtonian model presented in [184] has been used in a recent parameter estimation study for GW190814 [92], though we demonstrate that higher order post-Newtonian (PN) corrections are needed for a complete analysis for ground-based and next-generation detectors. For ground-based compact object binaries, Ref. [130] gives a back-of-envelope estimation for the detectability of a tertiary's imprint from the GW signal within a hierarchical triple. Another recent study has outlined a numerical framework for analyzing time-dependent Doppler effects for full inspiral-merger-ringdown models [54]. We instead consider detection at ground-based GW detectors for inspiral events, which requires higher-order post-Newtonian (PN) corrections to the orbital phase. Our model reduces to the Newtonian result [185] in the appropriate limit.

While we were independently working on this model, another study carried out an in-depth investigation on the detectability of CoM acceleration at current and upcoming ground-based GW detectors [194]. The authors provided 3.5PN analytic waveforms accurate to first order in CoM acceleration for non-spinning compact objects, and presented Fisher forecasts and Bayesian parameter inference on GW170817 and GW190425. Their analytic results agree with ours, although we will present new analytic waveforms that include the effects from component spins aligned with the orbital angular momentum. In addition, we will provide analytic formulae for the Cramér-Rao (CR) bound, quantify the number of observed orbital cycles due to CoM acceleration for all given PN orders, and demonstrate that the CoM acceleration is degenerate with the component spins at a comparable level with the chirp mass and the reduced mass. We explicitly demonstrate that neglecting spin would decrease the CR bound on CoM acceleration by a factor of two. Doing so could lead to false detection, even if the inferred spin is centered around zero. In summary, we rigorously quantify, using Fisher information, the detectability of the CoM acceleration effect at forthcoming ground-based GW observatories (Advanced LIGO A+, Cosmic Explorer, and Einstein Telescope) and present analytical formulae that are broadly applicable and have yet to appear in the literature.

The chapter is organized as follows. In Section 3.2, we present an analytic, frequency-domain model for the GW phase, which incorporates the CoM acceleration of the inner binary induced by a distant tertiary up to the third PN order. In Section 3.3, we present a statistical framework based on Fisher information in which we forecast the detectability of CoM acceleration. The results for forthcoming ground-based GW detectors will be given in Section 3.4. We will give concluding remarks in Section 3.5. We set $G = c = 1$ throughout.

3.2 Model Incorporating Small Center-of-Mass Acceleration

This section presents our GW phase model, which incorporates the CoM acceleration of an inspiraling binary on a circular orbit, embedded in a hierarchical triple system. The relative motion of the two bodies, which decouples from the CoM acceleration because the binary CoM is in free fall, is given by the standard two-body GR dynamics. We use the analytic PN phase of the standard two-body problem [33] to derive the observed wave phase.

The inspiraling binary has a line-of-sight acceleration:

$$a_\parallel = (M_3/r^2)\, \hat{l} \cdot \hat{r}, \tag{3.1}$$

where M_3 is the tertiary mass, r is the distance between the binary and the tertiary, $\hat{l}$ is a unit vector along the line of sight, and $\hat{r}$ is a unit vector pointing from the binary CoM to the tertiary. The GW signals from inspiraling compact binaries detected by ground-based observatories would last for no more than $\mathcal{O}(10^3)$ seconds, so we assume that $a_\parallel$ is approximately constant during the event.

We now correct the observed time-domain orbital phase due to $a_\parallel$:

$$\phi_\alpha(t) = \phi_0\left(t + \alpha(t-T)^2\right), \tag{3.2a}$$

$$\alpha = \frac{a_\parallel}{2} = 9.9\times 10^{-12}\,\mathrm{s}^{-1}\left(\frac{M_3}{M_\odot}\right)\left(\frac{1\ \mathrm{AU}}{r}\right)^2, \tag{3.2b}$$

where $\phi_\alpha(t)$ and $\phi_0(t)$ are the orbital phases with and without the CoM acceleration, respectively, and we have restored physical units in $\alpha = a_\parallel/2c$ for the second line. The time constant T corresponds to the choice of a reference time. See Section 3.6 for details on how T is chosen and how $\phi_\alpha(t)$ can be evaluated as a perturbative series in α.

The frequency-domain waveform is the Fourier transform of the time-domain GW waveform [66],

$$h_\alpha(t) = \mathrm{Re}\left[A(t)\,e^{2\,i\,\phi_\alpha(t)}\right]. \tag{3.3}$$

In this work, we neglect corrections to the wave amplitude $A(t)$ due to CoM acceleration, although it has been calculated to first order in α [184]. See Ref. [44] and references therein for details on how the time dependence of the amplitude can be treated.

We analytically calculate the Fourier transform using the stationary phase approximation (SPA). This approach results in the widely used "Taylor" models, in which the orbital phase of the binary is obtained by integrating the bound state energy divided by the gravitational radiation flux, written as a PN expansion, and then using the SPA (see [33, 44, 37, 149] and Section 3.6 for further details). The result is

$$\begin{aligned}\psi_\alpha(f) = 2\pi f\,t_c - \phi_c - \frac{\pi}{4}\\ + x^{-5/2}\sum_{n=0}^{6}\underbrace{x^{n/2}\left(P_n + S_n + \alpha\,A_n\,x^{-4}\right)}_{n/2\ \mathrm{PN}}\\ + \mathcal{O}(\underbrace{\alpha^2}_{\text{“quadratic”}},\underbrace{x}_{\geq 3.5\ \mathrm{PN}}),\end{aligned} \tag{3.4}$$

where $x = (\pi\,M\,f)^{2/3}$ is the PN expansion parameter, the underbrace in the sum denotes the PN order of the term, and the "quadratic" underbrace below $O\left(\alpha^2\right)$ denotes higher order corrections in α. The time constant t_c and phase constant ϕ_c correspond to the point of coalescence.

The coefficients P_n, S_n, and A_n are given explicitly in Section 3.6 (see Eq. (3.24)). In the expressions for these coefficients are the binary's (redshifted) reduced mass $\mu = (1+z)\,m_1\,m_2/M$, the (redshifted) chirp mass $\mathcal{M} = (1+z)\,\mu^{3/5}\,M^{2/5}$, and $-1 \leq \chi_1, \chi_2 \leq 1$ are dimensionless spins of the binary, each assumed to be parallel to the orbital angular momentum for simplicity. Here $M = m_1 + m_2$ is the binary total mass.

The frequency-domain GW waveform is then

$$h(f) = \mathcal{A}\,f^{-7/6}\,e^{i\,\psi_\alpha(f)}, \tag{3.5}$$

where $\mathcal{A}$ is an overall amplitude normalization constant. The factor of $f^{-7/6}$ comes from the SPA and dependence on the chirp mass has been absorbed into $\mathcal{A}$ (see Section 3.6 as well as [66, 44] and references therein). From Eq. (3.4), we see that α affects the entire frequency spectrum of the GW phase, whereas sky position manifests as a constant phase change, which is inferred by comparing strain signals recorded in multiple detectors [66]. For simplicity, in the following discussion we treat the GW detection process as if there is only one detector. To account for multiple detectors, we can rescale the amplitude constant $\mathcal{A}$ to match the network SNR. In this way, we essentially assume that the CoM acceleration does not affect the inference of extrinsic parameters such as sky location and binary position angle.

We now discuss three features and caveats of this analytic waveform model. First, the corrections due to acceleration appear at $\mathcal{O}\left(f^{-8/3}\right)$ relative to the non-acceleration terms. The effect of CoM acceleration on the phase is therefore most pronounced at low frequencies. The importance of the low frequency GW signal can be understood by calculating the number of wave cycles that arise from contributions of the usual TaylorF2 terms, P_n and S_n, and from acceleration, A_n, as a function of the minimum frequency observed at each order in the PN expansion (see Eq. (3.15) for how one derives the observed orbital phase $\phi_\alpha(f)$).

The number of cycles is defined by

$$\mathcal{N} = \frac{\phi_\alpha\left(f_{\mathrm{I}SCO}\right) - \phi_\alpha\left(f_{\mathrm{m}in}\right)}{\pi}, \tag{3.6}$$

where $f_{\mathrm{I}SCO} = 1/6^{3/2}\pi M$ is the orbital frequency at an approximate innermost stable circular orbit (ISCO). The values for $\mathcal{N}$ are given in Table 3.1. There, we calculate the number of cycles, at each order in the PN expansion, for two values of $f_{\mathrm{m}in}$, 10 Hz and 1 Hz. Each column lists the contributions from the P_n, S_n, and A_n terms.

For $f_{\mathrm{m}in} = 10\,\mathrm{Hz}$, the frequency at which seismic noise is expected to limit the sensitivity of advanced LIGO [15], acceleration contributes less than one cycle unless $\alpha \gtrsim 10^{-7}\,\mathrm{s}^{-1}$; however, our model, accurate to first order in α, would not be valid for such large α values for binary NS inspirals (see Section 3.7 and Figure 3.2). If the lowest frequency is set to 1 Hz, acceleration then contributes tens of thousands of detectable orbital cycles for $\alpha \leq 10^{-7}\,\mathrm{s}^{-1}$ and many cycles for higher orders in the PN expansion, so they are necessary for a complete parameter inference study. The more sensitive a GW detector is at low frequencies, the more capable it is to detect CoM acceleration, which implies that third-generation detectors are much more promising than current LVK detectors for CoM inference. Our results for $f_{\mathrm{m}in} = 10\,\mathrm{Hz}$ reproduce Tables 3 and 4 in [33] and Table 1 in [148]. We further note that decreasing $f_{\mathrm{m}in}$ from 10 Hz to 1 Hz results in at least an order of magnitude more observable cycles from the P_n and S_n terms, but four to five orders of magnitude increase in the CoM acceleration terms. The spin dependent terms in A_n also result in many cycles, so they must be included to accurately model the waveform [65].

Second, we have assumed binary inspiral during the entire duration of the GW signal. Since the merger and ringdown phases are very shortlived compared to inspiral, the latter phase provides almost all the information about CoM acceleration. For BBHs, it has been

PN Order	P_n	S_n	A_n
	$f_{\min} = 10$ Hz		
0	1.6×10^4	-	$5.4 \times 10^7 \alpha$
1	4.4×10^2	-	$2.1 \times 10^6 \alpha$
1.5	-2.1×10^2	$66\,(\chi_1 + \chi_2)$	$(-7.5 + 2.4\,\chi_1 + 2.4\,\chi_2) \times 10^5 \alpha$
2	9.9	-	$4.4 \times 10^4 \alpha$
2.5	-11	$9.3\,(\chi_1 + \chi_2)$	$(-3.1 + 1.8\,\chi_1 + 1.8\,\chi_2) \times 10^4 \alpha$
3	2.6	$-4.0\,(\chi_1 + \chi_2)$	$(4.4 - 4.6\,\chi_1 - 4.6\,\chi_2) \times 10^3 \alpha$
	$f_{\min} = 1$ Hz		
0	7.4×10^5	-	$1.2 \times 10^{12} \alpha$
1	4.4×10^3	-	$9.6 \times 10^9 \alpha$
1.5	-1.0×10^3	$3.1 \times 10^2\,(\chi_1 + \chi_2)$	$(-16 + 5.1\,\chi_1 + 5.1\,\chi_2) \times 10^8 \alpha$
2	24	-	$4.4 \times 10^7 \alpha$
2.5	-17	$13\,(\chi_1 + \chi_2)$	$(-14 + 8.3\,\chi_1 + 8.3\,\chi_2) \times 10^6 \alpha$
3	2.7	$-4.5\,(\chi_1 + 4.5\,\chi_2)$	$(0.81 - \chi_1 - \chi_2) \times 10^6 \alpha$

Table 3.1: Contribution to the number of observed cycles as a function of α [s^{-1}], calculated via Eqs. (3.6) and (3.15), of the orbital phase for a binary with $m_1 = m_2 = 1.4 M_\odot$ for two values of $f_{\min}$. The left-most column denotes the PN order of the contributing waveform cycles, while the second, third, and fourth columns denote the contribution from the P_n, S_n, and A_n terms, respectively, see Eqs. (3.4) and (3.24) (note that there are both spin-independent and dependent terms within A_n). We consider two values for $f_{\min}$, 10 Hz in the first tabular block and 1 Hz in the second. The highest frequency for the orbit is taken to be $f_{ISCO} = 1/\left(6^{3/2}\pi M\right)$, the ISCO for a massive test particle in Schwarzschild spacetime, for all cases. It is clear that the number of cycles arising from CoM acceleration dramatically increases as the minimum frequency is decreased. Therefore, sensitivity improvements at low frequencies greatly enhance the detectability of α. For the lowest minimum frequency, $f_{\min} = 1$ Hz, CoM acceleration can contribute at least one cycle so long as $\alpha \gtrsim 10^{-12}$ s^{-1}. We see also that the 2.5 PN terms can contribute a cycle for $\alpha \sim 10^{-7}$ s^{-1}, but accelerations that are much larger requires considering $O(\alpha^2)$ in Eq. (3.4), see Section 3.7. Note these values are independent of detector sensitivity.

shown that using inspiral models for full inspiral-merger-ringdown (IMR) events yields parameter posteriors that are consistent with using IMR models [86, 87]. Other studies have demonstrated how one would carry out a numerical analysis of a time-dependent phase delay, similar to ours, for full IMR events [54]. Our simplifying treatment should be valid except for the very massive BBH events.

Third, we have only incorporated the effect of acceleration at the linear order in α. Our model, Eq. (3.4), is of the form $\psi_\alpha(f) = \psi_0(f) + \alpha\,\psi_1(f) + \alpha^2\,\psi_2(f) + \ldots$, with $\psi_2(f)$ and all higher-order pieces neglected. This is valid provided $|\alpha| \ll |\psi_1(f)/\psi_2(f)|$. We investigate this assumption in Section 3.7. We find that for binaries with $m_1 = m_2 = 1.4\,M_\odot$, the quadratic term becomes important only for rather large acceleration values $\alpha \gtrsim 6\times10^{-7}\,\mathrm{s}^{-1}$.

We are now in a position to address the data analysis of [92], in which a CoM acceleration posterior with mean $\alpha \approx 10^{-3}\ \mathrm{s}^{-1}$ and standard deviation $\sim 10^{-3}\ \mathrm{s}^{-1}$ are inferred from GW190814. This result is consistent with zero CoM acceleration and therefore is compatible with the null hypothesis that the source is not undergoing CoM acceleration. The signal entered the LIGO Livingston detector at around 30 Hz [11]. According to Eq. (3.6), the number of cycles contributed by CoM acceleration for an event with $f_{\mathrm{m}in} = 30$ Hz is $2.13 \times 10^2\,\alpha$ at the Newtonian order and $7.95 \times 10\,\alpha$ at 1 PN order. This is an insufficient number of cycles to detect astrophysically plausible values $\alpha \ll 10^{-3}\,\mathrm{s}^{-1}$, consistent with the result of [92].

In the remainder of the chapter, we forecast the precision with which α can be measured from GW data. To this end, we discuss the Fisher information formalism and detector sensitivities in the next Section.

3.3 Framework for Parameter Estimation

We now summarize the framework we use to predict the precision of parameter inference using our model. In Section 3.3.1, we introduce the Fisher information matrix. This enables enables us to forecast a lower bound for posterior variances that would be obtained by Markov-Chain Monte-Carlo (MCMC) techniques [59]. Detector sensitivities for the third-generation detectors of interest are given in Section 3.3.2.

3.3.1 Fisher Information and the Posterior Covariance

The Fisher information formalism has been widely used to quantify parameter inference precision in GW science. We refer the readers to [77, 148, 66, 99, 169] and references therein for further information and we proceed by defining quantities needed for our analysis.

When a signal is present, GW strain data can be decomposed as, $s(f) = h\left(f;\hat{\theta}\right) + n(f)$, where $h\left(f;\hat{\theta}\right)$ is a GW waveform, θ is a placeholder for the entire set of source parameters, and $\hat{\theta}$ denotes the parameter values that best fit the data for given detector noise $n(f)$. The detector noise $n(f)$ is assumed to be stationary, colored Gaussian noise characterized by the one-sided power spectral density (PSD) $S_n(f)$. Because $\hat{\theta}$ depends on the noise realization $n(f)$, it is also a random variable with mean equal to the source's true parameter value [99].

For a sufficiently high signal-to-noise ratios (SNR), the likelihood function for the parameters θ^a has a Gaussian form

$$L\left(\theta \middle| s\right) \propto \exp\left[-\frac{1}{2}\,\Gamma_{ab}\,\delta\theta^a\,\delta\theta^b\right], \tag{3.7a}$$

$$\Gamma_{ab} = \left\langle \frac{\partial h}{\partial \theta^a}, \frac{\partial h}{\partial \theta^b} \right\rangle \Bigg|_{\theta=\hat{\theta}}, \tag{3.7b}$$

$$\left\langle \frac{\partial h}{\partial \theta^a}, \frac{\partial h}{\partial \theta^b} \right\rangle = \mathrm{Re}\left[4\int_0^\infty \frac{\frac{\partial h}{\partial \theta^a}\frac{\partial h^*}{\partial \theta^b}}{S_n(f)}\,\mathrm{d}f\right], \tag{3.7c}$$

where Γ_{ab} is the Fisher information matrix, $\delta\theta^c$ is the difference between a given parameter θ^c and the posterior's mean, $\langle \cdots \rangle$ denotes the standard inner product between two frequency domain signals, and $S_n(f)$ is the PSD of the detector under consideration [66, 77, 148, 169, 59]. See [77, 66] and references therein for details about this framework.

The likelihood function in Eq. (3.7a) is a multivariate Gaussian whose covariance matrix is the inverse of the Fisher matrix,

$$\Sigma = \Gamma^{-1}. \tag{3.8}$$

The a^{th} diagonal entry of Σ is a lower bound on the variance in the estimation of the parameter θ_a,

$$\langle \Delta\theta_a^2 \rangle_n = \Sigma_{aa}, \tag{3.9}$$

where here the angled brackets and subscript n indicates an averaging over detector noise realizations. This lower bound is referred to as the *Cramér-Rao (CR) bound*, which is the minimum standard deviation that can be achieved with an unbiased estimator [66, 169, 148]. We will also make use of the correlation coefficient $\mathcal{C}^{ab}$, defined as

$$\mathcal{C}^{ab} = \Sigma^{ab}/\sqrt{\Sigma^{aa}\,\Sigma^{bb}}. \tag{3.10}$$

This quantifies how errors in estimating different parameters are correlated [66, 148] and it is useful in identifying parameter degeneracy.

3.3.2 Detector Sensitivities

The low frequency portion of the GW signal has the most information about CoM acceleration (see Eq. (3.4) and Table 3.1), which implies that third-generation detectors, designed to have reduced low-frequency noise (see Fig. 3.1), are particularly promising sites to detect α. We therefore consider advanced LIGO A Plus (aLIGO A+) [26], Cosmic Explorer (CE) [109], and Einstein Telescope (ET) [154].

For ET, we use the ET-D sensitivity curve (see [95] for a discussion of the various ET configurations). The available PSD curve for ET-D goes down to a frequency of 1 Hz. However, sensitivity projections for both CE and aLIGO A+ are only available down to 5 Hz. We numerically extrapolate the logarithm of the aLIGO A+ and CE PSD curves down to 1 Hz. We use a quadratic extrapolation for aLIGO A+ and a cubic extrapolation for CE. We nevertheless find that using these extrapolated PSDs below 5 Hz make insignificant differences in the numerical results of the Fisher forecast because the noise level rapidly increases by several orders of magnitude over a few Hz.

In Figure 3.1, these PSDs are shown with aLIGO A+ in black, ET-D in purple, CE in blue, and an estimate for the recent LIGO Livingston PSD in red. The solid curves are official projections and the dashed curves are our extrapolations to very low frequencies. The LIGO Livingston PSD is estimated with `gwpy.timeseries` [124] and built-in routines for PSD estimation on a strain data series in the Livingston detector (we use 2048 seconds of data beginning 1 second after GW200316). In the next section, we use these PSDs to calculate the covariance matrix Eq. (3.8) and thus forecast the detectability of the acceleration parameter α.

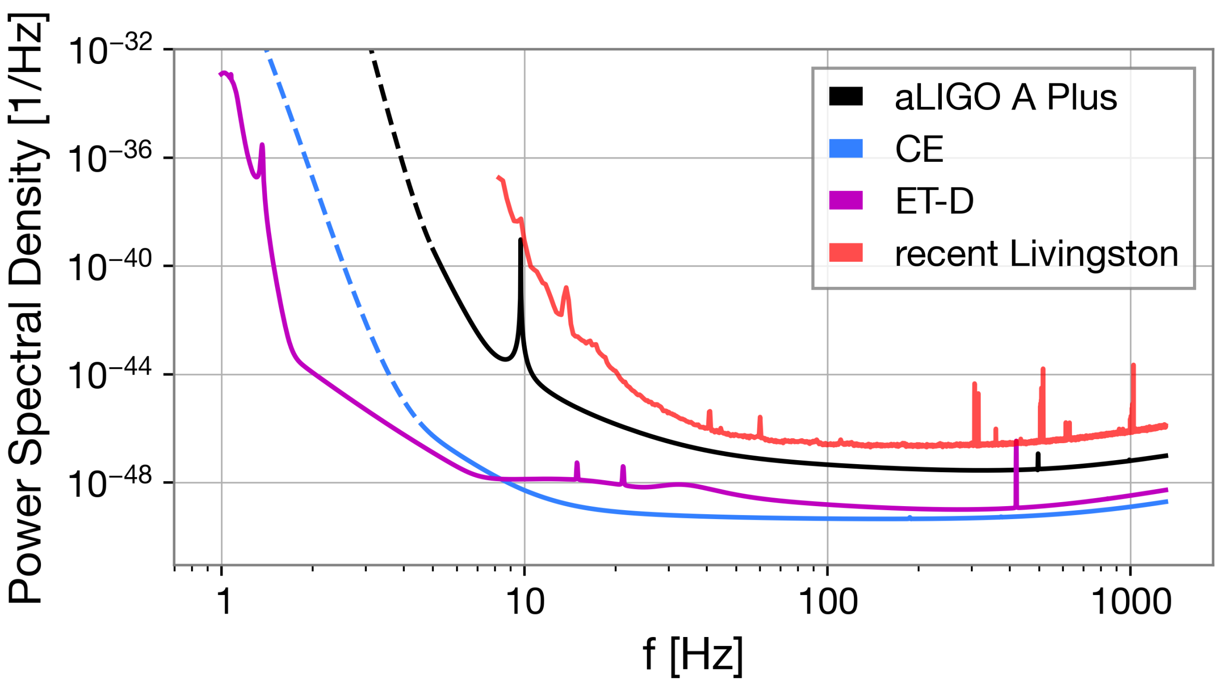

Figure 3.1: PSD projections used in our calculations for three third-generation ground-based GW detectors: aLIGO A+ (black), ET-D (magenta), and CE (blue), and an estimation for Livingston using recent data (red). References to the source of these PSD curves are given in the main text. A model for ET-D's PSD is available down to 1 Hz, while the curves for aLIGO A+ and CE are provided down to 5 Hz; we have been extrapolated them to 1 Hz (dashed curves). See text for how the recent Livingston PSD is obtained.

3.4 Results and Discussion

In this Section, we provide the results of the Fisher forecast. We begin with Section 3.4.1, in which we provide an analytic explanation about how $\Delta\alpha$ is expected to scale as a function of other parameters. We continue in Section 3.4.2 by presenting the fully numerical Fisher results, including the CR bound for α and discussing the degeneracy between α and other parameters. We will fit the numerical results for the CR bound of α to simple analytical formulae as motivated by the results of Sec. 3.4.1.

3.4.1 Analytic Scaling

Here, we provide an argument for how $\Delta\alpha$ is expected to scale with other parameters. According to Eqs. (3.4), (3.7b), and (3.24), we see that

$$\frac{\Delta\alpha}{\alpha} \propto \frac{\mathcal{M}^{10/3}}{\rho\,\alpha}, \tag{3.11}$$

where ρ is the SNR. This is derived by considering $\Delta\alpha/\alpha = \sqrt{\Sigma_{\ln\alpha\ln\alpha}} \approx 1/\sqrt{\Gamma_{\ln\alpha\ln\alpha}}$. Considering just the leading order term, we have $\Gamma_{\ln\alpha\ln\alpha} \propto \alpha^2\mathcal{A}^2\,A_0^2\,x^{-13} \propto \alpha^2\rho^2/\mathcal{M}^{20/3}$ (recall that $\mathcal{A}$ is the frequency domain signal amplitude, Eq. (3.5)) [65]. This relation is inexact for a few reasons. First, inverting the Fisher matrix Γ to obtain Σ depends on the off-diagonal elements of Γ, as well as the higher-order corrections in the phase that are proportional to the A_n coefficients. Second, evaluating the Fisher matrix requires integrating between a minimum frequency and the ISCO frequency (see the paragraph below Eq. (3.7b)), and the ISCO frequency itself is a function of the chirp mass $\mathcal{M}$. Nonetheless, we find that the analytic scaling result is a fair approximation (see Fig. 3.2).

This relation provides a few noteworthy insights. First, it implies that $\Delta\alpha$ is roughly constant at fixed SNR as a function of α. This is consistent with Eq. (3.4) because we consider only $O(\alpha)$ corrections in our model; differentiating $h(f)$ in Eq. (3.5) with respect to α does not bring any additional powers of α into the integrand of Eq. (3.7b). Second, it implies that the CoM acceleration is most detectable for a binary with a small chirp mass.

3.4.2 Numerical Results

We now report our numerical results for the Fisher matrix calculation on the entire set of parameters, $\{\ln\alpha, \ln\mathcal{M}, \ln\mu, \chi_1, \chi_2, t_c, \phi_c\}$. We also provide results that correspond to some of these parameters held fixed. We use the logarithms of α, $\mathcal{M}$ and μ to avoid ill-conditioned matrices (see [96] for a discussion of when ill-conditioning might occur when numerically evaluating the Fisher matrix). We set a fiducial SNR $\rho = 10$, which corresponds to the majority of detectable GW events close to the detection threshold of matched filtering. All parameter derivatives are evaluated for equal mass binaries with $\mathcal{M}_{\mathrm{b}Ns}/2 \leq \hat{\mathcal{M}} \leq 30\,M_\odot$ (where $\mathcal{M}_{\mathrm{b}Ns}$ is the chirp mass for an neutron star binary with $m_1 = m_2 = 1.4M_\odot$), $\hat{\mu} = 2^{-4/5}\hat{\mathcal{M}}$ corresponding to an equal mass binary, and $\hat{\chi}_1 = \hat{\chi}_2 = \hat{t}_c = \hat{\phi}_c = 0$ (we hereafter drop the hats). Note that $\mathcal{M}_{\mathrm{bNs}}/2$ corresponds to a binary with component masses $m \approx 0.7\, M_{\odot}$. In agreement with Eq. (3.11), we find that varying the true value of α hardly affects the CR bound. Even changing α by orders of magnitude only alters the value of $\Delta\alpha$ by, at most, 0.1%, except when α have very large values $\sim 10^{-4}$ s^{-1} and our perturbative phase model becomes inapplicable.

Although inexact, Eq. (3.11) provides useful analytic guidance for $\Delta\alpha$ as a function of $\mathcal{M}$. We therefore fit

$$\Delta\alpha_i = c_i \left(\frac{10}{\rho}\right) \mathcal{M}^{e_i}, \tag{3.12}$$

to our numerical Fisher forecast for $\Delta\alpha = \sqrt{\Sigma_{\alpha\alpha}}$ according to Eq. (3.8). We expect that the exponents e_i will equal 10/3 only when all other parameters are fixed. This is because the CR bound is calculated by inverting the entire Fisher matrix, whereas Eq. (3.11) comes from fixing all other parameters, considering the Fisher matrix to be a scalar, $\Gamma_{\alpha\alpha}$. The parameters to be fit, c_i and e_i, depend on the specific detector under consideration, which we label using the index i. Note that the units of c_i is s$^{-1-e_i}$ and e_i is dimensionless.

For the sensitivities given in Fig. 3.1, the obtained values for c_i and e_i are shown in Table 3.2 for the full range $\mathcal{M}_{\mathrm{bNS}}/2 \leq \mathcal{M} \leq 30\, M_{\odot}$; each tabular block in Table 3.2 corresponds to different parameters being fixed, which is implemented by removing from the Fisher matrix rows and columns corresponding to those parameters. As mentioned above, the exponents e_i approach 10/3 when other parameters are fixed, although they deviate from this value by, at most, 10%. We see that c_i decreases by a factor of two depending on whether or not aligned spin components are included as parameters in the waveform model.

The numerical results are shown, alongside the corresponding fitting formula of Eq. (3.12), in Figure 3.2. The colored markers show the CR bounds for $\Delta\alpha$, from Eq. (3.9), as a function of the chirp mass $\mathcal{M}$ and evaluated for $\alpha = 0$. Results are shown for aLIGO A+, CE, and ET with fits to the empirical formula, Eq. (3.12), shown with the colored lines. The fits show excellent agreement with the CR bounds. The gray markers behind the colored markers (see, for instance, the ET data at low chirp masses) are the CR bounds for nonzero acceleration values $\alpha = 10^{-11}, \ldots, 10^{-6}\,\mathrm{s}^{-1}$. These heavily overlap with the colored markers because the CR bounds change by, at most 0.1%, as a function of α. The gray shades enclose the parameter space where quadratic corrections $O(\alpha^2)$ to the GW phase in Eq. (3.4) are smaller than the linear contribution for effective minimum observable frequencies at 20 Hz, 5 Hz and 2 Hz. These values are appropriate for detection at aLIGO A+, CE, and ET, respectively. See Section 3.7 for details on how this frequency affects the validity of neglecting terms quadratic in α. For all three detectors and masses shown, the detection limit calculated using our linear model is within the validity range. Note that the Fisher analysis is carried out for $f_{min} = 1$ Hz for all detectors.

A detection of CoM acceleration is possible when $\Delta\alpha/\alpha < 1$ for nonzero α; otherwise, a clear detection is not possible. We see that for light chirp masses $\mathcal{M}_{\mathrm{bNs}}/2 \leq \mathcal{M} \leq 2\, M_{\odot}$ and with a moderate SNR $\rho = 10$, detections can be made at aLIGO A+ for CoM acceleration $\alpha \sim 10^{-8}$ s^{-1}, whereas for stellar mass binaries, a CoM acceleration $\alpha \gtrsim 10^{-6}\,\mathrm{s}^{-1}$ is detectable.

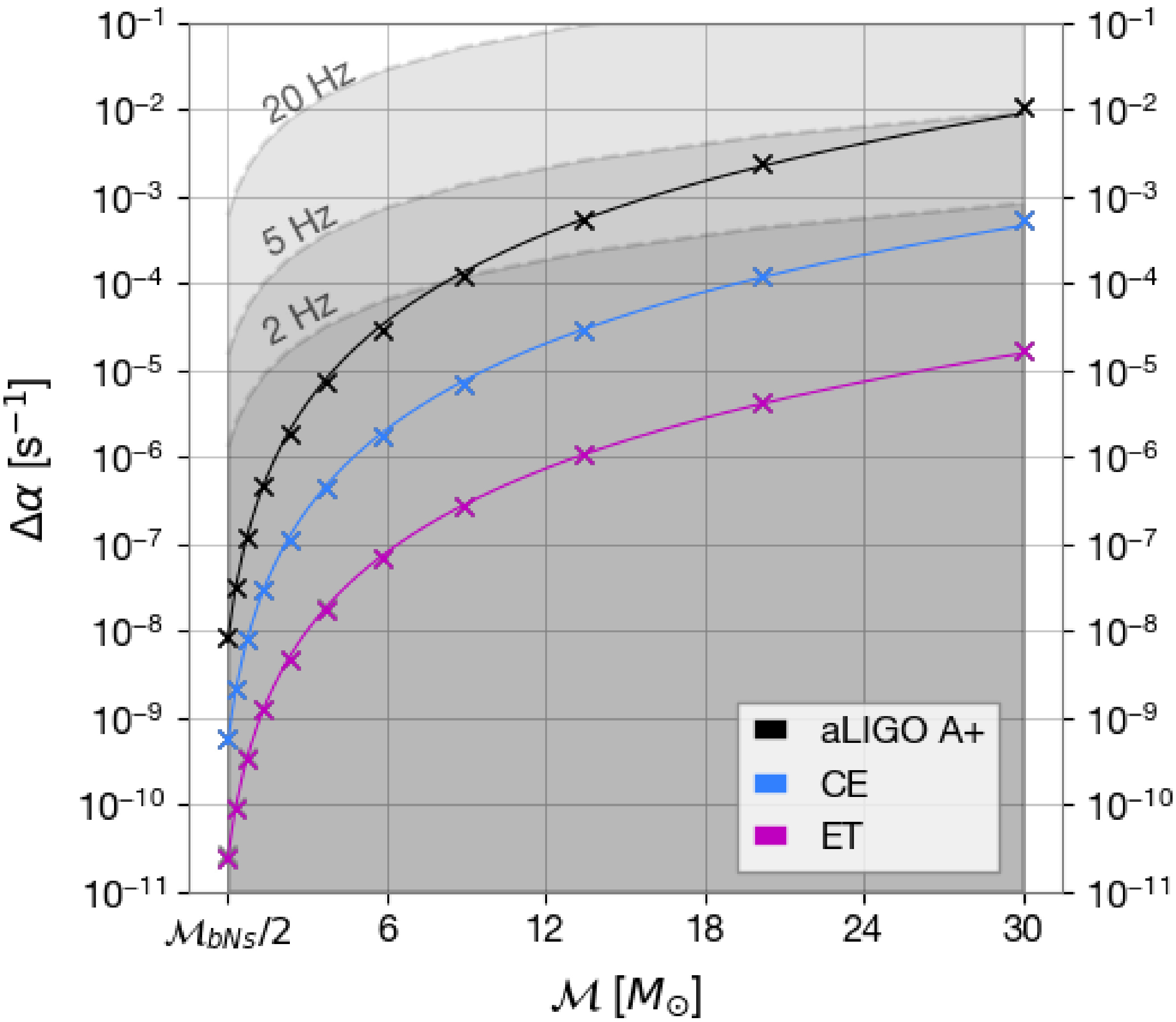

Figure 3.2: CR bound for $\Delta\alpha$ for a fiducial SNR $\rho = 10$, evaluated as a function of the chirp mass $\mathcal{M}$ and with $f_{\min} = 1$ Hz; the regions shaded in gray denote regions in which terms $\mathcal{O}(\alpha^2)$ can be safely neglected if the effective minimum observable frequency is 20 Hz, 5 Hz and 2 Hz, appropriate for aLIGO A+, CE and ET, respectively (see Section 3.7 for details on how the boundary of the shaded region is calculated based on the effective minimum observable frequency). The markers are the CR bound for each detector and under the null hypothesis $\alpha = 0$, as per Eq. (3.9). The colored curves are numerical fits to the empirical fitting formula Eq. (3.12). Behind the colored markers are gray markers (most noticeable for ET with low chirp mass), which are the CR bounds for α in the range $[10^{-11}, 10^{-6}]$ s^{-1}. Changing α over orders of magnitude alters the CR bound by at most 0.1%, but usually much less. As a result, the gray markers are hardly visible in this plot. All results here correspond to a Fisher analysis centered at parameter values $\mu = 2^{-4/5}\mathcal{M}$ and $\chi_1 = \chi_2 = t_c = \phi_c = 0$.

det.	c_i [s^{-1-e_i}]	e_i
no fixed parameters		
aLIGO A+	4.31×10^{-8}	3.60
ET	1.26×10^{-10}	3.45
CE	2.82×10^{-9}	3.53
fix $\chi_1 = \chi_2 = 0$		
aLIGO A+	2.32×10^{-8}	3.38
ET	6.95×10^{-11}	3.36
CE	1.32×10^{-9}	3.41
fix $\chi_1 = \chi_2 = t_c = \phi_c = 0$		
aLIGO A+	2.03×10^{-8}	3.27
ET	6.31×10^{-11}	3.30
CE	1.10×10^{-9}	3.31

Table 3.2: Parameter values from fitting the empirical formula Eq. (3.12) to the numerical CR bound for $\Delta\alpha$, for an event with a fiducial SNR $\rho = 10$ and $\alpha = 0$. We have used logarithmically spaced values $\mathcal{M}$ (see Fig. 3.2) and fit the natural logarithm of Eq. (3.12) to $\ln \Delta\alpha$ because the CR bound varies by orders of magnitude as a function of $\mathcal{M}$. In the top block, all parameters are given uniform priors and are marginalized over the parameter space; in the middle block, χ_1 and χ_2 are fixed to zero; in the bottom block, χ_1, χ_2, t_c, and ϕ_c are all fixed to be zero.

Owing to excellent sensitivities at low frequencies, both CE and ET hold promise in detecting CoM acceleration. The CR bound for α strongly depends on the chirp mass, as suggested by Eq. (3.11). For lighter sources with chirp masses less than $3\,M_\odot$, ET will be sensitive to $\alpha \sim (10^{-11}\text{–}10^{-9})\ \mathrm{s}^{-1}$, and CE will be sensitive to $\alpha \sim (10^{-9}\text{–}10^{-7})\,\mathrm{s}^{-1}$. For heavier BBH sources, ET will be sensitive to $\alpha \sim (10^{-8}\text{–}10^{-6})\ \mathrm{s}^{-1}$ and CE will be sensitive to $\alpha \sim (10^{-7}\text{–}10^{-5})\,\mathrm{s}^{-1}$. For GW events with higher SNR values, lower values of α can be detected according to Eq. (3.12).

Incorporating Eq. (3.2b), we can use the CR bounds of Fig. 3.2 to determine values of the tertiary mass and distance for which CoM acceleration is detectable. ET is sensitive to a tertiary perturber with mass and distance satisfying $(M_3/M_\odot)\,(1\ \mathrm{AU}/r)^2 \gtrapprox 10/\mathrm{SNR}$, CE can detect if this ratio is $\gtrapprox 10^3/\mathrm{SNR}$, and aLIGO A+ for $\gtrapprox 10^4/\mathrm{SNR}$. Therefore, our analysis indicates that detecting CoM acceleration with the third-generation detectors on the ground is possible for a stellar-mass tertiary in compact bound systems with a size $\lesssim 1\,\mathrm{AU}$.

The above results can be gleaned from Table 3.2. That table additionally shows how the detectability of α improves if the spins of the compact objects are fixed (for instance if we believe the binary compact objects are non-spinning). In this case, the CR bound is improved by about a factor of 2, and the possibility of detecting the effect of a CoM acceleration becomes even more promising.

det. \ param.	$\mathcal{M}$	μ	χ_1	χ_2	t_c	ϕ_c
aLIGO A+	0.86	-0.78	-0.75	0.75	0.62	-0.72
CE	0.88	-0.81	-0.74	0.74	0.58	-0.73
ET	0.84	-0.76	-0.66	0.66	0.50	-0.66

Table 3.3: Correlation coefficients, $\mathcal{C}_{\alpha\theta^b}$ (defined in Eq. (3.10)), between the CoM acceleration parameter α and parameter θ^b, evaluated for each of the three third-generation GW detectors, for $\mathcal{M} = \mathcal{M}_{\rm bNS}$, and $\alpha = 0$. We see that α has large correlation coefficients with the other parameters, with $\mathcal{M}$ having the largest correlation of $C_{\alpha\mathcal{M}} \approx 0.8$ across all detectors. These correlation coefficients are sufficiently large to bias inferred parameter values away from their true values if a phase model without accounting for the effect of CoM acceleration is used applied to an acceleration GW source, see text.

The degeneracy between α and the other parameters can be quantified through the correlation coefficients, which are defined in Eq. (3.10). These dimensionless numbers, $\mathcal{C}_{ab}$, are between -1 and 1 by definition and indicate the extent to which the errors in estimating two different parameters θ^a and θ^b are correlated. Typically, values $|\mathcal{C}_{ab}| > 0.9$ are taken to be indications of strong correlations and imply that a linear combination of the two parameters can be measured significantly more accurately than what can be done for θ^a and θ^b separately [66]. Nonetheless, the correlations appearing in Table 3.3 imply that excluding α from data analysis of an event whose true α is nonzero can bias the inferred parameters (the extent to which parameters are biased is discussed in Section 3.8).

Values of $\mathcal{C}_{\alpha\theta^b}$, where the second index runs over all parameters other than α, are shown for each of the three third-generation ground-based detectors in Figure 3.3, evaluated for $\alpha = 0$ (changing the value of α by orders of magnitude hardly affects the correlation coefficients). It is clear that all parameters show significant degeneracy with α to similar degrees, with $0.5 \leq |\mathcal{C}_{\alpha\theta^b}| \leq 0.83$. It is worth noting that such degeneracy is significantly milder than that between the chirp mass $\mathcal{M}$, the reduced mass μ, and component spins, which tends to be equal to ± 1 up to three or four significant digits (e.g. [148]). The mild degeneracy between α and the other parameters comes from the fact that α corrects the waveform phase at $\mathcal{O}\left(f^{-8/3}\right)$ relative to the usual PN terms, which depend on the various other parameters. In other words, the α correction to the waveform phase scales uniquely with frequency compared to the PN terms, which provide information on all other parameters. This weak degeneracy implies that if one observes an event where the source has a CoM acceleration, but a non-acceleration waveform model is used for parameter inference, the inferred component masses and spins will deviate from their true values. This statement is explored through both an injection analysis and a semi-analytic argument in Section 3.8.

3.5 Chapter 3 Conclusion

We have presented an analytic frequency-domain model for the gravitational waveform phase of an inspiraling compact binary system whose CoM is accelerating relative to the observer. Our model is valid to first order in the acceleration and it can be easily generalized to incorporate higher order effects. See Section 3.6 for a derivation of our model, including how to incorporate higher order effects, and Section 3.7 for a discussion of the range of validity of the linear approximation. We have shown that the acceleration appears as a correction at $\mathcal{O}\left(f^{-8/3}\right)$ compared to the intrinsic PN phase terms, see Eq. (3.4). Therefore, improvements of detector sensitivity at low frequencies at ground-based GW observatories will be pivotal for the detection of CoM acceleration. We have demonstrated, in particular, that the Einstein Telescope's focus on mitigating low-frequency seismic noise with the underground design, see Fig. 3.1, will make it the ideal detector for CoM acceleration, see Fig. 3.2 and Table 3.2. This chapter presents the first analytic phase model up to 3PN order, which can readily be implemented in existing parameter estimation suites.

Through a Fisher information calculation, we have constrained the values of SNR and CoM acceleration that are detectable for third-generation GW detectors on the ground. The main conclusions of our chapter can be summarized with Eq. (3.2b), Eq. (3.12), Table 3.2, and Fig. 3.2. These imply that for binaries with chirp mass $\mathcal{M}_{\rm bNs}/2$, ET can detect tertiary perturbers with mass and distance satisfying $(M_3/M_\odot)\,(1\ \mathrm{AU}/r)^2 \gtrapprox 10/\mathrm{SNR}$, CE can detect if this ratio is $\gtrapprox 10^3/\mathrm{SNR}$, and aLIGO A+ for $\gtrapprox 10^4/\mathrm{SNR}$.

The imprint of CoM acceleration in the GW signal will be one of the promising new signatures to look for at third-generation ground-based GW detectors [153]. We have created a GW template incorporating this effect to help usher in the detection of hierarchical triple compact object systems with GWs. As such, our model is a simple case in which two compact objects inspiral as they, together, orbit a massive tertiary body. This model can be further built upon by including Newtonian and post-Newtonian three-body perturbations, as well as eccentricity. Eccentricity is of particular interest because hierarchical three-body systems are known to undergo Kozai-Lidov oscillations, in which an inner binary's eccentricity oscillates in coherently with the outer binary's inclination in such a way that the total angular momentum of the system is conserved [134]. In the context of our model, a nonzero CoM for an eccentric binary would imply a smoking gun for a triple system. These will be directions of future research.

3.6 Outline of Derivation

Here we outline how to obtain the GW phase starting from PN expressions of the energy flux radiated from a circular binary, $\mathcal{F}$, and the bound state energy, $\mathcal{E}$:

$$\mathcal{F} = x^{5/2} \sum_i F_{i/2}\, x^{i/2}, \quad \mathcal{E} = \sum_i E_{i/2}\, x^{i/2},$$

where $x = (M\,\omega)^{2/3}$ is the usual PN expansion parameter and ω is the angular orbital frequency. See Eqs. (232) and (314) of [33] for values of $F_{i/2}$ and $E_{i/2}$ for non-spinning sources and Eqs. (414) and (415) of [33] for spin-orbit coupling. We neglect all terms quadratic in the spins, which arise from the spin-spin dynamics at leading-order and spin-orbit dynamics at next-to-leading-order.

The orbital dynamics are then determined by radiation reaction considerations [149],

$$\frac{\mathrm{d}\mathcal{E}}{\mathrm{d}t} = -\mathcal{F}. \tag{3.13}$$

The chain rule gives $\mathrm{d}\mathcal{E}/\mathrm{d}t = (\mathrm{d}\mathcal{E}/\mathrm{d}x)/(\mathrm{d}x/\mathrm{d}t)$ and we can solve for $t(x)$ by integrating

$$t(x) - t_c = \int_\infty^x \frac{\mathrm{d}\mathcal{E}(x')/\mathrm{d}x'}{\mathcal{F}(x')}\,\mathrm{d}x'. \tag{3.14}$$

This can be easily evaluated by expanding the integrand as PN expansion in x. Note that this expression can be inverted as a power series in order to obtain $x(t)$.

The orbital phase is

$$\phi(x) - \phi_c = \int_{t_c}^t \omega(t')\,\mathrm{d}t' = \frac{1}{M}\int_{t_c}^t x^{3/2}\,\mathrm{d}t'. \tag{3.15}$$

To evaluate this expression, we invert $t(x)$ given by Eq. (3.14) to obtain

$$\begin{aligned}
x(t) = {} & \frac{1}{4}\Theta^{-1/4} + \frac{743 + 924\,\nu}{16128}\,\Theta^{-1/2} \\
& + \left(-\frac{\pi}{20} + \frac{1}{960\,M^2}\left\{\left[75\,M\,\Delta\,m_2 + 188\,m_2^2\right]\,\chi_2\left[-75\,M\,\Delta\,m_2 + 188\,m_2^2\right]\,\chi_1\right\}\right)\Theta^{-5/8} \\
& + \frac{313328 + 512421\,\nu + 437472\,\nu^2}{16257024}\,\Theta^{-3/4} + \left(\frac{\pi\,(11891 + 3052\,\nu)}{215040}\right. \\
& + \frac{1}{2580480 M^2}\left\{\left[5\,M\,\Delta\,(96473 - 6636\,\nu)\,m_2 + 4\,(357923 - 5236\nu)\,m_2^2\right]\chi_2\right. \\
& \left.\left. + \left[5\,M\,\Delta\,(6636\,\nu - 96473)\,m_1 + 4\,(357923 - 5236\,\nu)\,m_1^2\right]\,\chi_1\right\}\right)\Theta^{-7/8} \\
& + \left(\frac{1}{24034384281600}\left(-10052469856691 + 1530761379840\,\gamma_E + 1001432678400\,\pi^2\right.\right. \\
& + 24236159077900\,\nu - 882121363200\,\pi^2\,\nu - 206607970800\,\nu^2 + 462992376000\,\nu^3 \\
& \left. + 3061522759680\,\log 2 + 765380689920 \log\left(\frac{1}{4\Theta^{1/4}}\right)\right) \\
& \left. + \frac{\pi}{364 M^2}\left\{\left[-45\,M\,\Delta\,m_2 - 118\,m_2^2\right]\,\chi_2 + \left[45\,M\,\Delta\,m_1 - 118\,m_1^2\right]\,\chi_2\right\}\right)\Theta^{-1},
\end{aligned} \tag{3.16}$$

where $\Theta = \frac{\nu}{5M}\,(t_c - t)$, γ_E is the Euler-Mascheroni constant, $M = m_1 + m_2$, $\Delta = (m_1 - m_2)/M = \sqrt{1 - 4\nu}$, and $\nu = \mu/M$ is the symmetric mass ratio. This expression can be compared to Eq. 316 in [33], with which our result agrees; unlike Eq. 316 in [33], we have included spin.

and then we can evaluate the above integral by expanding $x^{3/2}$ as a PN expansion in t. Doing so yields $\phi(t)$; see Eq. (317) of [33] for the expression neglecting spin.

We obtain the waveform in the frequency domain by approximating the full Fourier transform,

$$h(f) = \int_{-\infty}^{\infty} h(t)\, e^{2\pi i f t}\, \mathrm{d}t, \tag{3.17}$$

where $h(t) = A(t)\, e^{2\,i\,\phi(t)}$, via the stationary phase approximation (SPA)

$$h(f) \approx \frac{1}{2}\, A\left(t^*(f)\right) \sqrt{\frac{\mathrm{d}f}{\mathrm{d}t}}\, \exp\left[2\pi\, f\, t^*(f) - \frac{\pi}{4} - 2\phi(t^*(f))\right], \tag{3.18}$$

where $t^*(f)$ satisfies

$$\left.\frac{\mathrm{d}\phi(t)}{\mathrm{d}t}\right|_{t=t^*(f)} = \pi\, f, \tag{3.19}$$

and it is understood that $\mathrm{d}f/\mathrm{d}t$ in Eq. (3.18) is evaluated at $t = t^*(f)$.

So far, we have not incorporated the CoM acceleration. As described in the text, we consider the case in which CoM acceleration is completely decoupled from the binary's relative dynamics. We incorporate the effect by considering the time-delayed signal

$$\phi_\alpha(t) = \phi_0\left(t + \alpha(t-T)^2\right), \tag{3.20}$$

and using this as the phase entering the Fourier transform of Eq. (3.17). We now solve for $t^*_\alpha(f)$ that satisfies

$$\left[1 + 2\,\alpha\,(t^*(f) - T)\right]\left.\frac{\mathrm{d}\phi(t)}{\mathrm{d}t}\right|_{t=t^*(f)} = \pi\, f. \tag{3.21}$$

Solving for $t^*(f)$ is then straightforward. We use the ansatz

$$\begin{aligned} t^*(f) = t_c - x^{-4}\big(t_0 + t_2\, x + t_3\, x^{3/2} + t_4\, x^2 + t_5\, x^{5/2} \\ + t_6\, x^3 + \alpha\, t_A(x)\big), \end{aligned} \tag{3.22}$$

where $x = (\pi M f)^{2/3}$, the t_{2n} are functions of the masses and spins, and $t_A(x)$ must be solved for via Eq. (3.21). At this point, letting $T = t_c$ greatly simplifies the resulting algebra. With $t^*(f)$, we can now evaluate

$$\begin{aligned} \psi_\alpha(f) &= 2\pi\, f\, t^*(f) - \frac{\pi}{4} - 2\,\phi\left(t^*(f)\right) \\ &= 2\pi\, f\, t_c - \phi_c - \frac{\pi}{4} + x^{-5/2}\sum_{n=0}^{6} x^{n/2}\left(P_n + S_n + \alpha\, A_n\, x^{-4}\right), \end{aligned} \tag{3.23}$$

where the coefficients P_n, S_n, and A_n are

$$
\begin{aligned}
P_0 &= \frac{3}{128\,\nu} \\
P_1 &= 0 \\
P_2 &= \frac{5\,(743 + 924\,\nu)}{32256\,\nu} \\
P_3 &= -\frac{3\pi}{8\nu} \\
P_4 &= \frac{15293365 + 5040\,\nu\,(5429 + 4319\,\nu)}{21676032\,\nu} \\
P_5 &= -\frac{5\pi}{64512\nu}\,(-7729 + 1092\,\nu)\,(2 + 3\ln x) \\
P_6 &= \frac{1}{200286535680\,\nu}\,\Big\{4527600\,\big[(45633 - 102260\,\nu)\nu^2 + \,432\pi^2(451\,\nu - 512)\big] \\
&\quad -24236159077900\,\nu - \,1530761379840\,\gamma + 11583231236531 - \\
&\quad 3061522759680\ln 2 - 765380689920\ln x\Big\}
\end{aligned} \tag{3.24a}
$$

$$
\begin{aligned}
S_1 &= 0 \\
S_2 &= 0 \\
S_3 &= \frac{1}{128\,M^2\,\nu}\,\Big\{\big[188\,m_1^2 - 75M\Delta\,m_1\big]\,\chi_1 + \,\big[188\,m_2^2 + 75M\Delta\,m_2\big]\,\chi_2\Big\} \\
S_4 &= 0 \\
S_5 &= \frac{5\,(2 + 3\ln x)}{193536\,M^2\,\nu}\,\Big\{\big[27\,M\Delta\,m_2\,(-2783 + 56\nu) - 22\,m_2^2\,(10079 + 252\nu)\big]\,\chi_2 \\
&\qquad + \big[27\,M\Delta\,m_1\,(2783 - 56\nu) - 22\,m_1^2\,(10079 + 252\nu)\big]\,\chi_1\Big\} \\
S_6 &= \frac{5\pi}{16\,M^2\,\nu}\,\Big\{\big[118\,m_2^2 + 45M\Delta\,m_2\big]\,\chi_2 + \big[118\,m_1^2 - 45M\Delta\,m_1\big]\,\chi_1\Big\}
\end{aligned} \tag{3.24b}
$$

$$\begin{aligned}
A_0 &= \frac{25\,M}{32768\,\nu^2} \\
A_1 &= 0 \\
A_2 &= \frac{25\,M\,(743+924\,\nu)}{4128768\,\nu^2} \\
A_3 &= -\frac{5M\,\pi}{512\,\nu^2} + \frac{5}{24576\,M\,\nu^2}\left\{\left[-75\,M\Delta\,m_1 + 188\,m_1^2\right]\chi_1 + \left[75\,M\Delta\,m_2 + 188\,m_2^2\right]\chi_2\right\} \\
A_4 &= \frac{25\,M}{2774532096\,\nu^2}\,(1755623 + 112\,\nu\,(32633+23121\,\nu)) \\
A_5 &= -\frac{5\,M\pi\,(20807+8036\,\nu)}{1376256\,\nu^2} \\
&\quad + \frac{5}{4128768\,M\,\nu^2}\left\{\left[-5M\Delta\,m_1\,(32477+8736\,\nu) + 14\,m_1^2\,(33049+8932\,\nu)\right]\chi_1\right. \\
&\qquad \left. + \left[5\,M\Delta\,m_2\,(32477+8736\,\nu) + 14\,m_2^2\,(33049+8932\,\nu)\right]\chi_2\right\} \\
A_6 &= \frac{M}{46146017820672\,\nu^2}\left\{23100\,\nu\,(3311653861 + 84\,\nu\,(2030687+1856036\,\nu))\right. \\
&\quad - 234710784\,\pi^2\,(-18944+11275\,\nu) - 28907482848623 + 4592284139520\,\gamma \\
&\quad \left. + 9184568279040\ln 2 + 2296142069760\ln x\right\} \\
&\quad + \frac{\pi}{6144\,M\,\nu^2}\left\{\left[1725M\Delta\,m_1 - 4454\,m_1^2\right]\chi_1 - \left[1725M\Delta\,m_2 + 4454\,m_2^2\right]\chi_2\right\}
\end{aligned} \tag{3.24c}$$

Our expression agrees with the result of [185] (see their Eq. (A23), in which our A_0 appears). Furthermore, our method can be compared to the numerical framework outlined by [54], which considered a time-dependent time delay for an entire inspiral-merger-ringdown signal.

3.7 Validity of Neglecting Quadratic Correction

We now address the values of α for which it is valid to truncate the expression

$$\psi_\alpha(f) = \psi_\alpha(f)\bigg|_{\alpha=0} + \frac{\partial\psi}{\partial\alpha}\bigg|_{\alpha=0}\alpha + \frac{1}{2}\frac{\partial^2\psi}{\partial\alpha^2}\bigg|_{\alpha=0}\alpha^2 + O(\alpha^3) \tag{3.25}$$

where the ψ appearing here is the phase of the SPA waveform. To make notation less cumbersome, we define $\psi_n = \partial^n\psi/\partial\alpha^n$.

We now quantify the range of α for which it is valid to neglect ψ_2, as we have done in Eq. (3.4). To derive ψ_n, we repeat the steps of Section 3.6 but we add a term $\alpha^2 t_B(x)$ in Eq. (3.22). Doing so gives the quadratic correction

$$\psi_2 = \alpha^2(B_0 x^{-21/2} + B_2 x^{-19/2} + B_3 x^{-9} + B_4 x^{-17/2} + B_5 x^{-8} + B_6 x^{-15/2}), \tag{3.26}$$

where

$$
\begin{aligned}
B_0 &= \frac{625\, M^2}{12582912\, \nu^3} \\
B_2 &= \frac{1625\, M^2\, (924\, \nu + 743)}{3170893824\, \nu^3} \\
B_3 &= -\frac{25\pi M^2}{32768\, \nu^3} \\
B_4 &= \frac{1375\, M^2}{6392521949184\, \nu^3} \left\{7475065 + 2352\, \nu\, (6997 + 4755\, \nu)\right\} \\
B_5 &= -\frac{125\pi\, M^2}{1585446912\, \nu^3} \,(86197 + 53676\, \nu) \\
B_6 &= \frac{5\, M^2}{11813380562092032\, \nu^3} \left\{-82698671170559 + 13776852418560\, \gamma \right. \\
&\quad - 704132352\, \pi^2\, (-25088 + 11275\, \nu) + 69300\, \nu\, (3572915219 + 84\, \nu\, (5819253 \\
&\quad \left. +3592540\, \nu)) + 27553704837120 \ln 2 + 6888426209280 \ln x \right\} .
\end{aligned}
\tag{3.27}
$$

These expressions neglect spin contributions because our analysis has considered true binary values of $\chi_1 = \chi_2 = 0$.

Evidently, the quadratic terms in α are of $\mathcal{O}\left(f^{-8/3}\right)$ relative to the terms linear in α and are thus $\mathcal{O}\left(f^{-16/3}\right)$ relative to the non-acceleration terms. They are, therefore, potentially impactful at low frequencies and while they may be important for large accelerations, our study has focused on the linear correction.

We have that the relation $\alpha \ll (\partial\phi/\partial\alpha)/(\partial^2\phi/\partial\alpha^2)$ can be written in the form

$$
\alpha \ll \frac{\partial\phi/\partial\alpha}{\partial^2\phi/\partial\alpha^2} = x^4(C_0 + C_2 x + C_3 x^{3/2} + C_4 x^2 + C_5 x^{5/2} + C_6 x^3), \tag{3.28}
$$

as a PN expansion, with C_{2n} being functions of A_n and B_{2n},

$$
\begin{aligned}
C_0 &= A_0/B_0 \\
C_2 &= \left(A_2 B_0 - A_0 B_2\right)/B_0^2 \\
C_3 &= \left(A_3 B_0 - A_0 B_3\right)/B_0^2 \\
C_4 &= \left(A_4 B_0^2 - A_2 B_2 B_0 + A_0 B_2^2 - A_0 B_0 B_4\right)/B_0^3 \\
C_5 &= \left(A_5 B_0^2 - A_3 B_0 B_2 - A_2 B_0 B_3 + 2A_0 B_2 B_3 - A_0 B_0 B_5\right)/B_0^3 \\
C_6 &= \left(A_6 B_0^3 - A_4 B_0^2 B_2 + A_2 B_0 B_2^2 - A_0 B_2^3 - A_3 B_0^2 B_3 \right. \\
&\quad \left. + A_0 B_0 B_3^2 - A_2 B_0^2 B_4 + 2A_0 B_0 B_2 B_4 - A_0 B_0^2 B_6\right)/B_0^4.
\end{aligned}
\tag{3.29}
$$

We can therefore get an upper bound for α by evaluating the RHS for the lightest binary considered here, with $m_1 = m_2 = 0.7 M_\odot$ (corresponding to a chirp mass $\mathcal{M}_{\rm bNs}/2$), and a minimum observing frequency of 1 Hz. Then we have that the RHS of Eq. (3.28) is equal to

2.03×10^{-7} s^{-1}. The largest term in Eq. (3.28) is $x^4\, C_0$ and so, $\psi_1/\psi_2 \propto \mathcal{M}^{5/3}$. Therefore, the upper bound on α is closest to 0 for small chirp mass and throughout our study, where the minimum $\mathcal{M}$ is $\mathcal{M}_{\rm bNS}/2$, the smallest upper bound on α is thus 2.03×10^{-7} s^{-1}. Note that the minimum observing frequency plays a role in this analysis, which we have fixed to 1 Hz in this Section. In Fig. 3.2, we present regions in which $\Delta\alpha \ll |\partial\phi/\partial\alpha|/|\partial^2\phi/\partial\alpha^2)|$ for a minimum observable frequency at 20 Hz, 5 Hz and 2 Hz, evaluated as a function of $\mathcal{M}$.

This result for $\mathcal{M} = \mathcal{M}_{\rm bNS}/2$ is numerically confirmed in Figure 3.3, where we consider the maximum value of the ratio between the quadratic correction, $\alpha^2\, \psi_2$, and the linear correction, $\alpha\, \psi_1$ for fixed $\mathcal{M} = \mathcal{M}_{\rm bNS}/2$. We see that for small α, until $\alpha \sim O\,(10^{-7}$ s$^{-1})$, the quadratic correction is (at least) an order of magnitude smaller than the linear correction. They become equal at $\alpha \approx 2.03 \times 10^{-7}$ s^{-1}, which we therefore take as the maximum possible value for α at which our model is valid for the $\mathcal{M}_{\rm bNs}/2$ system. This is the value marked by the green region in Fig. 3.2 on the $\Delta\alpha$-axis, where it is given as a function of the chirp mass.

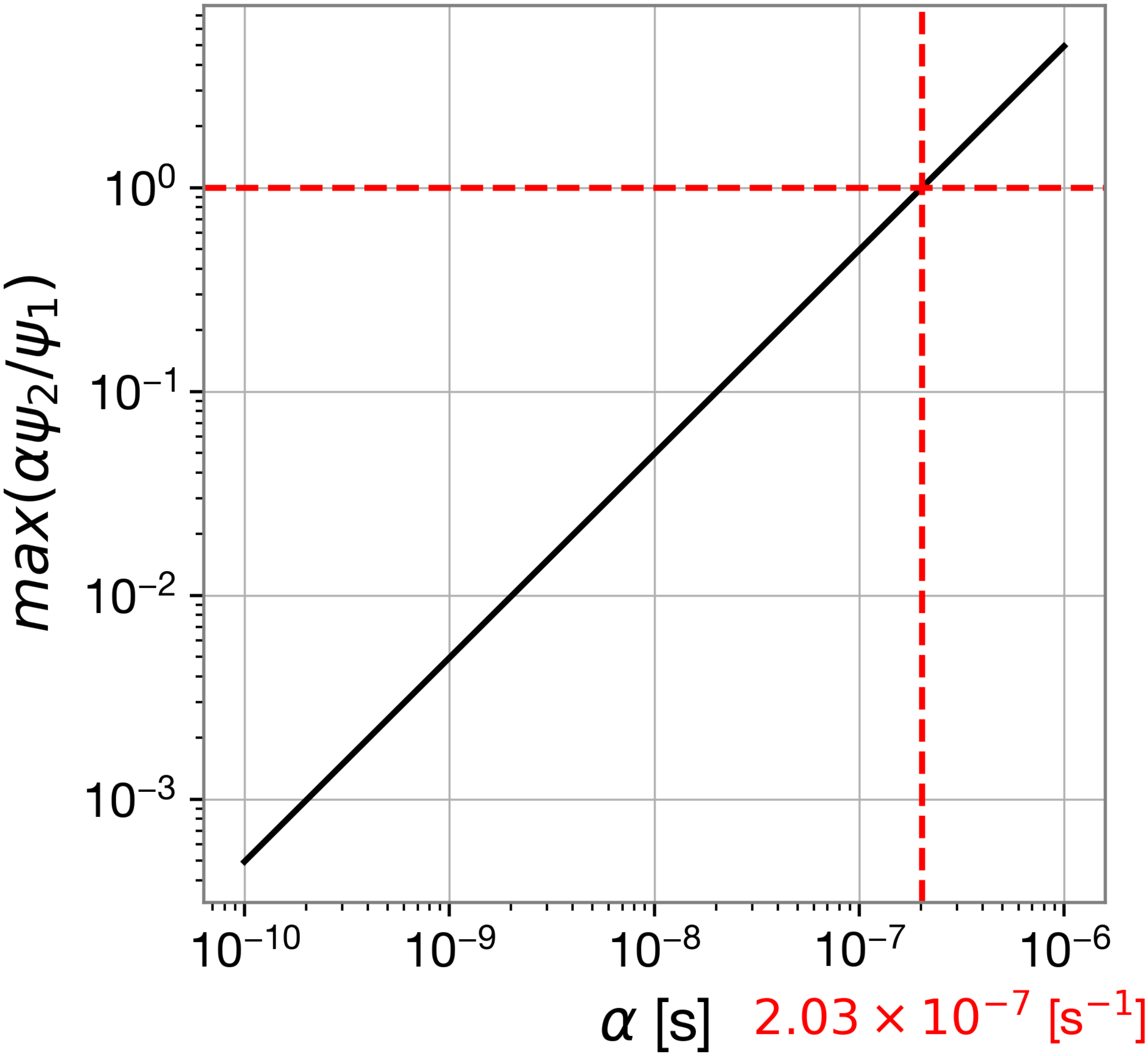

Figure 3.3: The maximum value of $\alpha\,\psi_2\,/\,\psi_1$, the ratio $\alpha^2\,\psi_2$ to $\alpha\,\psi_1$ as a function of α for fixed $\mathcal{M} = \mathcal{M}_{\mathrm{bNS}}/2$. By comparing the $O\,(\alpha^2)$ and $O\,(\alpha)$ corrections to our model, we see that the quadratic correction is much less than, and therefore negligible to, the linear correction as long as $\alpha \ll 10^{-7}\ \mathrm{s}^{-1}$. Once $\alpha \sim O\,(10^{-7}\ \mathrm{s}^{-1})$, then $\alpha^2\,\psi_2$ is within an order of magnitude of $\alpha\,\psi_1$ until they become equal at $\alpha \approx 2.03 \times 10^{-7}\ \mathrm{s}^{-1}$. Therefore, we set this value of α as the absolute maximum limit of α for which our model can be valid, this is marked in Fig. 3.2 by the gray regions.

3.8 Inferred Masses Deviate from True Values if Acceleration is Present but Unmodeled

In this Section, we present an injection analysis that demonstrates how binary parameters can be biased if a non-accelerating model is used for parameter inference of an event with true $\alpha_{\rm tr} \neq 0$. In particular, we injected our template (cf. Eq. (3.4)) with various values of the CoM acceleration, fixed component masses $m_1 = m_2 = 1.4\,M_\odot$, and fixed aligned spin components $\chi_{1,z} = \chi_{2,z} = 0$, into mock noise for a detector with the projected ET-D PSD (cf. Fig. 3.1). We then apply the relative binning method for fast likelihood evaluation [206] and our model with α set to 0 to infer the chirp mass, symmetric mass ratio, and component spins. We derive posterior probability distributions with the nested sampling Monte Carlo algorithm MLFriends ([40, 41]) using the UltraNest[1] package [42].

A corner plot [79] of our analysis is shown in Figure 3.4. Curves of various colors correspond to different injected values of $\alpha_{\rm tr}$, $\alpha_{\rm tr} = 0$ s^{-1} (blue), 10^{-12} s^{-1} (orange), 10^{-10} s^{-1} (green), 10^{-8} s^{-1} (red). The true values of the other parameters are marked by the solid black lines. Each posterior distribution is derived by fixing $\alpha = 0$ s^{-1} in our fitting model and using uniform priors for all parameters. We see that both the inferred chirp mass and symmetric mass ratio deviate by significantly more than 1σ for CoM acceleration as large as $\alpha \gtrsim 10^{-8}$ s^{-1}. For smaller values of $\alpha_{\rm tr}$, the inferred parameters are consistent with their true values.

This brief analysis demonstrates that neglecting CoM acceleration can bias the inferred binary parameters for $\alpha_{\rm tr}$ as large as 10^{-8} s^{-1}. It is unlikely that neglecting CoM acceleration will qualitatively change the interpretation of the GW signal because the chirp mass is biased by about one part in a hundred thousand and the symmetric mas ratio is biased by a few parts in ten thousand.

[1] `https://johannesbuchner.github.io/UltraNest/`

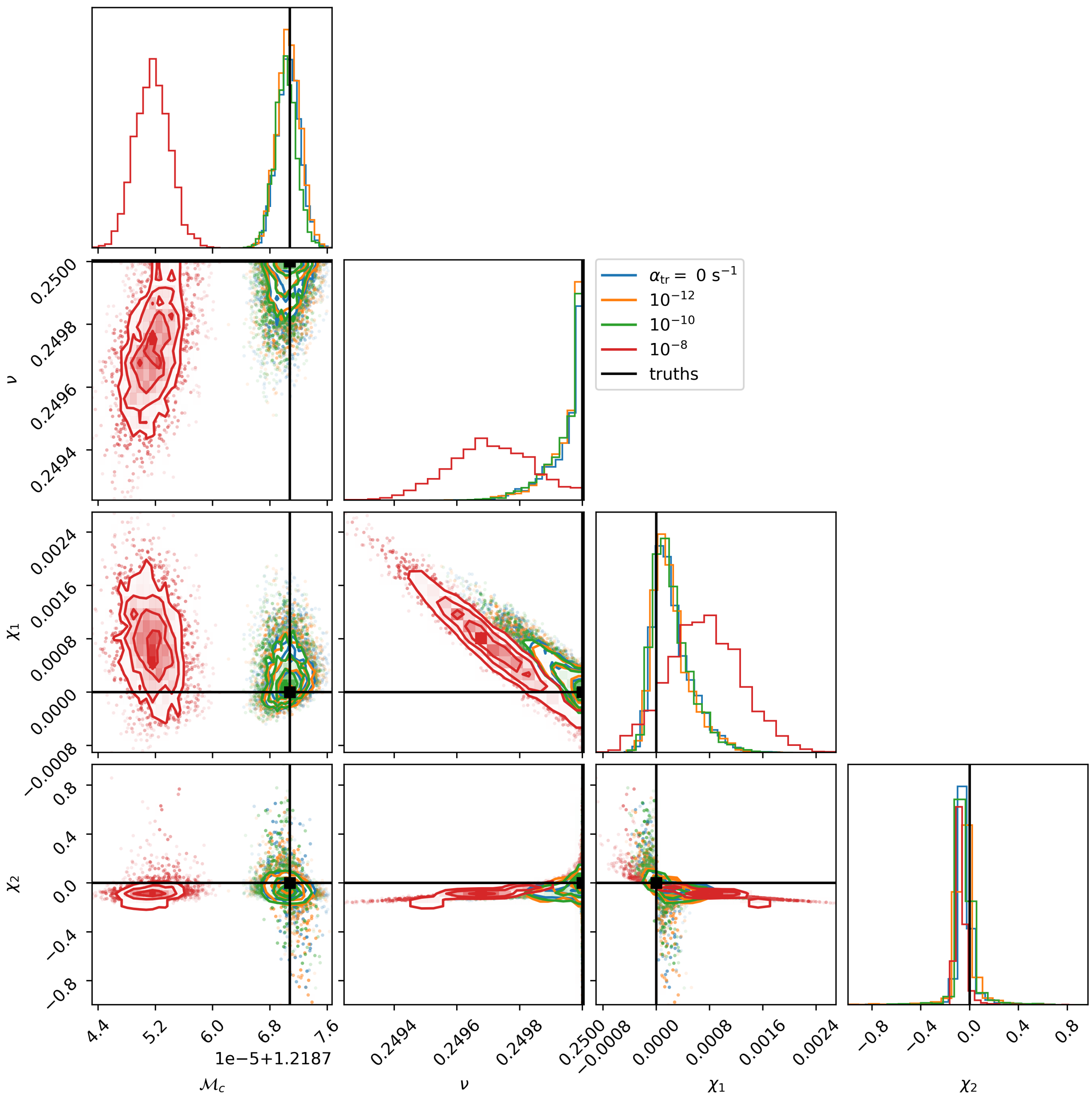

Figure 3.4: Posterior distributions of binary parameters when TaylorF2 (cf. Eq. (3.4)) with $\alpha = 0$ is used to analyze a signal with true $\alpha_{tr} \neq 0$ given by the colors ($\alpha_{tr} = 0$ s^{-1} (blue), 10^{-12} s^{-1} (orange), 10^{-10} s^{-1} (green), 10^{-8} s^{-1} (red)) and the black solid lines denoting the parameters' true values. We see that for $\alpha \gtrsim 10^{-8}$ s^{-1}, the chirp mass can deviate by significantly more than 1σ, while ν deviates moderately from its true value. While the posterior distributions for the aligned spin components are centered at slightly nonzero values, they are still consistent with zero.

Chapter 4

Double White Dwarf Tides from Multi-messenger Measurements

4.1 Introduction

Short-period double white dwarf (DWD) systems in the Milky Way are one of the loudest predicted populations and the only observationally-guaranteed population of gravitational wave (GW) sources at low frequencies 10^{-4}–10^{-2} Hz detectable by space-based interferometric observatories such as a forthcoming leading mission LISA [18] (see also the TianQin mission [123]). Along with GW signals from super-massive black hole binaries (SMBHBs) and extreme mass ratio inspirals (EMRIs), GW signals from DWDs are expected to be persistent and overlapping in both time and frequency, unlike the short events measured by the LIGO-Virgo-KAGRA (LVK) collaboration. The loudest of these signals are individually detectable in GWs and can be fit and removed from the data. Those include the DWDs [119, 110, 111, 45] that have already been observed electromagnetically, which will enable complementary constraints on their binary orbital motions. A much larger number of these signals will be unresolvable and they will form a stochastic GW background in the frequency range 10^{-4}–10^{-3} Hz [61, 102]. This confusion noise, in the particular case of a nominal four-year LISA mission and after subtraction of individually detectable signals, is predicted to be the dominant contribution to the strain power spectral density in the frequency range $0.5 - 2\,\mathrm{mHz}$ [102, 107, 22].

It has been estimated that in the Milky Way tens of millions of DWD systems exist across the LISA frequency band [106], but only $\mathcal{O}(10^2)$ LISA-band DWDs have been detected in the optical domain as short-period eclipsing binaries [111, 170, 47, 46, 159].

So far, optical detections are made through major spectroscopic and photometric monitoring programs such as the Extremely Low Mass (ELM) survey [39] and the Zwicky Transient Facility (ZTF) [30]. The Gaia mission has provided astrometry, allowing us to compute distances to sources, and will likely enable more detections when photometry is released [110, 111]. Over the next decade, substantially more short-period DWDs are expected to be detected first electromagnetically at the Vera C. Rubin Observatory (also known as LSST), which we consider in this work, and then with gravitational waves LISA. Measurements of both magnitude and GW strain as a function of time from the same DWD source independently allow us to extract information about the orbital phase evolution, with the GW phase being always twice the orbital phase; these two different observational avenues also yield unique and complementary information about other intrinsic and extrinsic properties of the DWD system. The combination of photometric and GW signals will enhance detections of individual DWDs and lead to more precise measurements of their stellar and orbital properties [175, 174], and hence will help shed light on the formation and evolution of DWDs on tight orbits.

DWD inspiral in the LISA band is likely a later stage in the dynamic evolution of DWD systems. The progenitor stars are too big to fit into the current tight DWD orbits observed, while orbital decay via GW radiation alone is insufficient to allow initially widely separated DWDs to merge within a Hubble time [98, 145]. A promising explanation for the formation of these systems is a common-envelope (CE) phase, in which the compact cores of both progenitor stars spiral within a shared stellar envelope of hydrogen following unstable binary mass transfer [142]. Such CE dynamics leads to rapid ejection of the shared hydrogen envelope and the compact cores stall on a very tight orbit. The fraction of orbital energy dissipated in this process has been constrained by DWD population studies [170]. Alternatively, the WD binary could have been part of a hierarchical triple system, and via the Kozai-Lidov (KL) effect [108, 115, 134] it could have been driven onto a highly eccentric orbit with a large semi-major axis but a tiny periastron. With energy loss from tides and GW radiation, the binary orbit can circularize and settle down to a short period. Both formation channels are expected to produce systems of circular orbits in the LISA band. To our knowledge, eccentric systems with short periods, although expected from dynamic formation channel in dense stellar systems [196], are yet to be found.

Short-period DWDs are further tightening their binary orbits through GW radiation. When these systems reach a critical orbital period of roughly $P_c \approx 45\text{–}130\,\mathrm{min}$ (depending on the exact WD masses and ages) [80, 47], tidal torquing turns on to drive the WDs toward tidal locking, for which the WD spin periods are synchronized with the binary orbital period. Since WD spins open up an additional angular momentum reservoir, such tidal interaction modifies the rate of orbital tightening, and hence the orbital phase evolution measurable with both photometry and GWs. When the DWD orbit becomes sufficiently tight, one WD will overflow its Roche lobe and begin to transfer mass to the other, which further impacts the orbital evolution. This mass transfer can eventually cause the accreting object to trigger a Type Ia supernova (SN), which are used as a standard candle for measuring the expansion rate of the Universe [144, 57]. The mechanisms through which this can happen are still being studied. Recently, the dynamically-driven double-degenerate double-detonation (D^6) scenario has been used to explain the existence of high speed white dwarfs in Gaia data by proposing they are the companions of the exploding star in the scenario [177, 28].

It is easier to isolate the effects of the tides on the orbital evolution prior to the onset of Roche-lobe overflow, so in this work we shall consider detached DWDs, which should also be more common than mass-transfer systems due to longer orbital evolution timescales. By analyzing tidal effects on the orbital decay rate, we can constrain the combined moment of inertia of the two WDs, which will allow for novel constraints on WD structure and internal physics [47]. In addition, tidal effects before Roche-lobe overflow set crucial initial conditions for WD mergers [81].

In this chapter, we turn specific attention to the degeneracy that rises between the dependence of orbital phase evolution on the tides and that on the WD masses. Some previous works assumed a value for the tidal contribution to orbital decay, but they are unable to measure it independently of the contribution from GW radiation [46, 47]. In Section 4.2, we will present a framework to quantify the effect of tides on DWD orbital evolution for detached, tidally locked DWD systems. In Section 4.3, we will discuss parameter degeneracies that arise from including these effects and how these degeneracies may be broken using multi-messenger information. In Section 4.4, we describe mock multi-messenger parameter inference we perform to test the feasibility of the methods of breaking the degeneracies. In section 4.5, we present the results of our mock parameter inference study, and in Section 4.6, we discuss the implications of these results. We give concluding remarks in 4.7.

4.2 Tidal Effects in Detached, Tidally-Locked DWDs

The orbital frequencies of LISA-band DWDs increase over time mainly due to GW radiation. However, this orbital evolution is expected to be slow ($f_{GW} = 3 \times 10^{-4}$–$10^{-2}$ Hz and $\dot{f}_{GW} = 10^{-18}$–10^{-15} Hz s^{-1}) [106]. The timescale for order-unity change in the orbital frequency is much longer than the expected time span of photometric surveys and GW observations. Therefore, we model the orbital phase evolution using the following low-order polynomial,

$$\phi_{orb}(t) = \phi_0 + 2\pi \left(f\, t + \frac{1}{2}\, \dot{f}\, t^2 + \frac{1}{6}\, \ddot{f}\, t^3 \right), \tag{4.1}$$

where f, $\dot{f}$ and $\ddot{f}$ are phase derivatives defined at a chosen reference time. For circular inspiral, each orbital cycle corresponds to two sinusoidal GW cycles, and the GW phase is twice the orbital phase as parameterized in Eq. (4.1). The quadrupole formula predicts that due to GW radiation alone the orbital evolution depends on the chirp mass of the binary, $\mathcal{M} = (M_1\, M_2)^{3/5}/(M_1 + M_2)^{1/5}$ (where M_1 and M_2 are the masses of the binary components) [145]:

$$2\dot{f}_{\mathrm{GW}\,only} = \frac{96}{5}\, \pi^{\frac{8}{3}} \left(\frac{G\mathcal{M}}{c^3} \right)^{\frac{5}{3}} (2\, f)^{\frac{11}{3}}, \tag{4.2a}$$

$$2\ddot{f}_{\mathrm{GW}\,only} = \frac{33792}{25}\, \pi^{\frac{16}{3}} \left(\frac{G\mathcal{M}}{c^3} \right)^{\frac{10}{3}} (2\, f)^{\frac{19}{3}}. \tag{4.2b}$$

As previously mentioned, tidal effects will correct these frequency derivatives, which is more significant at short orbital periods. For DWDs that are undergoing tidal spin-up (or spin-down) but are not yet synchronized, one can parameterize the degree of tidal locking using a phenomenological tidal locking factor $\eta = \Omega_{spin}/\Omega_{orbit}$ as introduced in [147]. This approach uses the simplifying assumption that both stars are spinning at the same orbital frequency Ω_{spin}. When the period of a DWD system drops below the critical orbital period $P_c \approx$ 45–130 minutes, η asymptotes towards 1 (complete tidal locking) as shown in Figure 12 of [80]. As the system reaches short periods, η changes more slowly such that $\dot{\eta}/\eta \ll \dot{f}/f$. Because of this, we will allow a general value of η, but we will use the simplifying assumption that η is a constant in time.

Assuming complete tidal spin-orbit synchronization, we can derive tidal corrections to the frequency derivatives. The binding energy of the binary is the sum of gravitational potential energy E_g and kinetic energy of the binary orbital motion $E_{k,orb}$:

$$E_{\rm orb} = E_g + E_{k,orb} = -\frac{G\,M_1\,M_2}{2\,a}, \tag{4.3}$$

where a is the binary semi-major axis. Applying Kepler's 3rd Law, the rate of change in E_{orb} is proportional to the orbital period derivative

$$\dot{E}_{\rm orb} = \frac{GM_1M_2}{3\,a}\,\frac{\dot{P}}{P}. \tag{4.4}$$

If the finite sizes of the WDs are neglected, this energy would be lost only to GW radiation. When the finite sizes are accounted for, orbital energy partially converts into WD rotation energy, and is partially lost to tidal heating, in addition to GW loss. When tidal-locking is achieved, the tidal heating rate is very low [80], so we neglect this contribution and write

$$\dot{E}_{\rm orb} = \dot{E}_{k,\rm rot} + \dot{E}_{\rm GW}. \tag{4.5}$$

Assuming the stars rotate at the same rate parameterized by the constant $\eta = \Omega_{spin}/\Omega_{orbit}$, the rotational kinetic energy of the WDs change at a rate

$$\dot{E}_{k,\rm rot} = -4\pi^2\,I\,\frac{\dot{P}}{P^3}\,\eta^{-2}, \tag{4.6}$$

where $I = I_1 + I_2$ is the sum of moments of inertia of the two WDs.

Now we can use these expressions to calculate the orbital frequency derivative in terms of the power transferred into the GWs:

$$\frac{\dot{f}}{f} = -\frac{\dot{P}}{P} = \frac{3\,a}{G\,M_1\,M_2}\,\frac{\dot{E}_{\rm GW}}{1-r}, \tag{4.7}$$

where r is the absolute value of the ratio of Eq.(4.6) and Eq.(4.4) and is given by

$$r \equiv \frac{12\pi^2\,I\,a}{G\,M_1\,M_2\,P^2\eta^2}. \tag{4.8}$$

The period derivative without tidal effects is recovered if I or r are set to zero. we can write the orbital frequency derivative as

$$\frac{\dot{f}}{f} = \frac{\dot{P}}{P} = \frac{\dot{f}_{\mathrm{GW}\,only}}{f}\left(1 + \frac{r}{1-r}\right). \tag{4.9}$$

To determine the second frequency derivative $\ddot{f}$, we need to know $\dot{r}$. Applying Kepler's 3rd law to relate a and P, we have $r \propto P^{-4/3} \propto f^{4/3}$. Here we are assuming for simplicity that $\dot{\eta} = 0$. We derive

$$\frac{\dot{r}}{r} = \frac{4}{3}\frac{\dot{f}}{f} = \frac{4}{3}\frac{\dot{f}_{\mathrm{GW}\,only}}{f}\left(1 + \frac{r}{1-r}\right). \tag{4.10}$$

We simplifying our final expressions by replacing r with a different dimensionless ratio $r_{\mathrm{t}ide}$, which is defined as

$$r_{\mathrm{t}ide} \equiv \frac{\dot{P}_{\mathrm{t}ide}}{\dot{P}_{\mathrm{GW}}} = \frac{r}{1-r}. \tag{4.11}$$

The first frequency derivative can be written as

$$\dot{f} = \dot{f}_{\mathrm{GW}\,only}\,(1 + r_{\mathrm{t}ide}) \tag{4.12}$$

The second frequency derivative is then derived by taking the time derivative of Eq.(4.10), using $\dot{f}_{\mathrm{GW}\,only} \propto f^{11/3}$, and applying Eq.(4.10)

$$\ddot{f} = \frac{(\dot{f}_{\mathrm{GW}\,only})^2}{3\,f}\,(1 + r_{\mathrm{t}ide})^2\,(11 + 4\,r_{\mathrm{t}ide})\,. \tag{4.13}$$

4.3 Resolving Degeneracy Between Chirp Mass and Tides

In previous analyses of photometrically monitored DWD systems, mass measurements are carried out by constraining the time derivative of the orbital frequency [46, 47]. With only the first frequency derivative $\dot{f}$ measured, there is a degeneracy between $\mathcal{M}$ and r_{tide} for tidally locked DWDs. If the second frequency derivative $\ddot{f}$ is measurable, this degeneracy can be lifted. Unfortunately, for typical short-period detached DWDs $\ddot{f}$ is extremely small $\ddot{f}_{GW} \lesssim 10^{-28}\,\mathrm{s}^{-3}$. Eq. (4.2a) and Eq. (4.13) imply a steep scaling $\ddot{f} \propto f^{19/3}$, so the best hope for measuring $\ddot{f}$ would lie in those detached DWDs with the shortest periods ($P \lesssim 10\,\mathrm{min}$). As we will show, even those will require very long time baseline and high precision of phase measurement, which would require extremely dedicated photometric monitoring.

Additional information could be exploited to break the degeneracy between $\mathcal{M}$ and $r_{\mathrm{t}ide}$. Radial velocity measurements from spectroscopy can be used to independently constrain orbital velocities and thus disentangle parameter degeneracy between orbital period, orbital separation, and masses. Getting radial velocity measurements from both stars requires the stars to be extraordinarily close in temperature so that both lines are detectable. This requires extremely tight fine tuning of star temperatures, and is usually impossible. Single radial velocity measurements using the 10m Keck telescope were used to analyze bright ZTF sources in [45], but the information was not sufficient to break this degeneracy. This degeneracy could be broken with higher precision single radial velocity measurements, but this would require a substantial amount of dedicated time on an extremely large telescope, which is often cost prohibitive.

Alternatively, a coherent GW signal detected will provide this information. At a given orbital frequency f, the observed strain amplitude depends on the chirp mass $\mathcal{M}$, the luminosity distance to the source d_L, and the orbital inclination ι, but is not affected by tidal interaction. For eclipsing DWDs, ι will be well determined. The luminosity distance d_L can be extracted from the photometric magnitudes of the binary if temperature and radii are independently constrained by data. For an eclipsing DWD system, surface temperatures can be measured with multi-band photometry and the radii of the WDs can be measured from the eclipse signals.

In this work, we would like to compare two methods to break the degeneracy between $\mathcal{M}$ and r_{tide}: one approach by directly measuring $\ddot{f}$ and the other multi-messenger approach by combining photometric and GW signals. Many eclipsing DWDs are or will be initially discovered in large-sky-coverage photometric cadence surveys, and for this reason, we consider the Vera C. Rubin Observatory (also known as LSST), a six-band flagship program which will survey roughly half of the sky over a decade [17]. By the time LISA is operational, this 10-year survey will have been carried out, and many eclipsing DWDs individually detectable with LISA will have their optical counterparts identified in LSST. However, LSST will have a 30-second exposure time for each image, which can partially smear out the eclipsing signal, whose duration can be as short as a few minutes. To explore the best chance at detecting $\ddot{f}$ with a good precision, we also consider HiPERCAM, an existing short-cadence camera that has been deployed on the 10.4-m Gran Telescopio Canarias (GTC) [70]. In order to balance readout noise and shot noise, we assume 3 second visits as was done for HiPERCAM in [45].

4.4 Mock Parameter Inference

To investigate how effective the multimessenger approach and photometric $\ddot{f}$ measurements with HiPERCAM are for breaking the $\mathcal{M}$–r_{tide} degeneracy, we generate mock photometric and GW data with injected DWD signals, and perform mock Bayesian parameter estimation to derive posterior distributions for the source parameters. In this section, we will explain how we generate mock data for LISA, LSST, and HiPERCAM, respectively.

4.4.1 LISA

LISA will consist of three spacecrafts in triangular formation that orbit the sun in a cartwheeling heliocentric orbit that trails the Earth by about 20 degrees [18]. Each spacecraft is equipped with two lasers that can beam signals to each of the other two spacecrafts. Each spacecraft is also equipped with detection systems that can measure the phases of the incoming laser signals from the other two spacecrafts. There are a total of six time series that result from measuring the residual phase of each laser signal between emission and detection.

With onboard instrumentation accounting for most of the noise sources, the dominant noise source is laser frequency noise, which is different for each of the six lasers. This laser frequency noise can be canceled by using linear combinations of these time series, each delayed by different amounts. This process, called Time Delay Interferometry (TDI) [188], gives us 3 time series that minimize noise, called $X(t)$, $Y(t)$, and $Z(t)$, which cyclically transform into each other under cyclic permutation of the satellites.

These three time series have correlated noises. The noises can be made uncorrelated by diagonalizing the covariance matrix and finding the eigenvectors that describe linear combinations of $X(t)$, $Y(t)$ and $Z(t)$. These linear combinations, $E(t)$, $A(t)$ and $T(t)$, are given by

$$E = (X - 2Y + Z)/\sqrt{6}, \tag{4.14a}$$

$$A = (Z - X)/\sqrt{2}, \tag{4.14b}$$

$$T = (X + Y + Z)/\sqrt{3}. \tag{4.14c}$$

Due to full symmetry in this definition, no astrophysical source will produce signals in the T channel. The time-domain expressions we use for X, Y, and Z are detailed in Section 8.3 of [23]. We use Solar System Barycenter (SSB) conventions from Section 6.1, spacecraft orbits from Section 8.1, and a cubic polynomial for the phase that is twice of Equation 4.1. We assume that the three channels have stationary Gaussian noise described by power spectral densities (PSDs) $S_E(f) = S_A(f)$ and $S_T(f)$ as defined in Section 8.3, with further optical metrology and acceleration noise estimates defined in [22].

The assumption of stationary Gaussian random noise is an ideal one. The assumption of stationarity may not be accurate for several reasons; for example, the rotation of the LISA constellation plane relative to the Galactic plane, from which the bulk of the Galactic DWD confusion noise originates, will cause temporal variations in the total noise power spectra [71]. We also assume that the PSDs are known to infinite precision, while a more accurate likelihood model would marginalize over PSD uncertainties [32]. However, we lack further detailed information to account for these complications as neither real LISA data nor extensive survey data on the bulk of the Galactic DWD population is available. Additionally, as LISA will not launch for at least another decade, our PSD estimates are based on design specifications to be realized, so for this work, we will settle for stationary Gaussian noises with PSDs taken from the LISA design specifications as provided in [22].

With the assumption of stationary noise, we would need to evaluate LISA waveforms in the frequency domain for DWDs. To allow efficient computation, we use a heterodyned frequency domain waveform similar to that described in Appendix A of [63]. Essentially, we divide the complex-valued frequency-domain signal by a monochromatic complex exponential factor with the frequency of the GW at the reference time which yields a term that varies slowly and smoothly with the frequency and contains information about frequency derivatives induced by both the intrinsic source chirping and the Doppler effect caused by the motion of the LISA constellation. This slowly varying piece can be well approximated through a computationally-efficient FFT performed on a coarse frequency grid.

To generate mock data, we assume that LISA begins to record data on January 1st, 2037 at midnight and runs for exactly 4 years at a sampling rate of 0.1 Hz.

4.4.2 Lightcurve Model

For this work, we employ a simple photometric lightcurve model for eclipsing DWDs, which accounts for all of the important effects. We will apply this model to both LSST and HiPERCAM, except that the photometric noise level and cadence are telescope-specific, and are specified in Sections 4.4.3 and 4.4.4. We model four effects on the lightcurves: the spectral energy distribution for single WDs (excluding the radiation effect from the companion star), eclipses, ellipsoidal variation due to tidal deformation of the stars, and irradiation of each star by the other. For simplicity, these effects are treated as additive in the photometry.

First, we need to calculate the flux of a WD star in any given photometric filter without corrections due to the companion star. For this, we compute the fractional frequency-averaged spectral flux density f_b for each band under the assumption that each WD has a blackbody spectrum [105]. We assume an ideal filter throughput curve as defined by perfect transmission between a pair of cutoff wavelengths in Table 2.1 of [17]. Details such as atmospheric absorption, imperfect reflectivity/transmission for various optical components, and sensor efficiency create a more complicated transmission function that is projected to range roughly from 30-70%, but we ignore this for simplicity. We use the same cutoffs for both LSST and HiPERCAM. We define $f_b(T)$ to be the fractional frequency-averaged spectral flux density in the given photometric filter b for a WD of a surface temperature T, which we can calculate as

$$f_b(T) = \frac{15\, h^3\, c^3}{\pi^4\, (k_B\, T)^4} \frac{\int_{\lambda_{\min,b}}^{\lambda_{\max,b}} \frac{\lambda^{-4}}{\exp(hc/\lambda\, k_B T)-1}\, \mathrm{d}\lambda}{\int_{\lambda_{\min,b}}^{\lambda_{\max,b}} \mathrm{d}\lambda/\lambda}. \tag{4.15}$$

The total flux of star i in band b is given by this multiplied by the total flux:

$$\Phi_{i,b} = \frac{\sigma\, T_i^4\, R_i^2}{d_L^2} f_b(T), \tag{4.16}$$

where T_i and R_i are the surface temperature and radius of star i, d_L is the luminosity distance to the star and σ is the Stefan-Boltzmann constant.

Eclipses create two unequal dips corresponding to two transits per orbit: the primary eclipsing the secondary and vice versa. To model these dips, we borrow a simple analytic result derived for planet transits in Section 3B of [161] to model flux reduction during WD transits. To compute the linear and quadratic limb-darkening coefficients, we interpolate the data in “tableab” associated with [60], using the DB atmosphere for each of the u, g, r, i, z and y SDSS bands, which correspond reasonably well to the target LSST bands. Finally, we assume zero eccentricity and compute the eclipse durations (measured in units of the orbital phase) for given stellar radii and binary orbital inclination. These first two effects alone produce the following band-dependent lightcurve as a function of phase:

$$L_{ecl}(\phi) = \frac{\sigma\, T_1^4\, R_1^2}{d_L^2}\, f_b(T_1)\, \left(1 - S_1(\phi)\right) + \frac{\sigma\, T_2^4\, R_2^2}{d_L^2}\, f_b(T_2)\, \left(1 - S_2(\phi)\right), \tag{4.17}$$

where S_i is the fractional loss in flux for the star i eclipsed by the other star. At phase $\phi = 0$, star 1 eclipses star 2 and S_2 reaches its peak value. At phase $\phi = \pi$, star 2 eclipses star 1 and S_1 reaches its peak value.

Next, we consider tidal deformation of the stellar shape. This causes the otherwise circular photosphere to apppear to the observer as an ellipse whose shape varies with the orbital phase. Such ellipsoidal variation induced by tides is often modeled directly as a sinusoid with an amplitude that depends on orbital inclination, stellar radii, binary mass ratio, as well as limb darkening and gravity darkening coefficients [132, 94, 107]. This approximation has been shown to be inconsistent with radial velocity and measured Doppler beaming effects in calculating the binary mass ratio $q = M_2/M_1$ in the analysis of KOI-74 from Kepler data [34]. This expression has differing values for each star and there is also band dependence in the limb darkening and gravity darkening effects. To absorb the above modeling complication, we opt to introduce a phenomenological dummy mass ratio parameter q_{dummy} in place of the physical mass ratio q but still use this common expression. Adding this effect, the lightcurve becomes

$$\begin{aligned} L_{\mathrm{ecl,ell}}(\phi) =& \frac{\sigma\, T_1^4\, R_1^2}{d_L^2}\, f_b(T_1)\, (1 - S_1(\phi))\, (1 - \ell_{1,b}\, \cos(2\phi)) \\ &+ \frac{\sigma\, T_2^4\, R_2^2}{d_L^2}\, f_b(T_2)\, (1 - S_2(\phi))\, (1 - \ell_{2,b}\, \cos(2\phi)), \end{aligned} \tag{4.18}$$

where $\ell_{i,b}$ is given by

$$\ell_{i,b} = \frac{3\,(15 + u_{i,b})(\tau_{i,b} + 1)}{20\,(3 - u_{i,b})} \left(\frac{R_i}{a}\right)^3 q_{\mathrm{dummy}}\, \sin^2 \iota. \tag{4.19}$$

In the above expression, a is the binary semi-major axis, ι is the orbital inclination, and $u_{i,b}$ and $\tau_{i,b}$ are the linear limb darkening parameter and gravity darkening parameter, respectively, for star i and photometric band b. We use the same linear limb darkening parameters as used in the transit expressions, and we calculate the gravity darkening coefficients using Equation 10 of [60], using $\beta = 0.25$ and the center of each photemetric band as the observed wavelength.

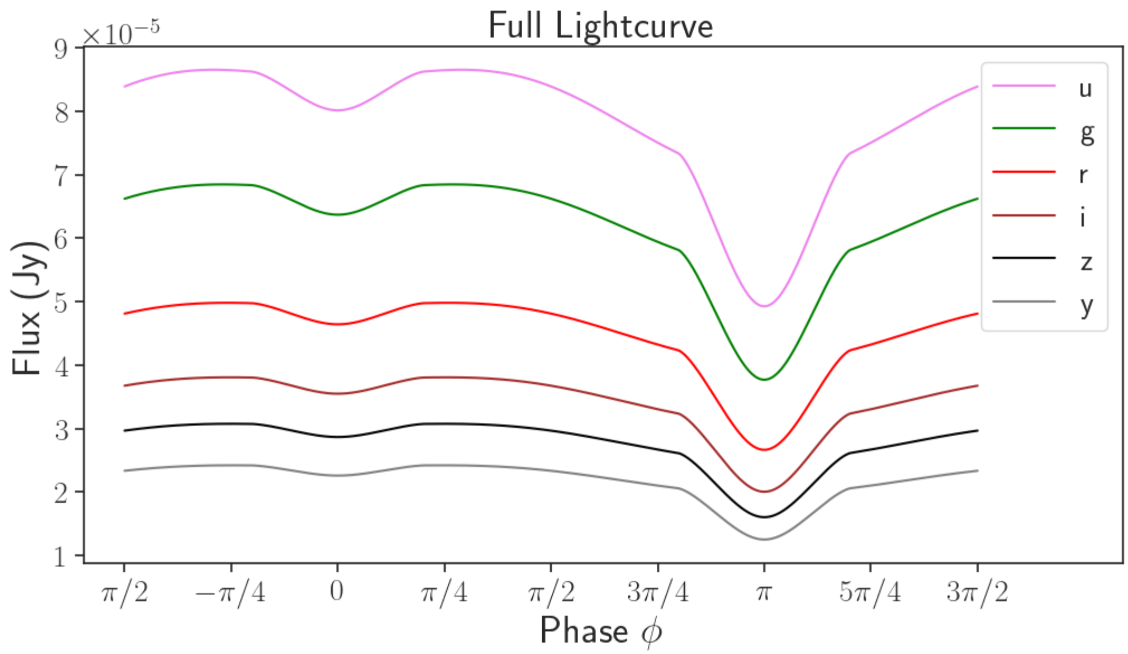

Figure 4.1: Phase-folded model lightcurves from Equation 4.20 using the parameters in Table 4.1 across the 6 photometric bands used by LSST. The effects of eclipsing and irradiance are clearly visible, but the effect of the ellipsoidal variation (which has 2 periods in one orbit) is difficult to discern as its amplitude is small ($\ell_{i,b} \sim 0.03 - 0.04$).

Finally, the photometric effect of WDs irradiating each other needs to be accounted for. Strictly speaking, this effect is not independent of the other effects we have considered as it creates temperature variation on the WD surface. Codes such as `ellc` have been developed to precisely calculate the full effect of this [128]. Crudely speaking, this effect ends up looking very similar to a sinusoid with the same period as the orbit [47]. In order to simply account for the degeneracy that this effect has with the others, we use this approximation with a simple phenomenological amplitude $A_{\rm irr}$ to complete our simple lightcurve model:

$$L_{\rm full}(\phi) = \Bigg[\frac{\sigma\, T_1^4\, R_1^2}{d_L^2}\, f_b(T_1)\,(1 - S_1(\phi))\,(1 - \ell_{1,b}\,\cos(2\phi)) + \frac{\sigma\, T_2^4\, R_2^2}{d_L^2}\, f_b(T_2)\,(1 - S_2(\phi))\,(1 - \ell_{2,b}\,\cos(2\phi))\Bigg] \times (1 + A_{irr}\,\cos(\phi))\,. \tag{4.20}$$

Full phase-folded lightcurves using this simple lightcurve model are shown in Figure 4.1.

4.4.3 LSST

The Vera C. Rubin Observatory (also known as LSST) hosts a 8.4-meter (effectively 6.5-meter) telescope which aims to survey roughly half of the sky in six broad photometric bands over a decade [17]. By the time LISA is launched, this 10-year survey will have been completed, and many LISA GW signals from DWDs will have optical counterparts detected with LSST. We consider a cadence for LSST that is based on the `rubin_sim` code [203] which contains a scheduler that simulates sequential decisions of which filter to use and which direction to point for the duration of LSST's operation [133]. The scheduler also determines the 5σ magnitude limit m_5 for each visit, which we use for including the photometric noise in mock LSST lightcurves. Using these values of m_5, the noise is modeled following Section 3.5 of [17], using in-text or table values for σ_{sys} and γ. We arbitrarily select the LSST-surveyed point (RA, DEC) = $(0, -20^{\circ})$ and we extract all of the times that this point is visited in each of the six photometric bands over a 10-year simulated survey at the expected LSST cadence. Each visit has a 30-second exposure, so our lightcurve model is time-averaged over 10 equally spaced points (each separated by 3 seconds) to account for smearing of the light variablity due to finite exposure times. If we simply compared an analysis including LSST to one including both LISA and LSST, the latter would have a longer baseline, which would not reflect true multimessenger advantages. In order to use comparable baselines for the comparison, we augment the LSST cadence with a four year chunk of the original 10 inserted while LISA flies. Whether or not LSST or other future surveys concurrent with LISA will be running, we want to make a conservative comparison as to not overstate the improvements from a multimessenger analysis. A mock example LSST cadence is shown in the upper panel of Figure 4.2.

4.4.4 HiPERCAM

Our mock HiPERCAM cadence begins with the first LSST measurement of the target patch of sky and consists of hour-long clusters of 3-second exposures once a year for 10 years. HiPERCAM simultaneously records data in the u, g, r, i and z photometric bands, so each 3s observation gathers 5 data points [70]. Photometric noise for HiPERCAM is modeled based on [REAL HIPERCAM DATA]. Details of this are given in Section 4.8.2 of Section 4.8. Since HiPERCAM observations are significantly shorter than the typical period of the DWDs we concern (3 s compared to 6 min), we choose not to include lightcurve time smearing. A mock example of the HiPERCAM cadence is shown in the lower panel of Figure 4.2.

4.5 Mock Parameter Inference Results

We investigate the efficacy of LISA and HiPERCAM in breaking the $\mathcal{M}/r_{\rm tide}$ degeneracy by performing injections and generate Bayesian posteriors. We do this always with mock LSST data, and with and without both LISA and HiPERCAM mock data. Our injection

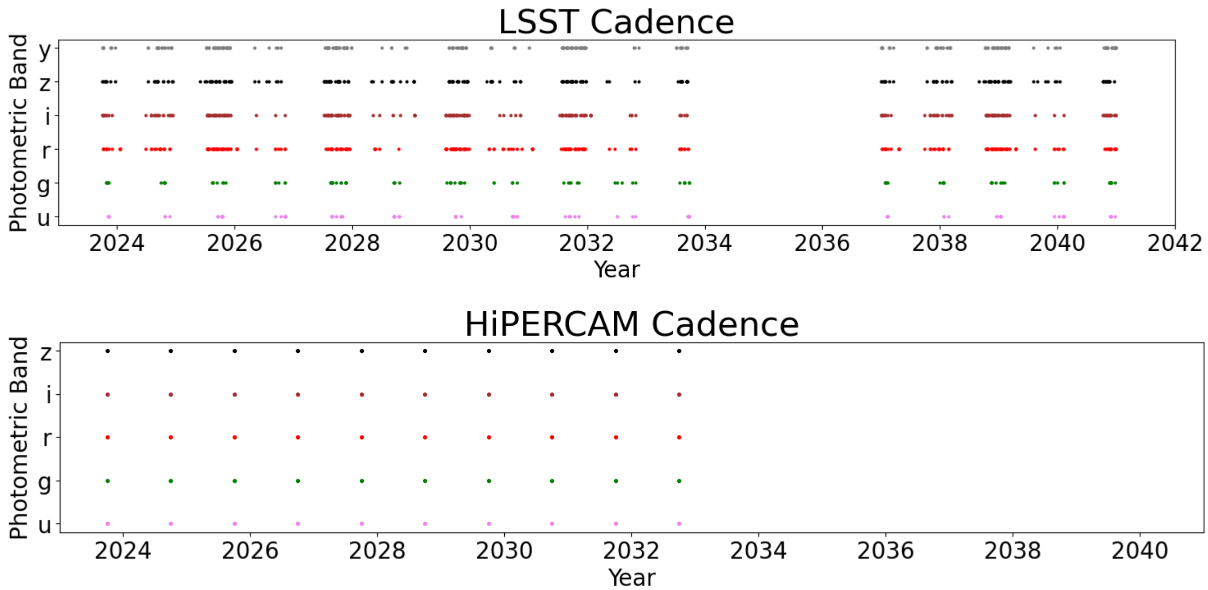

Figure 4.2: Mock cadences for the two photometric cadence surveys we consider. For LSST (upper panel), each point represents a 30 s exposure and is generated by averaging over 10 consecutive photometric measurements separated by 3 s between neighboring measurements. The total exposures in seconds are 76, 100, 294, 285, 237, and 247 in the u, g, r, i, z and y photometric bands, respectively. For HiPERCAM (lower panel), each point consists of 1200 consecutive 3-second exposures that are simultaneously taken in all six bands.

parameters are based on the source ZTF J2243+5242 identified in [46], an eclipsing DWD system with an 8.8-minute orbital period that has already been photometrically observed.

We use unpublished data from a 1.5 hour HiPERCAM observation of ZTF J2243+5242 provided by one of the authors, to choose the radii, inclination, and irradiation amplitude. The details of how we do this are in Section 4.8.1. We use the SED fit in [46], listed in their Table 3, to choose the masses, temperature, and distance. As $\ddot{f} \propto f^{19/3}$, we want to analyze a system with a very short orbital period so that it would be the most optimistic case for an attempt to directly measure $\ddot{f}$. We choose a reduced orbital period of 6 min; further decreasing it to 5 min would result in Roche-lobe overflow. We calculate r_{tide} using Equations 4.8 and 4.11, evaluating each moment of inertia as $I_i = \kappa_i M_i R_i^2$, where $\kappa_1 = \kappa_2 = 0.12$ (like in [46]) and we use $\eta = 1$, as this orbital period is substantially smaller than the critical period for tidal locking of 45–130 min. In [47], the WDs in ZTF J1539+5027 with a period of 6.91 minutes were assumed to be fully tidally locked with $\eta = 1$, so we find this to be a reasonable assumption. Finally, we choose the roll angle and initial orbital phase arbitrarily, as they only depend on orientation of the source. All of our parameter choices are listed in Table 4.1.

Table 4.1: The injection parameters used in this work, based on our inference of HiPERCAM observations of ZTF J2243+5242 and the inference in [46] with a orbital period shortened to 6 minutes. They list their measured parameters in Table 3. Parameters below the dividing line are not independent, and are calculated based on the above parameters, but provided for reference. We calculate r_{tide} using Equations 4.8 and 4.11, evaluating each moment of inertia as $I_i = \kappa_i M_i R_i^2$, where $\kappa_1 = \kappa_2 = 0.12$ (like in [46]). All priors are uniform except for masses and radii. Mass priors are uniform in chirp mass $\mathcal{M} = (M_1 M_2)^{\frac{3}{5}}/(M_1 + M_2)^{\frac{1}{5}}$ and mass ratio $q = M_2/M_1$. Radius priors are Gaussian based on [1]. The mean was the nonzero temperature prediction for the radius and the standard deviation was the difference between the zero and nonzero temperature predictions for the radius.

Parameter	Symbol	Injected Value
Orbital Period	P_{orb}	$360\,\mathrm{s}$
Primary Mass	M_1	$0.349\,M_\odot$
Secondary Mass	M_2	$0.384\,M_\odot$
Primary Radius	R_1	$0.0319\,R_\odot$
Secondary Radius	R_2	$0.0230\,R_\odot$
Primary Temperature	T_1	$22000\,\mathrm{K}$
Secondary Temperature	T_2	$16200\,\mathrm{K}$
Luminosity Distance	d_L	$2120\,\mathrm{pc}$
Inclination Angle	ι	$87.88°$
Roll Angle	ψ	0.2
Initial Phase[1]	ϕ_0	0.3
Irradiation Amplitude	A_{irr}	-0.013517
Chirp Mass	$\mathcal{M}$	$0.3186\,M_\odot$
Mass Ratio	q	1.1002
Tidal Fraction	r_{tide}	0.1288

While we always include LSST mock observations, we would like to compare the cases with or without LISA GW data, and with or without HiPERCAM, which results in a total of four parameter posterior distributions to be compared with each other. Bayesian parameter inference is carried out with the fast and embarrassingly parallel `pocoMC` sampler [101]. We sample in mostly uniform priors, including using the ($\mathcal{M}$, q) basis for masses, but we apply a conservative mass-radius relation prior based on [1]. Our prior was a Gaussian in the radius with a mean equal to the radius predicted from mass and temperature and a standard deviation equal to the difference between the mean and the the radius predicted from the same mass and zero temperature. Posterior inference for this problem was only made possible using the parameterization described in Section 4.9. All four posterior distributions are plotted in Figure 4.3 for a clear comparison.

For this mock system, it is clear from Figure 4.3 that we are unable to break the degen-

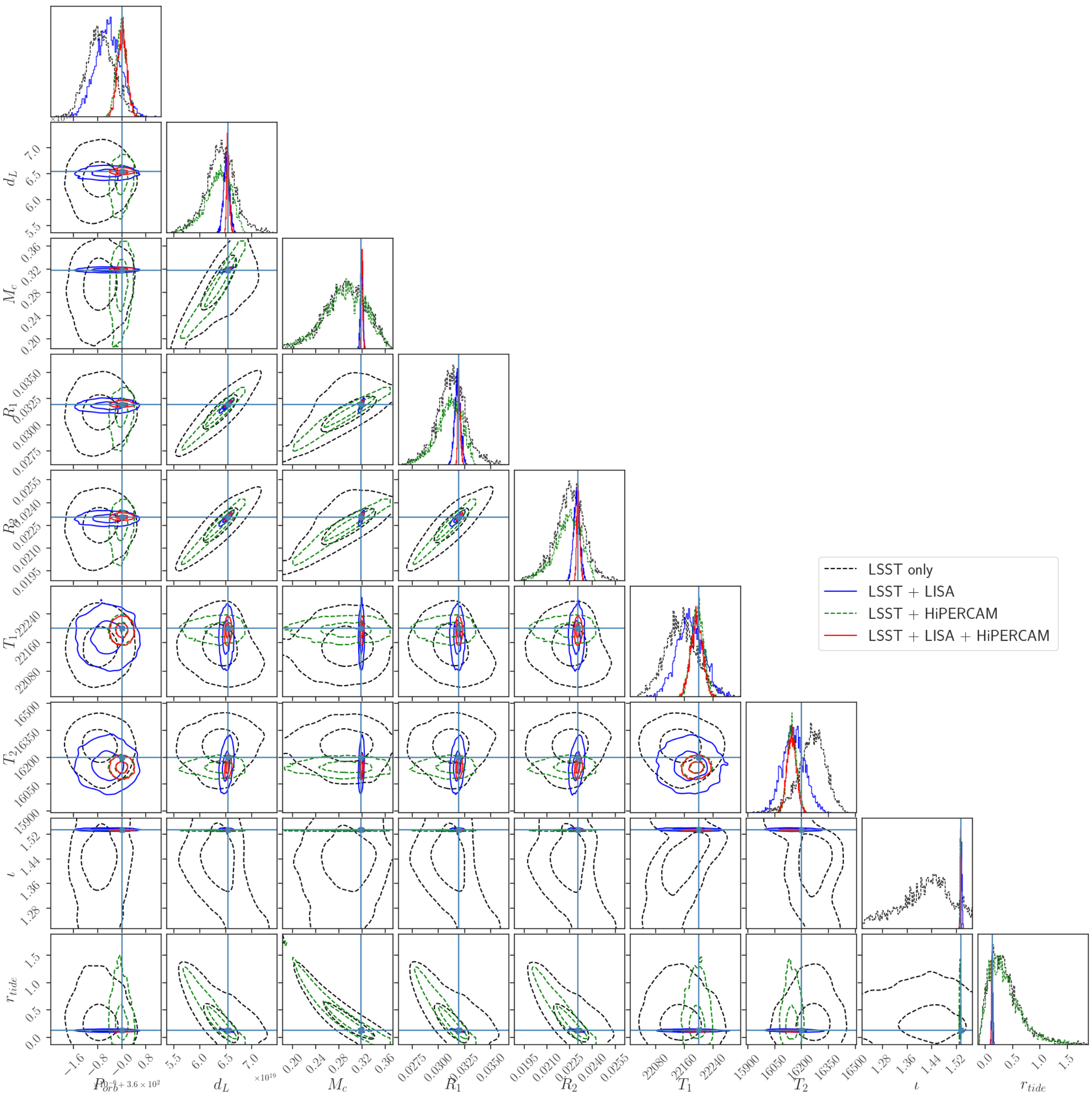

Figure 4.3: Corner plot showing parameter posteriors corresponding to all four sets of detectors/telescopes. The contours shown are for 50% and 95% credible regions. The light blue crosses are the injected values of the parameters. The posteriors including LISA are shown with solid lines and the posteriors without LISA are shown with dashed lines. The degeneracies are significantly reduced with LISA information, suggesting that $\ddot{f}$ is not constrained properly by the EM measurement of this source.

eracy between $\mathcal{M}$ and r_{tide} unless GW information is available. When LISA GW detection is available, uncertainties on $\mathcal{M}$ and r_{tide} decrease by large factors of 24 and 37 respectively when including HiPERCAM data and decrease by factors of 17 and 25 respectively with only LSST. We see significant tightening in luminosity distance and radii as well. The uncertainty in luminosity distance d_L and WD radii R_1 and R_2 all improve roughly by a factor of 9 with HiPERCAM and a factor of 5 without.

When HiPERCAM observations are available in addition to LSST observations, we see significant improvements in some of the parameters: binary period P_{orb}, surface temperatures T_1 and T_2, and inclination ι. HiPERCAM is able to achieve these improvements for 2 reasons. First, its short cadence observations which allow it to measure lightcurve details with less blurring, particularly improving the period and period derivative measurements. Second, its focused observations allow for a larger number of data points. We also note synergistic improvements with LISA as mentioned in the previous paragraph. We see even greater improvements in $\mathcal{M}$, r_{tide}, d_L, R_1 and R_2 when supplementing LISA data to LSST and HiPERCAM data than we see from simply combining LISA data and LSST data.

When LISA GW detection is added to photometric observations, we are able to empirically measure r_{tide} without making any assumptions about moment of inertia or whether tidal locking is realized. On the other hand, knowledge of both is required in order to predict a value for r_{tide}. If we assume that the mock DWD system is tidally locked, then we further need to know the combined moment of inertia $I = I_1 + I_2$ to determine r_{tide}. There exist universal relations (roughly independent of composition) for high mass, low-temperature WDs that can be used to compute the moment of inertia from mass in [199]. Our injected value of r_{tide} corresponds to nonzero temperature WDs as estimated in [46] and we measure it with sufficient precision to clearly distinguish it from the prediction of these universal relations that ignore non-zero temperature effects. The universal relations in [199] predict a value of r_{tide} that is too low to be consistent with our injections, but if we were to relax the assumption of tidal locking ($\eta = 1$), we would allow for larger values of r_{tide}. From Figure 12 of [80], we can extrapolate the values of η at a 6-min period to our WD temperatures of roughly 20,000 K to estimate $\eta \approx 0.8$. We directly compare r_{tide} predictions from the zero-temperature star model in [199] using both $\eta = 1$ and $\eta = 0.8$ with our inferred r_{tide} in Figure 4.4. In the posterior for this example DWD system, we see complete inconsistency with the fully tidally locked predictions, and reasonably strong evidence against $\eta = 0.8$. The evidence against $\eta = 0.8$ is generally stronger when HiPERCAM data is included, but for this example DWD system, this evidence is dependent on the realization of the noise. From this, we conclude that multimessenger precision on r_{tide} can be sufficient to detect and constrain, in a way independent of WD stellar structure modeling, the degree of tidal locking and/or the nonzero temperature effects on moment of inertia.

Our posteriors were generated by sampling the physical parameters of the DWD system, which do not directly demonstrate our constraints on the phenomenological parameter $\ddot{f}$. Because $\ddot{f}$ is best constrained via EM measurement with high phase precision and many visits, we can estimate $\ddot{f}$ constraints using only HiPERCAM. We estimate the constraints on $\ddot{f}$ for this 6 min ZTF J2243+5242 source for varying lengths of observation times, frequencies

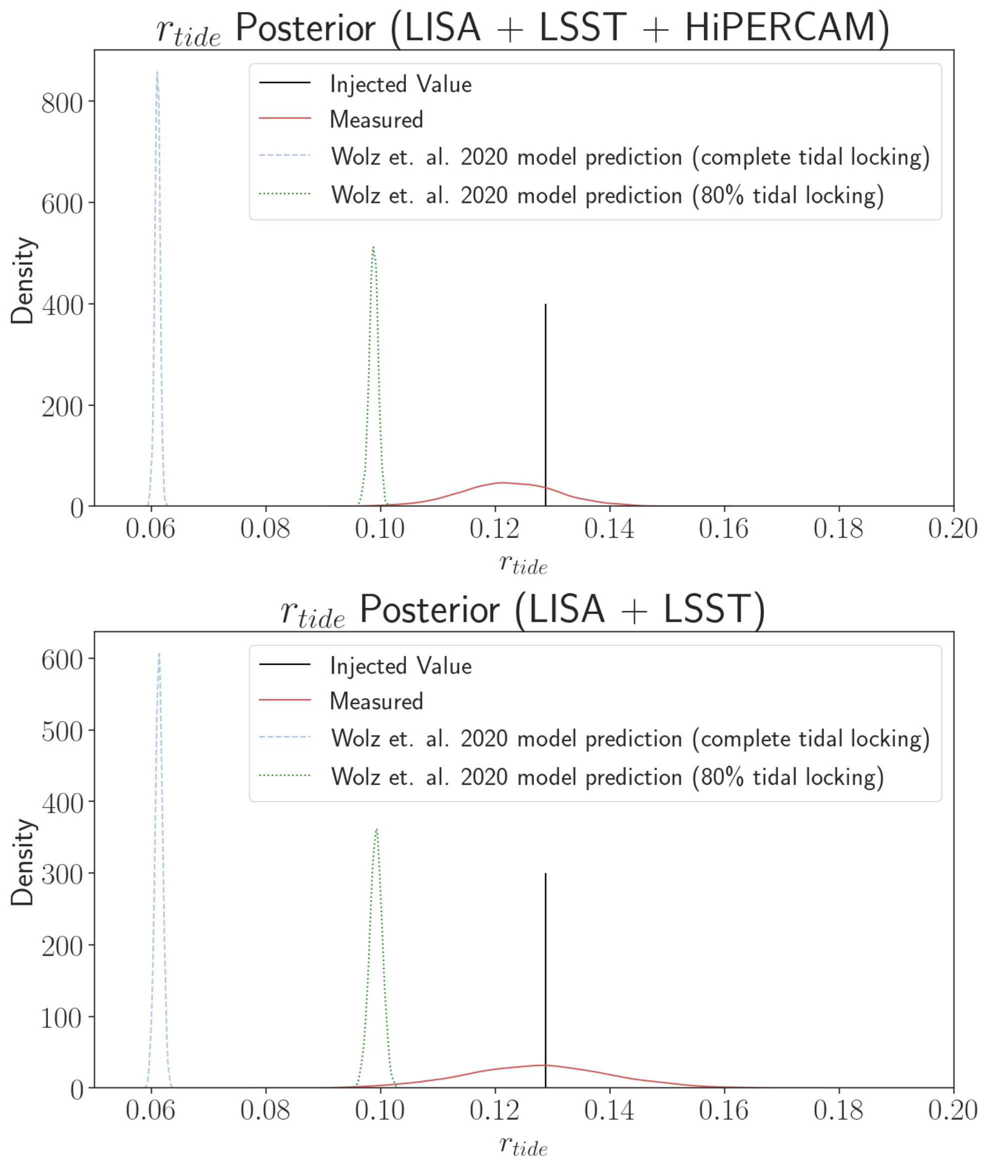

Figure 4.4: Multimessenger posteriors on r_{tide} with and without HiPERCAM data. In both plots, the rightmost, red, and solid curve shows our measured marginalized 1-D posterior for r_{tide}. The leftmost, light blue, and dashed posterior uses the sampled masses to compute moment of inertia from the relation in [199], which is used to compute r_{tide} using Equations 4.8 and 4.11 with $\eta = 1$. The center, green, and dotted posterior also uses the sampled masses to compute moment of inertia from [199] to compute r_{tide} using Equations 4.8 and 4.11, but with $\eta = 0.8$. The total inconsistency with $\eta = 1$ and evidence against $\eta = 0.8$ demonstrates that the multimessenger approach can be sufficient to observationally constrain constrain the nonzero temperature effects on moment of inertia, even when we relax the assumption of complete tidal locking and only use LISA and LSST data.

Table 4.2: Uncertainties in the orbital frequency derivative $\ddot{f}$ computed by fitting orbital phase measurements of given visit frequencies to a cubic polynomial. For comparison, the standard deviation in the predicted orbital $\ddot{f}$ from the LISA + LSST + HiPERCAM posterior samples was 2.8×10^{-31} s^{-3}. The left side value indicates the length of each observation chunk with a 3-second tme resolution and the top value indicates the frequency of such chunks. For example, the top left entry means that 1 hour of observation at the 3-second time resolution every year for 10 years (which corresponds to the cadence in Figure 4.2) would yield an $\ddot{f}$ uncertainty of 4.8×10^{-28} s^{-3}.

	10 yr, 1×/yr	10 yr, 10×/yr	20 yr, 1×/yr	20 yr, 10×/yr
1 hour	1.1×10^{-27} s^{-3}	4.3×10^{-28} s^{-3}	1.1×10^{-28} s^{-3}	3.9×10^{-29} s^{-3}
3 hours	6.3×10^{-28} s^{-3}	2.5×10^{-28} s^{-3}	6.2×10^{-29} s^{-3}	2.2×10^{-29} s^{-3}
5 hours	4.6×10^{-28} s^{-3}	1.8×10^{-29} s^{-3}	4.5×10^{-29} s^{-3}	1.6×10^{-29} s^{-3}

of such observation times and total baselines. For each length of observation time, we run `pocoMC` on injected HiPERCAM data alone for a single segment of 3s measurements for the given time and extract the marginalized uncertainty in the orbital phase. We use this same uncertainty for each observation time and fit a series of these with various frequencies and total baselines of these observations to a cubic polynomial and extract the uncertainty in $\ddot{f}$. The results are shown in Table 4.2.

4.6 Discussion

Our analysis of this source demonstrates that the multi-messenger approach breaks the $\mathcal{M}$–r_{tide} degeneracy, while breaking this degeneracy using a measurement of $\ddot{f}$ is likely infeasible. For a number of reasons, we believe this analysis extends to other detached, tidally locked DWDs. As mentioned earlier, $\ddot{f} \propto f^{19/3}$, and we have selected a test case of very high orbital frequency. Our version of ZTF J2243+5242 has a shorter period than any other detached DWD system found so far [47, 110, 111], and this particular system is barely detached, so we believe this to be on the high end for f and $\ddot{f}$. We expect lower frequency sources to have lower SNR in LISA, but the scaling is only $\rho_{\rm LISA} \propto f^{10/3}$, so at frequencies where LISA SNR drops off to make multi-messenger degeneracy breaking infeasible, $\ddot{f}$ will have shrunk substantially more, making the EM approach even less feasible.

Some DWDs such as PG 1159-036 [198] have been detected with at least one component exhibiting a surface temperature over 100,000 K, nearly an order of magnitude higher than that of ZTF J2243+5242, so one might consider the possibility of brighter sources yielding a much better phase measurement to measure $\ddot{f}$. The frequency constraint scales inversely with the SNR, which scales as $\rho \sim T^4 f_b(T)$. For these hotter sources, these visible photometric bands are on the tail of the blackbody distribution, so we have $f_b(T) \sim T^{-3}$. This means $\delta\ddot{f} \sim T^{-1}$, which is not a scaling strong enough to make a substantial difference.

As shown in Figure 4, our r_{tide} constraints can be sufficient to distinguish from moment of inertia relations that neglects nonzero temperature effects. These temperature dependent effects to these quasi-universal relations have been investigated in [36] and [186]. Multi-messenger observation could allow empirical testing of the deviations from these relations. Alternatively, if these relations were refined to accurately predict moment of inertia, we could instead use them to determine whether a tight DWD system is tidally locked.

4.7 Chapter 4 Conclusion

We used MCMC to compute posteriors for a simulated Galactic eclipsing DWD system with mock LISA, LSST and HiPERCAM data that is similar to ZTF J2243+5242 with an orbital period of six minutes. The addition of LISA data allowed the breaking of degeneracies in mass, distance, radius, and r_{tide}, the tidal contribution to the orbital frequency derivative $\dot{f}$. We demonstrate that masses and r_{tide} can be simultaneously measured to a precision that will allow us to constrain the non-zero temperature effects on the moments of inertia of the WDs. Without GW information from LISA, degeneracy breaking at a comparable level would not be possible even with dedicated 5-hour long HiPERCAM visits 10 times a year for 20 years.

This degeneracy could be alternatively broken from dedicated spectroscopy, which could constrain radial velocity, but this would require valuable time on a very large telescope like the Extremely Large Telescope (ELT), the Giant Megellan Telescope (GMT), or the Thirty Meter Telescope (TMT) [143], which are likely to be severely oversubscribed. Hence, it is unclear whether spectroscopy could be efficient for studying a large sample of DWDs. On the other hand, the multimessenger method we study in this work might identify many DWDs exhibiting interesting tidal effects on the orbital evolution, which will be justified follow-up targets for the very large telescopes.

Multi-messenger analysis appears key to disentangling the impact of tides from the chirp masses. The effect of tides is the dominant deviation from the binary evolution prediction from solely GW radiation, so it will be important to measure this to accurately model the evolution of these DWDs as they approach merger. Constraining the tidal effects themselves will also allow us to empirically test stellar model predictions of moment of inertia. As these predictions improve, we would be able to constrain the degree of tidal locking η. Joint efforts of the mHz-range GW community and the optical astronomy communities will be crucial for maximizing the science of Galactic DWDs in the next one or two decades.

4.8 Calibrations with HiPERCAM Observation on ZTF J2243+5242

We use our real HiPERCAM observation data of ZTF J2243+5242 to make our mock data as realistic as possible using our model. We perform a fit of the true data using our model to choose mock data parameters for our analysis and we perform a fit of the true noise estimates to calibrate our HiPERCAM noise.

4.8.1 Choosing Mock Data Parameters using HiPERCAM Data

The true HiPERCAM data is scaled relative to the brightness of a comparison star, so we do not use the data to model the temperature or luminosity distance, which scale the entire flux in each band. The data only lasts roughly an hour and a half, so we cannot reasonably use it to infer anything about the masses or r_{tide}. So we fix the masses, temperatures, and luminosity distance according to the SED fit in [46], and fit phase, period, radii, inclination, irradiation amplitude, and flux scaling factors for each band.

We compute posteriors in these parameters using the `MultiNest` sampler [76]. Our best fit is shown in Figure 4.5. The radii, inclination, and irradiation amplitude in this fit are listed in Table 4.1. Of note, the inclination is about 4.5 sigma above the result in [46] and the radius of the secondary white dwarf is about 2.5 sigma below the result in [46]. All other parameters are consistent. This difference is consistent with mild modeling differences that come from our simplifying assumptions, but we do not believe this will significantly affect the interpretation of our results.

4.8.2 Calibrating Mock HiPERCAM Noise using HiPERCAM Data

We used real HiPERCAM observations of ZTF J2243+5242 to calibrate our mock noise. For simplicity, we model our flux variance in each band σ_b^2 as a Poisson component plus a time-independent constant component:

$$\sigma_b^2 = \sigma_{\text{constant},b}^2 + k_b \phi_b, \tag{4.21}$$

where ϕ_b is the flux in band b, and $\sigma_{\text{constant},b}$ and k_b are the fit parameters. Noise from the real data had non-Poissonian time dependence due to factors like airmass, so the fit effectively averaged over these effects. A comparison between mock data using our best fit above and the fit noise and the true data is shown in Figure 4.6.

4.9 Reparameterization for DWD Parameter Inference with Tides

Our model is parameterized by 14 total parameters: 13 physical parameters that we described in Table 4.1 (the individual masses M_1 and M_2 are replaced with the chirp mass $\mathcal{M}$ and mass ratio q) and an additional dummy mass ratio q. This parameterization has numerous degeneracies as seen in 4.3, which made it difficult or impossible for many samplers to converge.

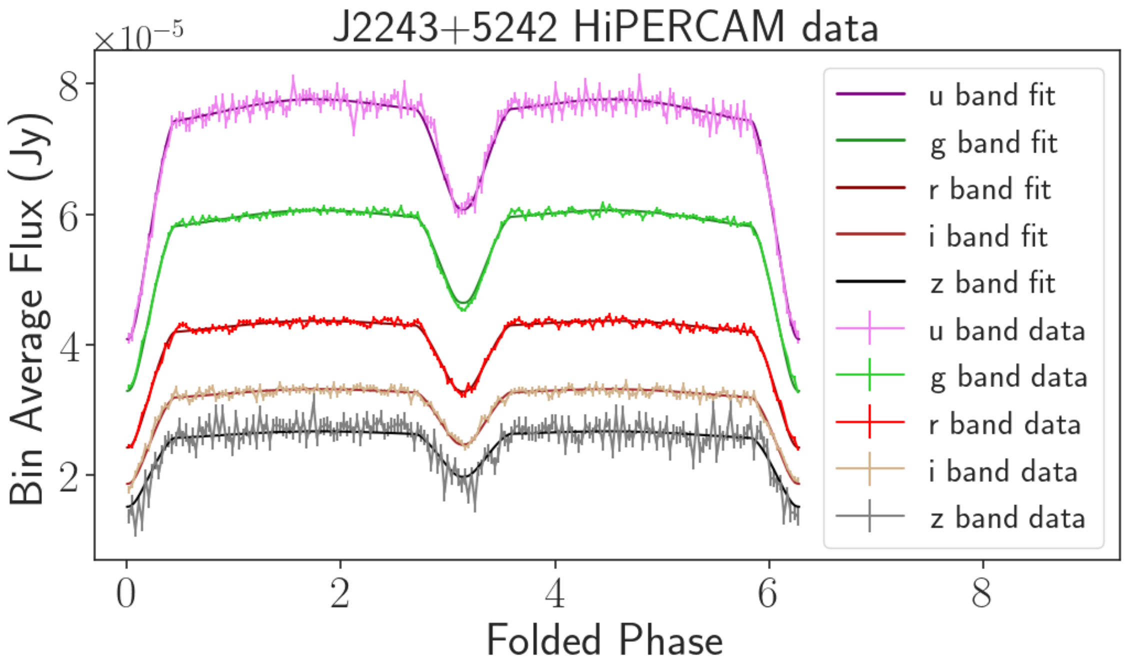

Figure 4.5: Our best fit to a 1.5 hour HiPERCAM observation of ZTF J2243+5242. The data is phase folded using the best fit orbital phase parameters and averaged into 200 equally size phase bins. The data with error bars is shown as the lighter colors, and the model fit is the solid darker curve. The radii, inclination, and irradiation amplitude from this fit are used for our main analysis and are shown in Table 4.1. The flux scaling factors are used to calibrate the mock noise, as detailed in section 4.8.2.

To solve this, we designed a reparameterization to remove the primary degeneracies, and this parameterization enabled us to get the accurate posteriors in 4.3. The $\mathcal{M}/r_{tide}$ degeneracy suggested that we define a so-called "effective tidal chirp mass" or $\mathcal{M}_{tide}$ as

$$\mathcal{M}_{tide} = \mathcal{M}(1 + r_{tide})^{3/5} \tag{4.22}$$

so that when you combine Equations 4.2a and 4.12 you get $\dot{f} \propto \mathcal{M}_{tide}^{5/3}$. The temperature, radii, and luminosity distance all contribute to the total fluxes from each star in the lightcurve model, so we address the resulting degeneracy by defining the coefficients C_1 and C_2 as

$$C_1 = \frac{T_1^4 R_1^2}{d_L^2}, \tag{4.23a}$$

$$C_2 = \frac{T_2^4 R_2^2}{d_L^2}. \tag{4.23b}$$

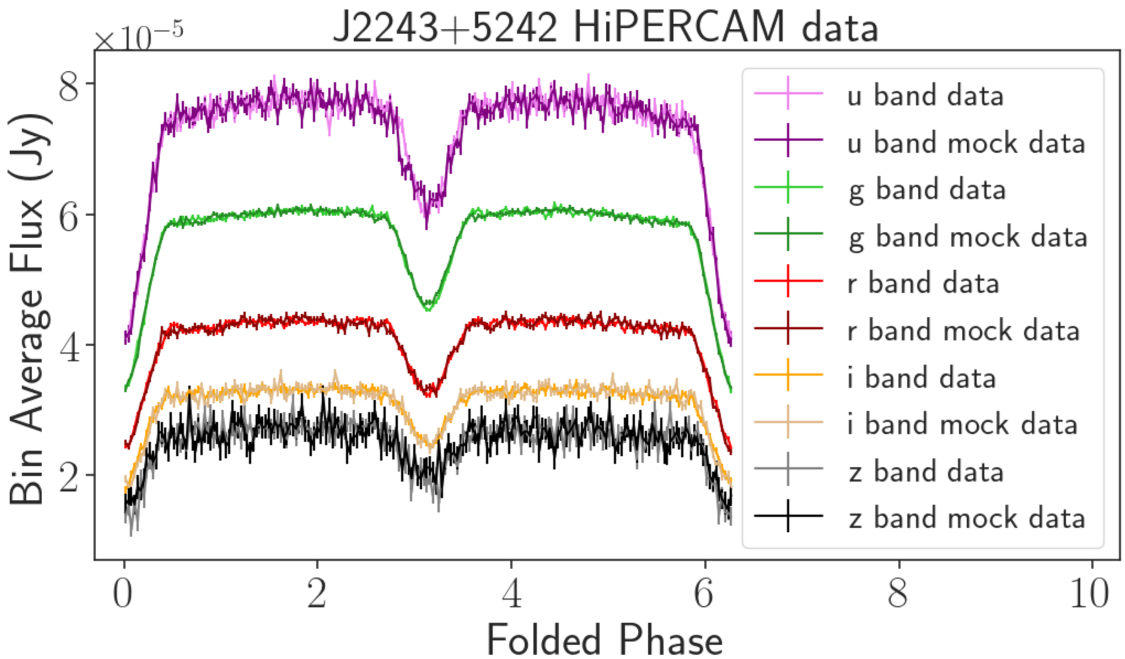

Figure 4.6: A comparison between data from a real 1.5 hour HiPERCAM observation of ZTF J2243+5242 and mock data model with error bars from Equation 4.21. Both are phase folded using the best fit orbital phase parameters and averaged into 200 equally size phase bins. The true data is shown in lighter colors and the mock data is shown in darker colors.

Finally we use the sum of the radii to make our parameter transformation bijective.

$$R = R_1 + R_2 \tag{4.24}$$

Our reparameterization is as follows:

$$(r_{\mathrm{tide}}, d_L, R_1, R_2) \to (\mathcal{M}_{tide}, R, C_1, C_2). \tag{4.25}$$

To preserve the prior when sampling in this new space, one needs to add the log determinant of the Jacobian of the transformation to the log prior. If we call the original "physical" parameters Θ_{phys} and the new parameters that we use for sampling $\Theta_{samp} = \mathcal{F}(\Theta_{phys})$, then the determinant of that Jacobian is

$$\det\big(J(\mathcal{F}^{-1}(\Theta_{samp}))\big) = \frac{5 d_L \mathcal{M}_{tide}^{2/3}}{12\mathcal{M}^{5/3} C_1 C_2}\left(\frac{B_1}{D_2} + \frac{B_2}{D_1}\right), \tag{4.26}$$

where the coefficients B's and D's are defined as follows:

$$B_1 = \frac{K_1 R}{D_1^2}, \tag{4.27a}$$

$$B_2 = \frac{K_2 R}{D_2^2}, \tag{4.27b}$$

$$D_1 = 1 + K_1, \tag{4.27c}$$

$$D_2 = 1 + K_2, \tag{4.27d}$$

$$K_1 = \sqrt{\frac{C_2}{C_1}} \left(\frac{T_1}{T_2}\right)^2, \tag{4.27e}$$

$$K_2 = \sqrt{\frac{C_2 1}{C_2}} \left(\frac{T_2}{T_1}\right)^2. \tag{4.27f}$$

Chapter 5

Outlook and Conclusion

All of the work in this thesis builds upon different subfields of the broad and rapidly evolving field of gravitational wave analysis. In this section, we discuss the outlook and future of many of these subfields, along with a few additional insights and ideas.

5.1 Faster Gravitational Wave Parameter Estimation

Like many fields in data science, gravitational wave parameter inference has the potential to be dramatically transformed by neural networks. Auto-regressive normalizing flows have been trained to build a bijective map from a Gaussian distribution to an accurate posterior distribution conditioned on strain data. Once such a model is trained, parameter inference on new data can be performed by just drawing samples from a Gaussian and applying this map conditioned on that new data, which only takes a few seconds [90]!

This sort of accomplishment does not render obsolete likelihood accelerating methods such as mode-by-mode relative binning, at least not yet. First of all, the speedup doesn't come for free: training such a flow can take from hours to months, and the flow is only accurate for the waveform model used in the training data. While this method has been successful on non-precessing waveforms like `IMRPhenomPv2`, it hasn't yet been demonstrated to work on precessing waveforms. In such cases, gathering posterior samples by evaluating a likelihood with mode-by-mode relative binning is a better bet.

Speedup from weeks to hours enables the feasibility of an analysis, but speedup from hours to seconds has additional benefits. Extremely rapid parameter estimation might enable electromagnetic followup, which might help catch transients like the gamma-ray burst or kilonova that followed the neutron star merger GW170817. But the most important information for such a follow-up is sky location, which can be immediately deduced from multiple detectors just by comparing arrival times, no detailed waveform modeling necessary. However, in a future where we might be detecting millions of events a year with a design-sensitivity Cosmic Explorer, we might want to determine which events are more likely to have electromagnetic counterparts, i.e. lower mass systems that are more likely to be neutron stars than black holes. In this scenario, fast inference of masses would be particularly helpful. If we become even more sensitive, we might seek specific follow-up on particularly rare events where the flags require more precision on parameters that are better modeled with more detailed models, such as those with precession and higher modes. In the future, neural networks may need to be designed, like the mode-by-mode relative binning algorithm, with careful analysis of the structure of higher-mode waveforms.

5.2 More New Gravitational Waveform Models

While Chapter 3 details the detectability of acceleration using our new waveform model, the model has not actually been tested on any real events. While we believe our best bet for detecting the effect of acceleration lies with next-generation detectors, it would be wise to test it on the loudest current LVK events, such as GW190814 or GW170817.

Next-generation detectors also leave us with a new problem when it comes to current gravitational wave data analysis pipelines. Most models treat the detector response coefficients (F_+ and $F_\times$ from Equation 1.24) as constants throughout the event. This is extremely accurate for sub-1 s events, like most binary black hole mergers as measured by LIGO, whose sensitivity goes down to about 8 Hz. This would not be accurate for the longer low-frequency signals that one may detect in Einstein Explorer, which plans to be sensitive down to roughly 2 Hz (cf. Figure 3.1). These might last minutes to hours, where the Earth has rotated, significantly altering the geometry of the detector relative to the source. With research mentees Druv Punjabi and Samyak Tiwari, I developed a way to alter waveform models to account for the rotation of the Earth to first order in the rotation rate of the Earth. I sought out a non-perturbative solution to this problem, and found via email correspondence that Neil Cornish had already solved this problem for massive black hole binaries with LISA, but hadn't published the result. Druv and I are continuing to determine a threshold for when such a model must be used to avoid biasing parameter inference.

5.3 Multi-messenger Noise Mitigation for LISA

In Chapter 4, I show that a multi-messenger approach enables the measurement of tidal effects or white dwarf structure that wouldn't be possible without expensive radial velocity measurements. I have also considered the possibility that a multi-messenger approach might also help address the problem of mitigating LISA confusion noise. As mentioned in Section 4.1, the dominant source of LISA noise at intermediate frequencies is confusion noise from galactic DWDs, which would exclude a target DWD if the goal is to analyze that DWD system. To mitigate this noise, the loudest sources would need to be measured and subtracted, leaving us only with noise due to the quieter unresolvable sources and the error in subtraction from the louder events.

In Chapter 4, we modeled the confusion noise for LISA based on [102], which only models the noise due to the quieter unresolvable sources, assuming all sources are perfectly subtracted. They fit a model to an iterative process performed on a sample population of galactic DWDs. First, they generate the strain from the sum of all sources and compute the signal-to-noise ratio (SNR) for each source assuming all other sources contribute to the noise PSD. They remove each source with SNR above some threshold ρ_0, and recompute SNR for each source only keeping the unsubtracted sources in the PSD. Subtracting sources from the PSD reduces the noise and increases the SNRs, so some more sources rise above the threshold and can be subtracted. This process is iterated until no additional sources rise above the SNR threshold. Finally, they fit a smooth function to the PSD of the remaining sources as the confusion noise fit.

Of course, each source is not perfectly subtracted, and one might instead try to compute the residuals like in [162], but these residuals themselves aren't completely accurate without confusion noise. Instead, you would need to perform a global fit, i.e. estimate the parameters of all sources in order to measure confusion noise, which can be quite difficult [183]. This is particularly challenging when each DWD is a complicated waveform with 8-9 parameters, and there are tens of millions of them overlapping [106].

This can be significantly ameliorated with EM information. The sky location, orbital frequency, and its first derivative can be measured quite well with a long-term EM measurement (the sky location significantly better than it can be measured with GWs). Fortunately, the frequency domain LISA waveform for the noise-independent channels E, A, and T can be decomposed as

$$h^{E,A,T}(f) = c_+ h_+^{E,A,T}(f) + c_\times h_\times^{E,A,T}(f), \tag{5.1}$$

where

$$c_+ = A_{\mathrm{GW}} e^{2i\phi_0} \left[-\frac{1+\cos^2\iota}{2}\cos(2\psi) + i\cos\iota\sin(2\psi) \right], \tag{5.2a}$$

$$c_\times = A_{\mathrm{GW}} e^{2i\phi_0} \left[-\frac{1+\cos^2\iota}{2}\sin(2\psi) - i\cos\iota\cos(2\psi) \right], \tag{5.2b}$$

Here A_{GW} is the amplitude of the gravitational wave, ι is the inclination angle of the binary, ψ is the roll angle, and ϕ_0 is the initial orbital phase.

Importantly, $h_+^{E,A,T}(f)$ and $h_\times^{E,A,T}(f)$ only depend of the sky location, orbital frequency, and its derivatives (in Chapter 4, we showed only the first derivative is likely measurable). So with perfect EM information on a source, $h_+^{E,A,T}(f)$ and $h_\times^{E,A,T}(f)$ are known, and fitting the GW counterpart just requires fitting the two complex numbers c_+ and $c_\times$.

In reality, we will not have such information on all sources as many will be obscured, but for this section we will assume that we do. The full LISA strain in a channel k contains instrumental noise, and signal from both resolvable and unresolvable sources (confusion noise), so it can be expressed as

$$
\begin{aligned}
d^k(f) &= n^k_{\text{instr}}(f) + \sum_{\substack{\alpha \\ \text{all DWDs}}} c_\alpha h^k_\alpha(f) \\
&= n^k_{\text{instr}}(f) + n^k_{\text{conf}}(f) + \sum_{\substack{\alpha \\ \text{resolvable DWDs}}} c_\alpha h^k_\alpha(f),
\end{aligned} \tag{5.3}
$$

where the α index denotes both the source and $+$ or $\times$.

If we know the EM measurable parameters and therefore all of the resolvable $h^k_\alpha(f)$s, then we can subtract a best fit to get a residual:

$$
\begin{aligned}
r^k(f) &= d^k(f) - \sum_\alpha c^{\text{best fit}}_\alpha h^k_\alpha(f) \\
&= n^k_{\text{total}}(f) + \sum_\alpha (c^{\text{true}}_\alpha - c^{\text{best fit}}_\alpha) h^k_\alpha(f).
\end{aligned} \tag{5.4}
$$

If we define an overlap

$$
\langle a|b\rangle = \sum_{k=E,A,T} \sum_f \frac{a^{k*}(f) b^k(f)}{\frac{T}{4} S_n(f)}, \tag{5.5}
$$

then we would like to find the values of $c^{\text{best fit}}_\alpha$ that minimize $\langle r|r\rangle$. After some algebra, this condition is equivalent to the following matrix equation:

$$
\langle h_\beta|d\rangle = \sum_\alpha c^{\text{best fit}}_\alpha \langle h_\beta|h_\alpha\rangle. \tag{5.6}
$$

We would need to invert this matrix which is $2N \times 2N$, where N is the number of resolvable signals. This seems tricky as $N \sim 200,000$ and ordinary matrix inversion has $\mathcal{O}(N^3)$ runtime, but fortunately, the matrix elements are

$$
\langle h_\beta|h_\alpha\rangle = \sum_{k=E,A,T} \sum_f \frac{h^{k*}_\beta(f) h^k_\alpha(f)}{\frac{T}{4} S_n(f)}, \tag{5.7}
$$

which is only non-zero if the frequencies of the two waveforms are very close, and LISA waveforms are very narrow in the frequency domain, their width dominated by Doppler broadening due to the motion of the detector around the Sun. This sparsity makes the matrix block tridiagonal, like the diagram in Figure 5.1, so it can be inverted using the Thomas algorithm, which has $\mathcal{O}(n_b m^3)$ runtime, where m is the width of the largest block and n_b is the number of blocks.

To investigate the feasibility of this approach, I wanted to estimate the sparsity of this matrix for actual LISA sources. Using the population model in [106], I generated an approximate frequency distribution of high SNR sources by generating hundreds of thousands of

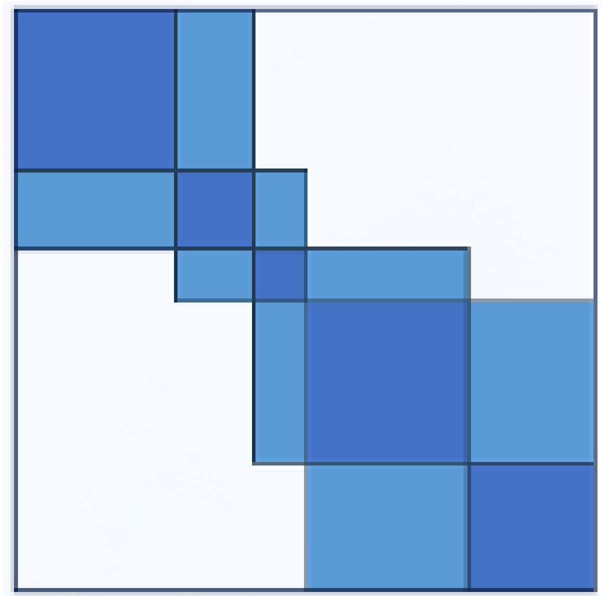

Figure 5.1: A depiction of the nonzero entries in a block tridiagonal matrix. The white space represents entries that are zero and the blue entries (light and dark) are nonzero. The side length of the largest dark blue square would be m.

sources, and removing those that had SNR < 7. I then fit a skew-normal distribution to the log frequency of these high frequency sources as shown in Figure 5.2.

As mentioned earlier, the frequency width of the signals is dominated by Doppler broadening, so I estimated that each signal had a frequency width of $(V_\oplus/c)f$, where $V_\oplus$ is the speed of the Earth (and therefore LISA) around the Sun. By drawing from the fit and assuming a frequency width of $(V_\oplus/c)f$, I found that the maximum number of overlapping signals was about $m = 80$, which would make the matrix inversion, and the global fit feasible.

Additionally, the cutoff of SNR $= 7$ was chosen somewhat arbitrarily, and existing work also uses arbitrary cutoffs between resolvable and unresolvable sources [102, 71]. With a method for a global fit of resolvable sources, I devised a method to determine an ideal cutoff.

If we apply such a method to an injection with an accurate DWD population we can compare an injected signal with a subtracted signal:

$$m^k_{\text{true}} = \sum_{\substack{\alpha \\ \text{all DWDs}}} c_\alpha h^k_\alpha(f), \tag{5.8a}$$

$$m^k_{\text{best fit}}(f) = \sum_{\substack{\alpha \\ \rho > \rho_{\text{thresh}}}} c^{\text{best fit}}_\alpha h^k_\alpha(f). \tag{5.8b}$$

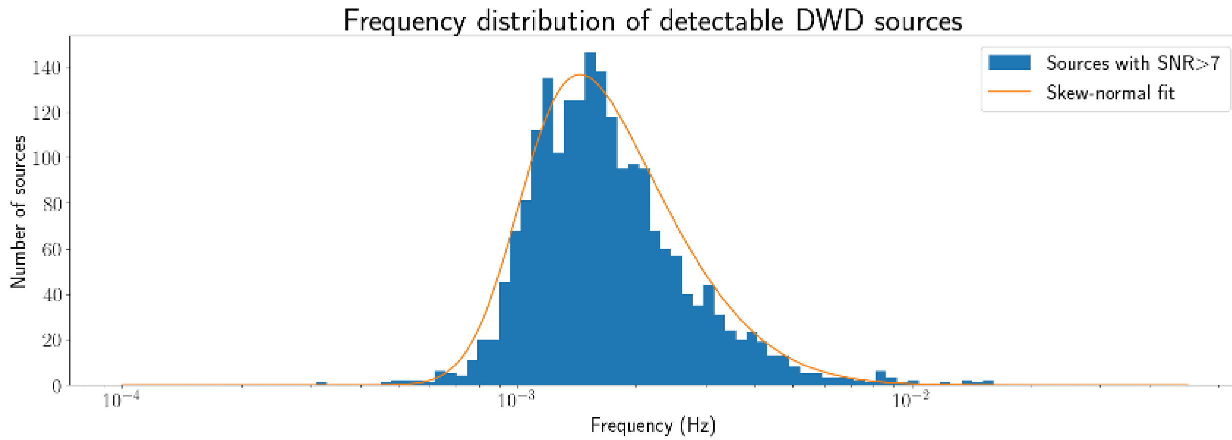

Figure 5.2: A histogram of the log frequencies of sources drawn from the DWD population model in [106], with a skew-normal distribution fit. The skew-normal distribution was used to draw frequencies of high SNR sources to estimate the maximum block size in the matrix in Equation 5.7.

We would like these to be as close as possible to optimize the SNR cutoff ρ_{thresh}:

$$\min_{\rho_{\text{thresh}}} \langle \delta m | \delta m \rangle, \tag{5.9}$$

where

$$\delta m^k(f) = m^k_{\text{true}} - m^k_{\text{best fit}}(f). \tag{5.10}$$

If ρ_{thresh} is too high, then you do not gather enough sources to fit the true signal, but if ρ_{thresh} is too low, you gather too many sources, and you begin to fit noise rather than sources, increasing your true residual δm. The best value comes from the optimization in Equation 5.9.

If we were to use this approach to fit confusion noise remaining after subtraction with EM information, then we would use many cores to compute the strain from the full set of roughly 2×10^7 DWDs using a population model. We would choose some starting value of ρ_{thresh} and treat all sources with SNR below this threshold (calculated with a noise PSD including all sources) as unresolvable and solve Equation 5.6 to get $c_\alpha^{\text{best fit}}$s for all resolvable sources. Like in the approach in [102], we can subtract the fit with these coefficients to get a new noise PSD, and this would raise the SNRs. Then we iterate, including more sources now above the starting ρ_{thresh}, recompute best fit $c_\alpha^{\text{best fit}}$s, get a new noise PSD, and continue until doing so adds no new detectable sources. The remaining noise PSD could be fit by a confusion noise model. At this point, we can compute the overlap $\langle \delta m | \delta m \rangle$ for this value of ρ_{thresh}. We would then need to iterate to optimize ρ_{thresh}, but multiple of these processes could be computed in parallel. This may take a while, but it would likely be feasible with modest computational resources, and it would yield a full confusion noise model for LISA with perfect EM information.

This approach provides both a computationally feasible way to perform global imperfect subtraction for LISA, simultaneously fitting all sources at once, which does not currently exist. It also provides a new criterion for picking an optimal cutoff SNR that can be used in a real LISA global fit. The problem is that it relies on all sources being detectable electromagnetically. This assumption is far from true, as many sources are too dim or blocked by dust extinctions, and the selection effects for LISA do not line up with those for EM detection. This approach may be adaptable to incomplete EM information, but it would likely not yield a simple matrix inversion. However, this approach does highlight that some of the hardest LISA information to fit (sky location and frequency) can be measured electromagnetically, and this observation may be used to yield some insights in tackling the LISA global fit problem.

5.4 Conclusion

Gravitational wave astronomy is a relatively new field, and one with an extremely bright (or as the gravitational wave community likes to say, loud) future. Ten years ago, we didn't have any experimental evidence that gravitational waves existed. Today, we've detected nearly 100 gravitational wave events, allowing us to test general relativity, constrain nuclear equations of state, and probe the population of extragalactic black holes—just a few of the many insights these observations have yielded. In ten years, we will launch a space-based gravitational wave detector around the Sun, which will detect gravitational waves from entirely new systems in our galaxy and potentially across the universe.

In Chapter 2, I presented mode-by-mode relative binning, a new gravitational wave likelihood approximation algorithm enabling fast and accurate parameter estimation for sources with precession effects and higher-than-quadrupole modes. In Chapter 3, I presented a new gravitational waveform model that includes the effect of center-of-mass acceleration, potentially allowing for the detection of heirarchical triple systems. In Chapter 4, I demonstrated how combining gravitational wave data from LISA with optical lightcurves from LSST and/or HiPERCAM enables measurement of how tidal interaction affects orbital evolution, which can constrain either a degree of tidal locking or enable empirical tests of white dwarf structure models with finite temperature effects.

Fast and accurate parameter inference, physically accurate and detailed waveform modeling, and multi-messenger astronomy will be extremely active and fruitful fields in the coming decades, especially with the planned ground-based and space-based gravitational wave detectors, as long as world governments continue to prioritize science.

Bibliography

[1] Elvis do A. Soares. *Constraining Effective Temperature, Mass and Radius of Hot White Dwarfs*. 2017. arXiv: 1701.02295 [astro-ph.SR].

[2] J Aasi et al. "Advanced LIGO". In: *Classical and Quantum Gravity* 32.7 (Mar. 2015), p. 074001. ISSN: 1361-6382. DOI: 10.1088/0264-9381/32/7/074001. URL: http://dx.doi.org/10.1088/0264-9381/32/7/074001.

[3] A. G. Abac et al. "Observation of Gravitational Waves from the Coalescence of a 2.5–4.5 $M_\odot$ Compact Object and a Neutron Star". In: *The Astrophysical Journal Letters* 970.2 (July 2024), p. L34. ISSN: 2041-8213. DOI: 10.3847/2041-8213/ad5beb. URL: http://dx.doi.org/10.3847/2041-8213/ad5beb.

[4] B P Abbott et al. "Characterization of transient noise in Advanced LIGO relevant to gravitational wave signal GW150914". In: *Classical and Quantum Gravity* 33.13 (June 2016), p. 134001. ISSN: 1361-6382. DOI: 10.1088/0264-9381/33/13/134001. URL: http://dx.doi.org/10.1088/0264-9381/33/13/134001.

[5] B. P. Abbott et al. "Gravitational Waves and Gamma-Rays from a Binary Neutron Star Merger: GW170817 and GRB 170817A". In: *The Astrophysical Journal Letters* 848.2 (Oct. 2017), p. L13. ISSN: 2041-8213. DOI: 10.3847/2041-8213/aa920c. URL: http://dx.doi.org/10.3847/2041-8213/aa920c.

[6] B. P. Abbott et al. "GW151226: Observation of Gravitational Waves from a 22-Solar-Mass Binary Black Hole Coalescence". In: *Physical Review Letters* 116.24 (June 2016). ISSN: 1079-7114. DOI: 10.1103/physrevlett.116.241103. URL: http://dx.doi.org/10.1103/PhysRevLett.116.241103.

[7] B. P. Abbott et al. "GW170814: A Three-Detector Observation of Gravitational Waves from a Binary Black Hole Coalescence". In: *Physical Review Letters* 119.14 (Oct. 2017). ISSN: 1079-7114. DOI: 10.1103/physrevlett.119.141101. URL: http://dx.doi.org/10.1103/PhysRevLett.119.141101.

[8] B. P. Abbott et al. "GW170817: Observation of Gravitational Waves from a Binary Neutron Star Inspiral". In: *Physical Review Letters* 119.16 (Oct. 2017). ISSN: 1079-7114. DOI: 10.1103/physrevlett.119.161101. URL: http://dx.doi.org/10.1103/PhysRevLett.119.161101.

[9] B. P. Abbott et al. "Multi-messenger Observations of a Binary Neutron Star Merger*". In: *The Astrophysical Journal Letters* 848.2 (Oct. 2017), p. L12. ISSN: 2041-8213. DOI: `10.3847/2041-8213/aa91c9`. URL: `http://dx.doi.org/10.3847/2041-8213/aa91c9`.

[10] R. Abbott et al. "GW190521: A Binary Black Hole Merger with a Total Mass of 150 $M_\odot$". In: *Physical Review Letters* 125.10 (Sept. 2020). ISSN: 1079-7114. DOI: `10.1103/physrevlett.125.101102`. URL: `http://dx.doi.org/10.1103/PhysRevLett.125.101102`.

[11] R. Abbott et al. "GW190814: Gravitational Waves from the Coalescence of a 23 Solar Mass Black Hole with a 2.6 Solar Mass Compact Object". In: *The Astrophysical Journal* 896.2 (June 2020), p. L44. ISSN: 2041-8213. DOI: `10.3847/2041-8213/ab960f`. URL: `http://dx.doi.org/10.3847/2041-8213/ab960f`.

[12] R. Abbott et al. "GWTC-3: Compact Binary Coalescences Observed by LIGO and Virgo during the Second Part of the Third Observing Run". In: *Phys. Rev. X* 13 (4 Dec. 2023), p. 041039. DOI: `10.1103/PhysRevX.13.041039`. URL: `https://link.aps.org/doi/10.1103/PhysRevX.13.041039`.

[13] Rich Abbott et al. "Open data from the first and second observing runs of Advanced LIGO and Advanced Virgo". In: *SoftwareX* 13 (Jan. 2021), p. 100658. ISSN: 2352-7110. DOI: `10.1016/j.softx.2021.100658`. URL: `http://dx.doi.org/10.1016/j.softx.2021.100658`.

[14] T. Accadia et al. "Virgo: a laser interferometer to detect gravitational waves". In: *JINST* 7 (2012), P03012. DOI: `10.1088/1748-0221/7/03/P03012`.

[15] "Advanced LIGO". In: *Classical and Quantum Gravity* 32.7 (Mar. 2015), p. 074001. DOI: `10.1088/0264-9381/32/7/074001`. URL: `https://dx.doi.org/10.1088/0264-9381/32/7/074001`.

[16] Gabriella Agazie et al. "The NANOGrav 15 yr Data Set: Evidence for a Gravitational-wave Background". In: *The Astrophysical Journal Letters* 951.1 (June 2023), p. L8. ISSN: 2041-8213. DOI: `10.3847/2041-8213/acdac6`. URL: `http://dx.doi.org/10.3847/2041-8213/acdac6`.

[17] LSST Science Collaboration et. al. *LSST Science Book, Version 2.0*. 2009. DOI: `10.48550/ARXIV.0912.0201`. URL: `https://arxiv.org/abs/0912.0201`.

[18] Pau Amaro-Seoane et al. *Laser Interferometer Space Antenna*. 2017. DOI: `10.48550/ARXIV.1702.00786`. URL: `https://arxiv.org/abs/1702.00786`.

[19] Fabio Antonini and Frederic A. Rasio. "Merging Black Hole Binaries in Galactic Nuclei: Implications for Advanced-LIGO Detections". In: *The Astrophysical Journal* 831.2 (Nov. 2016), p. 187. DOI: `10.3847/0004-637X/831/2/187`. URL: `https://dx.doi.org/10.3847/0004-637X/831/2/187`.

[20] Theocharis A. Apostolatos et al. *Spin-induced orbital precession and its modulation of the gravitational waveforms from merging binaries*. June 1994. URL: `https://journals.aps.org/prd/abstract/10.1103/PhysRevD.49.6274`.

[21] Gregory Ashton et al. "Bilby: A User-friendly Bayesian Inference Library for Gravitational-wave Astronomy". In: *The Astrophysical Journal Supplement Series* 241.2 (Apr. 2019), p. 27. ISSN: 1538-4365. DOI: `10.3847/1538-4365/ab06fc`. URL: `http://dx.doi.org/10.3847/1538-4365/ab06fc`.

[22] Stanislav Babak, Martin Hewitson, and Antoine Petiteau. *LISA Sensitivity and SNR Calculations*. 2021. DOI: `10.48550/ARXIV.2108.01167`. URL: `https://arxiv.org/abs/2108.01167`.

[23] Stas Babak and Antoine Petiteau. *LISA Data Challenge Manual - Institut National de Physique Nucléaire ...* Aug. 2020. URL: `https://lisa-ldc.lal.in2p3.fr/static/data/pdf/LDC-manual-002.pdf`.

[24] John G. Baker et al. "Gravitational-Wave Extraction from an Inspiraling Configuration of Merging Black Holes". In: *Physical Review Letters* 96.11 (Mar. 2006). ISSN: 1079-7114. DOI: `10.1103/physrevlett.96.111102`. URL: `http://dx.doi.org/10.1103/PhysRevLett.96.111102`.

[25] Pratyusava Baral et al. *Parameter estimation of gravitational-wave signals with frequency-dependent antenna responses and higher-modes*. 2025. arXiv: `2503.09627 [astro-ph.IM]`. URL: `https://arxiv.org/abs/2503.09627`.

[26] L. Barsotti et al. *LIGO-T1800042-v5: The A+ design curve — dcc.ligo.org*. `https://dcc.ligo.org/LIGO-T1800042/public`. [Accessed 24-09-2024].

[27] Imre Bartos et al. "Rapid and Bright Stellar-mass Binary Black Hole Mergers in Active Galactic Nuclei". In: *The Astrophysical Journal* 835.2 (Jan. 2017), p. 165. DOI: `10.3847/1538-4357/835/2/165`. URL: `https://dx.doi.org/10.3847/1538-4357/835/2/165`.

[28] Evan B. Bauer et al. "Masses of White Dwarf Binary Companions to Type Ia Supernovae Measured from Runaway Velocities". In: *The Astrophysical Journal Letters* 923.2 (Dec. 2021), p. L34. ISSN: 2041-8213. DOI: `10.3847/2041-8213/ac432d`. URL: `http://dx.doi.org/10.3847/2041-8213/ac432d`.

[29] Bence Bécsy et al. "How to Detect an Astrophysical Nanohertz Gravitational Wave Background". In: *The Astrophysical Journal* 959.1 (Nov. 2023), p. 9. ISSN: 1538-4357. DOI: `10.3847/1538-4357/ad09e4`. URL: `http://dx.doi.org/10.3847/1538-4357/ad09e4`.

[30] Eric C. Bellm et al. "The Zwicky Transient Facility: System Overview, Performance, and First Results". In: *Publications of the Astronomical Society of the Pacific* 131.995 (Dec. 2018), p. 018002. ISSN: 1538-3873. DOI: `10.1088/1538-3873/aaecbe`. URL: `http://dx.doi.org/10.1088/1538-3873/aaecbe`.

[31] Emanuele Berti et al. "Matched filtering and parameter estimation of ringdown waveforms". In: *Phys. Rev. D* 76 (10 Nov. 2007), p. 104044. DOI: 10.1103/PhysRevD.76.104044. URL: https://link.aps.org/doi/10.1103/PhysRevD.76.104044.

[32] Sylvia Biscoveanu et al. "Quantifying the effect of power spectral density uncertainty on gravitational-wave parameter estimation for compact binary sources". In: *Physical Review D* 102.2 (July 2020). DOI: 10.1103/physrevd.102.023008. URL: https://doi.org/10.1103%2Fphysrevd.102.023008.

[33] Luc Blanchet. "Gravitational Radiation from Post-Newtonian Sources and Inspiralling Compact Binaries". In: *Living Reviews in Relativity* 17.1 (Feb. 2014). DOI: 10.12942/lrr-2014-2. URL: https://doi.org/10.12942%2Flrr-2014-2.

[34] S. Bloemen et al. "Mass ratio from Doppler beaming and Rømer delay versus ellipsoidal modulation in the Kepler data of KOI-74⋆: Mass ratio of KOI-74". In: *Monthly Notices of the Royal Astronomical Society* 422.3 (Apr. 2012), pp. 2600–2608. ISSN: 0035-8711. DOI: 10.1111/j.1365-2966.2012.20818.x. URL: http://dx.doi.org/10.1111/j.1365-2966.2012.20818.x.

[35] Matteo Bonetti et al. "About gravitational-wave generation by a three-body system". In: *Classical and Quantum Gravity* 34.21 (Oct. 2017), p. 215004. DOI: 10.1088/1361-6382/aa8da5. URL: https://dx.doi.org/10.1088/1361-6382/aa8da5.

[36] K Boshkayev and H Quevedo. "Non-validity of I–Love–Q Relations for Hot White Dwarf Stars". In: *Monthly Notices of the Royal Astronomical Society* 478.2 (May 2018), pp. 1893–1899. ISSN: 1365-2966. DOI: 10.1093/mnras/sty1227. URL: http://dx.doi.org/10.1093/mnras/sty1227.

[37] Michael Boyle et al. "High-accuracy numerical simulation of black-hole binaries: Computation of the gravitational-wave energy flux and comparisons with post-Newtonian approximants". In: *Phys. Rev. D* 78 (10 Nov. 2008), p. 104020. DOI: 10.1103/PhysRevD.78.104020. URL: https://link.aps.org/doi/10.1103/PhysRevD.78.104020.

[38] Marica Branchesi et al. "Science with the Einstein Telescope: a comparison of different designs". In: *Journal of Cosmology and Astroparticle Physics* 2023.07 (July 2023), p. 068. ISSN: 1475-7516. DOI: 10.1088/1475-7516/2023/07/068. URL: http://dx.doi.org/10.1088/1475-7516/2023/07/068.

[39] Warren R. Brown et al. "The ELM Survey. VIII. Ninety-eight Double White Dwarf Binaries". In: *Astrophysical Journal* 889.1, 49 (Jan. 2020), p. 49. DOI: 10.3847/1538-4357/ab63cd. arXiv: 2002.00064 [astro-ph.SR].

[40] Johannes Buchner. "A statistical test for Nested Sampling algorithms". In: *Statistics and Computing* 26.1-2 (Jan. 2016), pp. 383–392. DOI: 10.1007/s11222-014-9512-y. arXiv: 1407.5459 [stat.CO].

[41] Johannes Buchner. "Collaborative Nested Sampling: Big Data versus Complex Physical Models". In: *PASP* 131.1004 (Oct. 2019), p. 108005. DOI: 10.1088/1538-3873/aae7fc. arXiv: 1707.04476 [stat.CO].

[42] Johannes Buchner. "UltraNest - a robust, general purpose Bayesian inference engine". In: *The Journal of Open Source Software* 6.60, 3001 (Apr. 2021), p. 3001. DOI: 10.21105/joss.03001. arXiv: 2101.09604 [stat.CO].

[43] A. Buonanno and T. Damour. "Effective one-body approach to general relativistic two-body dynamics". In: *Physical Review D* 59.8 (Mar. 1999). ISSN: 1089-4918. DOI: 10.1103/physrevd.59.084006. URL: http://dx.doi.org/10.1103/PhysRevD.59.084006.

[44] Alessandra Buonanno et al. "Comparison of post-Newtonian templates for compact binary inspiral signals in gravitational-wave detectors". In: *Phys. Rev. D* 80 (8 Oct. 2009), p. 084043. DOI: 10.1103/PhysRevD.80.084043. URL: https://link.aps.org/doi/10.1103/PhysRevD.80.084043.

[45] Kevin B. Burdge et al. "A Systematic Search of Zwicky Transient Facility Data for Ultracompact Binary LISA-detectable Gravitational-wave Sources". In: *The Astrophysical Journal* 905.1 (Dec. 2020), p. 32. ISSN: 1538-4357. DOI: 10.3847/1538-4357/abc261. URL: http://dx.doi.org/10.3847/1538-4357/abc261.

[46] Kevin B. Burdge et al. "An 8.8 Minute Orbital Period Eclipsing Detached Double White Dwarf Binary". In: *The Astrophysical Journal* 905.1 (Dec. 2020), p. L7. DOI: 10.3847/2041-8213/abca91. URL: https://doi.org/10.3847%2F2041-8213%2Fabca91.

[47] Kevin B. Burdge et al. "General relativistic orbital decay in a seven-minute-orbital-period eclipsing binary system". In: *Nature* 571.7766 (July 2019), pp. 528–531. DOI: 10.1038/s41586-019-1403-0. URL: https://doi.org/10.1038%2Fs41586-019-1403-0.

[48] M Cabero et al. "Blip glitches in Advanced LIGO data". In: *Classical and Quantum Gravity* 36.15 (July 2019), p. 155010. ISSN: 1361-6382. DOI: 10.1088/1361-6382/ab2e14. URL: http://dx.doi.org/10.1088/1361-6382/ab2e14.

[49] Juan Calderón Bustillo et al. "Tracking Black Hole Kicks from Gravitational-Wave Observations". In: *Physical Review Letters* 121.19 (Nov. 2018). ISSN: 1079-7114. DOI: 10.1103/physrevlett.121.191102. URL: http://dx.doi.org/10.1103/PhysRevLett.121.191102.

[50] M. Campanelli et al. "Accurate Evolutions of Orbiting Black-Hole Binaries without Excision". In: *Physical Review Letters* 96.11 (Mar. 2006). ISSN: 1079-7114. DOI: 10.1103/physrevlett.96.111101. URL: http://dx.doi.org/10.1103/PhysRevLett.96.111101.

[51] Priscilla Canizares et al. “Accelerated Gravitational Wave Parameter Estimation with Reduced Order Modeling”. In: *Physical Review Letters* 114.7 (Feb. 2015). ISSN: 1079-7114. DOI: 10.1103/physrevlett.114.071104. URL: http://dx.doi.org/10.1103/PhysRevLett.114.071104.

[52] Sean Carroll. *Spacetime and Geometry: An Introduction to General Relativity*. Benjamin Cummings, 2003. ISBN: 0805387323. URL: http://www.amazon.com/Spacetime-Geometry-Introduction-General-Relativity/dp/0805387323.

[53] Joan Centrella et al. “Black-hole binaries, gravitational waves, and numerical relativity”. In: *Rev. Mod. Phys.* 82 (4 Nov. 2010), pp. 3069–3119. DOI: 10.1103/RevModPhys.82.3069. URL: https://link.aps.org/doi/10.1103/RevModPhys.82.3069.

[54] Katie Chamberlain et al. “Frequency-domain waveform approximants capturing Doppler shifts”. In: *Phys. Rev. D* 99 (2 Jan. 2019), p. 024025. DOI: 10.1103/PhysRevD.99.024025. URL: https://link.aps.org/doi/10.1103/PhysRevD.99.024025.

[55] Debatri Chattopadhyay et al. “The impact of astrophysical priors on parameter inference for GW230529”. In: *Monthly Notices of the Royal Astronomical Society: Letters* 536.1 (Nov. 2024), pp. L19–L25. ISSN: 1745-3933. DOI: 10.1093/mnrasl/slae099. URL: http://dx.doi.org/10.1093/mnrasl/slae099.

[56] Katerina Chatziioannou et al. “On the properties of the massive binary black hole merger GW170729”. In: *Physical Review D* 100.10 (Nov. 2019). ISSN: 2470-0029. DOI: 10.1103/physrevd.100.104015. URL: http://dx.doi.org/10.1103/PhysRevD.100.104015.

[57] R. Chen et al. “Measuring Cosmological Parameters with Type Ia Supernovae in redMaGiC Galaxies”. In: *The Astrophysical Journal* 938.1 (Oct. 2022), p. 62. DOI: 10.3847/1538-4357/ac8b82. URL: https://doi.org/10.3847%2F1538-4357%2Fac8b82.

[58] Horng Sheng Chia et al. *Boxing Day Surprise: Higher Multipoles and Orbital Precession in GW151226*. 2021. arXiv: 2105.06486 [astro-ph.HE].

[59] N. Christensen and R. Meyer. “Parameter estimation with gravitational waves”. In: *Rev. Mod. Phys.* 94 (2 Apr. 2022), p. 025001. DOI: 10.1103/RevModPhys.94.025001. URL: https://doi.org/10.1103/RevModPhys.94.025001.

[60] A. Claret et al. “Gravity and limb-darkening coefficients for compact stars: DA, DB, and DBA eclipsing white dwarfs”. In: *Astronomy & Astrophysics* 634 (Feb. 2020), A93. ISSN: 1432-0746. DOI: 10.1051/0004-6361/201937326. URL: http://dx.doi.org/10.1051/0004-6361/201937326.

[61] Neil Cornish and Travis Robson. “Galactic binary science with the new LISA design”. In: *Journal of Physics: Conference Series* 840 (May 2017), p. 012024. ISSN: 1742-6596. DOI: 10.1088/1742-6596/840/1/012024. URL: http://dx.doi.org/10.1088/1742-6596/840/1/012024.

[62] Neil J. Cornish. *Fast Fisher Matrices and Lazy Likelihoods*. 2013. arXiv: `1007.4820 [gr-qc]`.

[63] Neil J. Cornish and Tyson B. Littenberg. "Tests of Bayesian model selection techniques for gravitational wave astronomy". In: *Physical Review D* 76.8 (Oct. 2007). DOI: `10.1103/physrevd.76.083006`. URL: `https://doi.org/10.1103%2Fphysrevd.76.083006`.

[64] Teviet Creighton. "Advanced LIGO: sources and astrophysics". In: *Classical and Quantum Gravity* 20.17 (Aug. 2003), S853. DOI: `10.1088/0264-9381/20/17/328`. URL: `https://dx.doi.org/10.1088/0264-9381/20/17/328`.

[65] C. Cutler et al. "The Last Three Minutes: Issues in Gravitational-Wave Measurements of Coalescing Compact Binaries". In: *Phys. Rev. Lett.* 70 (20 May 1993), p. 2984. DOI: `10.1103/PhysRevLett.70.2984`.

[66] Curt Cutler and Éanna E. Flanagan. "Gravitational waves from merging compact binaries: How accurately can one extract the binary's parameters from the inspiral waveform?" In: *Phys. Rev. D* 49 (6 Mar. 1994), pp. 2658–2697. DOI: `10.1103/PhysRevD.49.2658`. URL: `https://link.aps.org/doi/10.1103/PhysRevD.49.2658`.

[67] Liang Dai, Tejaswi Venumadhav, and Barak Zackay. *Parameter Estimation for GW170817 using Relative Binning*. 2018. arXiv: `1806.08793 [gr-qc]`.

[68] Thibault Damour. "Coalescence of two spinning black holes: An effective one-body approach". In: *Physical Review D* 64.12 (Nov. 2001). ISSN: 1089-4918. DOI: `10.1103/physrevd.64.124013`. URL: `http://dx.doi.org/10.1103/PhysRevD.64.124013`.

[69] Thibault Damour. "The General Relativistic Two Body Problem and the Effective One Body Formalism". In: *General Relativity, Cosmology and Astrophysics: Perspectives 100 years after Einstein's stay in Prague*. Ed. by Jiří Bičák and Tomáš Ledvinka. Cham: Springer International Publishing, 2014, pp. 111–145. ISBN: 978-3-319-06349-2. DOI: `10.1007/978-3-319-06349-2_5`. URL: `https://doi.org/10.1007/978-3-319-06349-2_5`.

[70] V S Dhillon et al. "HiPERCAM: a quintuple-beam, high-speed optical imager on the 10.4-m Gran Telescopio Canarias". In: *Monthly Notices of the Royal Astronomical Society* 507.1 (July 2021), pp. 350–366. ISSN: 1365-2966. DOI: `10.1093/mnras/stab2130`. URL: `http://dx.doi.org/10.1093/mnras/stab2130`.

[71] Matthew C. Digman and Neil J. Cornish. "LISA Gravitational Wave Sources in a Time-varying Galactic Stochastic Background". In: *The Astrophysical Journal* 940.1 (Nov. 2022), p. 10. DOI: `10.3847/1538-4357/ac9139`. URL: `https://doi.org/10.3847%2F1538-4357%2Fac9139`.

[72] Peter Eggleton and Ludmila Kiseleva. "An Empirical Condition for Stability of Hierarchical Triple Systems". In: *Astrophysical Journal* 455 (Dec. 1995), p. 640. DOI: `10.1086/176611`.

[73] Albert Einstein. “Näherungsweise Integration der Feldgleichungen der Gravitation”. In: *Sitzungsberichte der Königlich Preussischen Akademie der Wissenschaften* (Jan. 1916), pp. 688–696.

[74] Albert Einstein. “Über Gravitationswellen”. In: *Sitzungsberichte der Königlich Preussischen Akademie der Wissenschaften* (Jan. 1918), pp. 154–167.

[75] Will M. Farr et al. “The Mass Distribution of Stellar-Mass Black Holes”. In: *The Astrophysical Journal* 741.2 (Oct. 2011), p. 103. ISSN: 1538-4357. DOI: `10.1088/0004-637x/741/2/103`. URL: `http://dx.doi.org/10.1088/0004-637X/741/2/103`.

[76] F. Feroz, M. P. Hobson, and M. Bridges. “MultiNest: an efficient and robust Bayesian inference tool for cosmology and particle physics”. In: *Monthly Notices of the Royal Astronomical Society* 398.4 (Oct. 2009), pp. 1601–1614. ISSN: 1365-2966. DOI: `10.1111/j.1365-2966.2009.14548.x`. URL: `http://dx.doi.org/10.1111/j.1365-2966.2009.14548.x`.

[77] Lee S. Finn. “Detection, measurement, and gravitational radiation”. In: *Phys. Rev. D* 46 (12 Dec. 1992), pp. 5236–5249. DOI: `10.1103/PhysRevD.46.5236`. URL: `https://link.aps.org/doi/10.1103/PhysRevD.46.5236`.

[78] Daniel Finstad and Duncan A. Brown. “Fast Parameter Estimation of Binary Mergers for Multimessenger Follow-up”. In: *The Astrophysical Journal* 905.1 (Dec. 2020), p. L9. ISSN: 2041-8213. DOI: `10.3847/2041-8213/abca9e`. URL: `http://dx.doi.org/10.3847/2041-8213/abca9e`.

[79] Daniel Foreman-Mackey. “corner.py: Scatterplot matrices in Python”. In: *The Journal of Open Source Software* 1.2 (June 2016), p. 24. DOI: `10.21105/joss.00024`. URL: `https://doi.org/10.21105/joss.00024`.

[80] Jim Fuller and Dong Lai. “Dynamical tides in compact white dwarf binaries: helium core white dwarfs, tidal heating and observational signatures”. In: *Monthly Notices of the Royal Astronomical Society* 430.1 (Jan. 2013), pp. 274–287. ISSN: 0035-8711. DOI: `10.1093/mnras/sts606`. eprint: `https://academic.oup.com/mnras/article-pdf/430/1/274/3078317/sts606.pdf`. URL: `https://doi.org/10.1093/mnras/sts606`.

[81] Jim Fuller and Dong Lai. “Dynamical tides in compact white dwarf binaries: influence of rotation”. In: *Monthly Notices of the Royal Astronomical Society* 444.4 (Sept. 2014), pp. 3488–3500. ISSN: 0035-8711. DOI: `10.1093/mnras/stu1698`. URL: `http://dx.doi.org/10.1093/mnras/stu1698`.

[82] Toshifumi Futamase and Yousuke Itoh. “The Post-Newtonian Approximation for Relativistic Compact Binaries”. In: *Living Reviews in Relativity* 10.1 (2007), p. 2. DOI: `10.12942/lrr-2007-2`. URL: `https://doi.org/10.12942/lrr-2007-2`.

[83] Pablo Galaviz and Bernd Brügmann. “Characterization of the gravitational wave emission of three black holes”. In: *Phys. Rev. D* 83 (8 Apr. 2011), p. 084013. DOI: `10.1103/PhysRevD.83.084013`. URL: `https://link.aps.org/doi/10.1103/PhysRevD.83.084013`.

[84] Cecilio García-Quirós et al. "Multimode frequency-domain model for the gravitational wave signal from nonprecessing black-hole binaries". In: *Phys. Rev. D* 102.6 (2020), p. 064002. DOI: 10.1103/PhysRevD.102.064002. arXiv: 2001.10914 [gr-qc].

[85] Davide Gerosa et al. "A generalized precession parameter χ_p to interpret gravitational-wave data". In: *Physical Review D* 103.6 (Mar. 2021). ISSN: 2470-0029. DOI: 10.1103/physrevd.103.064067. URL: http://dx.doi.org/10.1103/PhysRevD.103.064067.

[86] Abhirup Ghosh et al. "Testing general relativity using golden black-hole binaries". In: *Phys. Rev. D* 94 (2 July 2016), p. 021101. DOI: 10.1103/PhysRevD.94.021101. URL: https://link.aps.org/doi/10.1103/PhysRevD.94.021101.

[87] Abhirup Ghosh et al. "Testing general relativity using gravitational wave signals from the inspiral, merger and ringdown of binary black holes". In: *Classical and Quantum Gravity* 35.1 (Nov. 2017), p. 014002. DOI: 10.1088/1361-6382/aa972e. URL: https://dx.doi.org/10.1088/1361-6382/aa972e.

[88] Yonadav Barry Ginat and Hagai B Perets. "Analytic modelling of binary-single encounters: non-thermal eccentricity distribution and gravitational-wave source formation". In: *Monthly Notices of the Royal Astronomical Society: Letters* 519.1 (Nov. 2022), pp. L15–L20. ISSN: 1745-3925. DOI: 10.1093/mnrasl/slac145. eprint: https://academic.oup.com/mnrasl/article-pdf/519/1/L15/54610664/slac145.pdf. URL: https://doi.org/10.1093/mnrasl/slac145.

[89] Philip B. Graff, Alessandra Buonanno, and B. S. Sathyaprakash. "Missing Link: Bayesian detection and measurement of intermediate-mass black-hole binaries". In: *Physical Review D* 92.2 (July 2015). ISSN: 1550-2368. DOI: 10.1103/physrevd.92.022002. URL: http://dx.doi.org/10.1103/PhysRevD.92.022002.

[90] Stephen R. Green, Christine Simpson, and Jonathan Gair. "Gravitational-wave parameter estimation with autoregressive neural network flows". In: *Physical Review D* 102.10 (Nov. 2020). ISSN: 2470-0029. DOI: 10.1103/physrevd.102.104057. URL: http://dx.doi.org/10.1103/PhysRevD.102.104057.

[91] Adrian S. Hamers and Todd A. Thompson. "Double Neutron Star Mergers from Hierarchical Triple-star Systems". In: *The Astrophysical Journal* 883.1 (Sept. 2019), p. 23. DOI: 10.3847/1538-4357/ab3b06. URL: https://dx.doi.org/10.3847/1538-4357/ab3b06.

[92] Wen-Biao Han et al. "Indication for a compact object next to a LIGO-Virgo binary black hole merger". In: (Jan. 2024). eprint: arXiv:2401.01743.

[93] Mark Hannam et al. "Simple Model of Complete Precessing Black-Hole-Binary Gravitational Waveforms". In: *Physical Review Letters* 113.15 (Oct. 2014). ISSN: 1079-7114. DOI: 10.1103/physrevlett.113.151101. URL: http://dx.doi.org/10.1103/PhysRevLett.113.151101.

[94] J. J. Hermes et al. "Two New Tidally Distorted White Dwarfs". In: *The Astrophysical Journal* 749.1 (Mar. 2012), p. 42. DOI: 10.1088/0004-637x/749/1/42. URL: https://doi.org/10.1088%2F0004-637x%2F749%2F1%2F42.

[95] S Hild et al. "Sensitivity studies for third-generation gravitational wave observatories". In: *Classical and Quantum Gravity* 28.9 (Apr. 2011), p. 094013. DOI: 10.1088/0264-9381/28/9/094013. URL: https://dx.doi.org/10.1088/0264-9381/28/9/094013.

[96] Francesco Iacovelli et al. "Forecasting the Detection Capabilities of Third-generation Gravitational-wave Detectors Using GWFAST". In: *The Astrophysical Journal* 941.2 (Dec. 2022), p. 208. DOI: 10.3847/1538-4357/ac9cd4. URL: https://dx.doi.org/10.3847/1538-4357/ac9cd4.

[97] Kohei Inayoshi et al. "Probing stellar binary black hole formation in galactic nuclei via the imprint of their center of mass acceleration on their gravitational wave signal". In: *Phys. Rev. D* 96 (6 Sept. 2017), p. 063014. DOI: 10.1103/PhysRevD.96.063014. URL: https://link.aps.org/doi/10.1103/PhysRevD.96.063014.

[98] N. Ivanova et al. "Common envelope evolution: where we stand and how we can move forward". In: *The Astronomy and Astrophysics Review* 21.1 (Feb. 2013). ISSN: 1432-0754. DOI: 10.1007/s00159-013-0059-2. URL: http://dx.doi.org/10.1007/s00159-013-0059-2.

[99] Piotr Jaranowski and Andrzej Królak. "Gravitational-Wave Data Analysis. Formalism and Sample Applications: The Gaussian Case". In: *Living Reviews in Relativity* 15.1 (2012), p. 4. DOI: 10.12942/lrr-2012-4. URL: https://doi.org/10.12942/lrr-2012-4.

[100] Chinmay Kalaghatgi, Mark Hannam, and Vivien Raymond. "Parameter estimation with a spinning multimode waveform model". In: *Physical Review D* 101.10 (May 2020). ISSN: 2470-0029. DOI: 10.1103/physrevd.101.103004. URL: http://dx.doi.org/10.1103/PhysRevD.101.103004.

[101] Minas Karamanis et al. *pocoMC: A Python package for accelerated Bayesian inference in astronomy and cosmology*. 2022. arXiv: 2207.05660 [astro-ph.IM]. URL: https://arxiv.org/abs/2207.05660.

[102] Nikolaos Karnesis et al. "Characterization of the stochastic signal originating from compact binary populations as measured by LISA". In: *Physical Review D* 104.4 (Aug. 2021). ISSN: 2470-0029. DOI: 10.1103/physrevd.104.043019. URL: http://dx.doi.org/10.1103/PhysRevD.104.043019.

[103] Sebastian Khan et al. "Frequency-domain gravitational waves from nonprecessing black-hole binaries. II. A phenomenological model for the advanced detector era". In: *Physical Review D* 93.4 (Feb. 2016). ISSN: 2470-0029. DOI: 10.1103/physrevd.93.044007. URL: http://dx.doi.org/10.1103/PhysRevD.93.044007.

[104] Sebastian Khan et al. "Including higher order multipoles in gravitational-wave models for precessing binary black holes". In: *Physical Review D* 101.2 (Jan. 2020). ISSN: 2470-0029. DOI: 10.1103/physrevd.101.024056. URL: http://dx.doi.org/10.1103/PhysRevD.101.024056.

[105] J. Koornneef et al. "Synthetic photometry and the calibration of the Hubble Space Telescope." In: *Highlights of Astronomy* 7 (Jan. 1986), pp. 833–843.

[106] Valeriya Korol et al. "Observationally driven Galactic double white dwarf population for LISA". In: *Monthly Notices of the Royal Astronomical Society* 511.4 (Feb. 2022), pp. 5936–5947. DOI: 10.1093/mnras/stac415. URL: https://doi.org/10.1093%2Fmnras%2Fstac415.

[107] Valeriya Korol et al. "Prospects for detection of detached double white dwarf binaries with Gaia, LSST and LISA". In: *Monthly Notices of the Royal Astronomical Society* 470.2 (May 2017), pp. 1894–1910. DOI: 10.1093/mnras/stx1285. URL: https://doi.org/10.1093%2Fmnras%2Fstx1285.

[108] Yoshihide Kozai. "Secular perturbations of asteroids with high inclination and eccentricity". In: *Astronomical Journal* 67 (1962), pp. 591–598. DOI: 10.1086/108790.

[109] K. Kuns et al. *CE-T2000017-v7: Cosmic Explorer Strain Sensitivity — dcc.cosmicexplorer.org*. https://dcc.cosmicexplorer.org/cgi-bin/DocDB/ShowDocument?docid=T2000017. [Accessed 24-09-2024].

[110] T Kupfer et al. "LISA verification binaries with updated distances from Gaia Data Release 2". In: *Monthly Notices of the Royal Astronomical Society* 480.1 (June 2018), pp. 302–309. ISSN: 1365-2966. DOI: 10.1093/mnras/sty1545. URL: http://dx.doi.org/10.1093/mnras/sty1545.

[111] Thomas Kupfer et al. *LISA Galactic binaries with astrometry from Gaia DR3*. 2024. arXiv: 2302.12719 [astro-ph.SR].

[112] Malcolm Lazarow, Nathaniel Leslie, and Liang Dai. *A Gravitational Waveform Model for Detecting Accelerating Inspiraling Binaries*. 2024. arXiv: 2401.04175 [gr-qc]. URL: https://arxiv.org/abs/2401.04175.

[113] Nathaniel Leslie, Liang Dai, and Kevin Burdge. *Double White Dwarf Tides with Multi-messenger Measurements*. 2025. arXiv: 2504.07919 [astro-ph.SR]. URL: https://arxiv.org/abs/2504.07919.

[114] Nathaniel Leslie, Liang Dai, and Geraint Pratten. "Mode-by-mode relative binning: Fast likelihood estimation for gravitational waveforms with spin-orbit precession and multiple harmonics". In: *Phys. Rev. D* 104.12 (2021), p. 123030. DOI: 10.1103/PhysRevD.104.123030. arXiv: 2109.09872 [astro-ph.IM].

[115] M.L. Lidov. "The evolution of orbits of artificial satellites of planets under the action of gravitational perturbations of external bodies". In: *Planetary and Space Science* 9.10 (1962), pp. 719–759.

[116] LIGO. *LIGO Gravitational Wave Open Science Center, Event List*.

[117] LIGO Scientific Collaboration. *LIGO Algorithm Library - LALSuite*. free software (GPL). 2018. DOI: 10.7935/GT1W-FZ16.

[118] LIGO Scientific Collaboration. "Observation of Gravitational Waves from a Binary Black Hole Merger". In: *Physical Review Letters* 116.6 (Feb. 2016). ISSN: 1079-7114. DOI: 10.1103/physrevlett.116.061102. URL: http://dx.doi.org/10.1103/PhysRevLett.116.061102.

[119] Tyson B. Littenberg and Ananthu K. Lali. "Have any LISA verification binaries been found?" In: (2024). arXiv: 2404.03046.

[120] Lionel London, Deirdre Shoemaker, and James Healy. "Modeling ringdown: Beyond the fundamental quasinormal modes". In: *Phys. Rev. D* 90 (12 Dec. 2014), p. 124032. DOI: 10.1103/PhysRevD.90.124032. URL: https://link.aps.org/doi/10.1103/PhysRevD.90.124032.

[121] Lionel London et al. "First Higher-Multipole Model of Gravitational Waves from Spinning and Coalescing Black-Hole Binaries". In: *Physical Review Letters* 120.16 (Apr. 2018). ISSN: 1079-7114. DOI: 10.1103/physrevlett.120.161102. URL: http://dx.doi.org/10.1103/PhysRevLett.120.161102.

[122] Wenbin Lu, Paz Beniamini, and Clément Bonnerot. "On the formation of GW190814". In: *Monthly Notices of the Royal Astronomical Society* 500.2 (Nov. 2020), pp. 1817–1832. ISSN: 0035-8711. DOI: 10.1093/mnras/staa3372. eprint: https://academic.oup.com/mnras/article-pdf/500/2/1817/34462808/staa3372.pdf. URL: https://doi.org/10.1093/mnras/staa3372.

[123] Jun Luo et al. "TianQin: a space-borne gravitational wave detector". In: *Classical and Quantum Gravity* 33.3 (Jan. 2016), p. 035010. ISSN: 1361-6382. DOI: 10.1088/0264-9381/33/3/035010. URL: http://dx.doi.org/10.1088/0264-9381/33/3/035010.

[124] D. M. Macleod et al. "GWpy: A Python package for gravitational-wave astrophysics". In: *SoftwareX* 13 (2021), p. 100657. ISSN: 2352-7110. DOI: 10.1016/j.softx.2021.100657. URL: https://www.sciencedirect.com/science/article/pii/S2352711021000029.

[125] Michele Maggiore. *Gravitational Waves. Vol. 1: Theory and Experiments*. Oxford University Press, 2007. ISBN: 978-0-19-171766-6. DOI: 10.1093/acprof:oso/9780198570745.001.0001.

[126] D. V. Martynov et al. "Sensitivity of the Advanced LIGO detectors at the beginning of gravitational wave astronomy". In: *Phys. Rev. D* 93 (11 June 2016), p. 112004. DOI: 10.1103/PhysRevD.93.112004. URL: https://link.aps.org/doi/10.1103/PhysRevD.93.112004.

[127] Maite Mateu-Lucena et al. *Adding harmonics to the interpretation of the black hole mergers of GWTC-1*. 2021. arXiv: 2105.05960 [gr-qc].

[128] P. F. L. Maxted. "ellc: A fast, flexible light curve model for detached eclipsing binary stars and transiting exoplanets". In: *Astronomy & Astrophysics* 591 (June 2016), A111. ISSN: 1432-0746. DOI: 10.1051/0004-6361/201628579. URL: http://dx.doi.org/10.1051/0004-6361/201628579.

[129] Barry McKernan et al. "Constraining Stellar-mass Black Hole Mergers in AGN Disks Detectable with LIGO". In: *The Astrophysical Journal* 866.1 (Oct. 2018), p. 66. DOI: 10.3847/1538-4357/aadae5. URL: https://dx.doi.org/10.3847/1538-4357/aadae5.

[130] Yohai Meiron, Bence Kocsis, and Abraham Loeb. "Detecting Triple Systems with Gravitational Wave Observations". In: *The Astrophysical Journal* 834.2 (Jan. 2017), p. 200. DOI: 10.3847/1538-4357/834/2/200. URL: https://dx.doi.org/10.3847/1538-4357/834/2/200.

[131] Soichiro Morisaki and Vivien Raymond. "Rapid parameter estimation of gravitational waves from binary neutron star coalescence using focused reduced order quadrature". In: *Physical Review D* 102.10 (Nov. 2020). ISSN: 2470-0029. DOI: 10.1103/physrevd.102.104020. URL: http://dx.doi.org/10.1103/PhysRevD.102.104020.

[132] Steven L. Morris and Stephen A. Naftilan. "The Equations of Ellipsoidal Star Variability Applied to HR 8427". In: *Astrophysical Journal* 419 (Dec. 1993), p. 344. DOI: 10.1086/173488.

[133] Elahesadat Naghib et al. "A Framework for Telescope Schedulers: With Applications to the Large Synoptic Survey Telescope". In: *The Astronomical Journal* 157.4 (Mar. 2019), p. 151. DOI: 10.3847/1538-3881/aafece. URL: https://doi.org/10.3847%2F1538-3881%2Faafece.

[134] Smadar Naoz. "The Eccentric Kozai-Lidov Effect and Its Applications". In: *Annual Review of Astronomy and Astrophysics* 54.Volume 54, 2016 (2016), pp. 441–489. ISSN: 1545-4282. DOI: https://doi.org/10.1146/annurev-astro-081915-023315. URL: https://www.annualreviews.org/content/journals/10.1146/annurev-astro-081915-023315.

[135] Smadar Naoz et al. "Secular dynamics in hierarchical three-body systems". In: *Monthly Notices of the Royal Astronomical Society* 431.3 (Mar. 2013), pp. 2155–2171. ISSN: 0035-8711. DOI: 10.1093/mnras/stt302. eprint: https://academic.oup.com/mnras/article-pdf/431/3/2155/4890577/stt302.pdf. URL: https://doi.org/10.1093/mnras/stt302.

[136] Alexander H. Nitz and Collin D. Capano. "GW190521 May Be an Intermediate-mass Ratio Inspiral". In: *The Astrophysical Journal* 907.1 (Jan. 2021), p. L9. ISSN: 2041-8213. DOI: 10.3847/2041-8213/abccc5. URL: http://dx.doi.org/10.3847/2041-8213/abccc5.

[137] Alexander H. Nitz et al. *3-OGC: Catalog of gravitational waves from compact-binary mergers*. 2021. arXiv: 2105.09151 [astro-ph.HE].

[138] Serguei Ossokine et al. "Multipolar effective-one-body waveforms for precessing binary black holes: Construction and validation". In: *Physical Review D* 102.4 (Aug. 2020). ISSN: 2470-0029. DOI: 10.1103/physrevd.102.044055. URL: http://dx.doi.org/10.1103/PhysRevD.102.044055.

[139] Benjamin J. Owen and B. S. Sathyaprakash. "Matched filtering of gravitational waves from inspiraling compact binaries: Computational cost and template placement". In: *Phys. Rev. D* 60 (2 June 1999), p. 022002. DOI: 10.1103/PhysRevD.60.022002. URL: https://link.aps.org/doi/10.1103/PhysRevD.60.022002.

[140] Benjamin J. Owen and B. S. Sathyaprakash. "Matched filtering of gravitational waves from inspiraling compact binaries: Computational cost and template placement". In: *Phys. Rev. D* 60 (2 June 1999), p. 022002. DOI: 10.1103/PhysRevD.60.022002. URL: https://link.aps.org/doi/10.1103/PhysRevD.60.022002.

[141] Feryal Özel et al. "The Black Hole Mass Distribution in the Galaxy". In: *The Astrophysical Journal* 725.2 (Dec. 2010), pp. 1918–1927. ISSN: 1538-4357. DOI: 10.1088/0004-637x/725/2/1918. URL: http://dx.doi.org/10.1088/0004-637X/725/2/1918.

[142] B. Paczynski. "Common Envelope Binaries". In: *Symposium - International Astronomical Union* 73 (1976), pp. 75–80. DOI: 10.1017/S0074180900011864.

[143] Paolo Padovani and Michele Cirasuolo. "The Extremely Large Telescope". In: *Contemporary Physics* 64.1 (Jan. 2023), pp. 47–64. ISSN: 1366-5812. DOI: 10.1080/00107514.2023.2266921. URL: http://dx.doi.org/10.1080/00107514.2023.2266921.

[144] S. Perlmutter et al. "Measurements of Ω and Λ from 42 High-Redshift Supernovae". In: *The Astrophysical Journal* 517.2 (June 1999), pp. 565–586. DOI: 10.1086/307221. URL: https://doi.org/10.1086%2F307221.

[145] P. C. Peters. "Gravitational Radiation and the Motion of Two Point Masses". In: *Phys. Rev.* 136 (4B Nov. 1964), B1224–B1232. DOI: 10.1103/PhysRev.136.B1224. URL: https://link.aps.org/doi/10.1103/PhysRev.136.B1224.

[146] P. C. Peters and J. Mathews. "Gravitational Radiation from Point Masses in a Keplerian Orbit". In: *Phys. Rev.* 131 (1 July 1963), pp. 435–440. DOI: 10.1103/PhysRev.131.435. URL: https://link.aps.org/doi/10.1103/PhysRev.131.435.

[147] Anthony L. Piro. "Inferring the Presence of Tides in Detached White Dwarf Binaries". In: *The Astrophysical Journal Letters* 885.1 (Oct. 2019), p. L2. ISSN: 2041-8213. DOI: 10.3847/2041-8213/ab44c4. URL: http://dx.doi.org/10.3847/2041-8213/ab44c4.

[148] Eric Poisson and Clifford M. Will. "Gravitational waves from inspiraling compact binaries: Parameter estimation using second-post-Newtonian waveforms". In: *Phys. Rev. D* 52 (2 July 1995), pp. 848–855. DOI: 10.1103/PhysRevD.52.848. URL: https://link.aps.org/doi/10.1103/PhysRevD.52.848.

[149] Eric Poisson and Clifford M. Will. *Gravity: Newtonian, Post-Newtonian, Relativistic*. Cambridge University Press, 2014. DOI: 10.1017/CBO9781139507486.

[150] Geraint Pratten et al. *Let's twist again: computationally efficient models for the dominant and sub-dominant harmonic modes of precessing binary black holes*. 2020. arXiv: 2004.06503 [gr-qc].

[151] Geraint Pratten et al. "Setting the cornerstone for a family of models for gravitational waves from compact binaries: The dominant harmonic for nonprecessing quasicircular black holes". In: *Phys. Rev. D* 102.6 (2020), p. 064001. DOI: 10.1103/PhysRevD.102.064001. arXiv: 2001.11412 [gr-qc].

[152] Frans Pretorius. "Evolution of Binary Black-Hole Spacetimes". In: *Physical Review Letters* 95.12 (Sept. 2005). ISSN: 1079-7114. DOI: 10.1103/physrevlett.95.121101. URL: http://dx.doi.org/10.1103/PhysRevLett.95.121101.

[153] M Punturo et al. "The third generation of gravitational wave observatories and their science reach". In: *Classical and Quantum Gravity* 27.8 (Apr. 2010), p. 084007. DOI: 10.1088/0264-9381/27/8/084007. URL: https://dx.doi.org/10.1088/0264-9381/27/8/084007.

[154] M. Punturo. *ET sensitivities page*. https://www.et-gw.eu/index.php/etsensitivities. [Accessed 24-09-2024].

[155] Michael Pürrer. "Frequency domain reduced order model of aligned-spin effective-one-body waveforms with generic mass ratios and spins". In: *Physical Review D* 93.6 (Mar. 2016). ISSN: 2470-0029. DOI: 10.1103/physrevd.93.064041. URL: http://dx.doi.org/10.1103/PhysRevD.93.064041.

[156] Hong Qi and Vivien Raymond. *PyROQ: a Python-based Reduced Order Quadrature Building Code for Fast Gravitational Wave Inference*. 2021. arXiv: 2009.13812 [gr-qc].

[157] Lisa Randall and Zhong-Zhi Xianyu. "A Direct Probe of Mass Density near Inspiraling Binary Black Holes". In: *The Astrophysical Journal* 878.2 (June 2019), p. 75. DOI: 10.3847/1538-4357/ab20c6. URL: https://dx.doi.org/10.3847/1538-4357/ab20c6.

[158] Lisa Randall and Zhong-Zhi Xianyu. "An Analytical Portrait of Binary Mergers in Hierarchical Triple Systems". In: *The Astrophysical Journal* 864.2 (Sept. 2018), p. 134. DOI: 10.3847/1538-4357/aad7fe. URL: https://dx.doi.org/10.3847/1538-4357/aad7fe.

[159] Alberto Rebassa-Mansergas et al. *J0526+5934: a peculiar ultra-short period double white dwarf*. 2024. arXiv: 2402.04443 [astro-ph.SR].

[160] David Reitze et al. *Cosmic Explorer: The U.S. Contribution to Gravitational-Wave Astronomy beyond LIGO*. 2019. arXiv: 1907.04833 [astro-ph.IM]. URL: https://arxiv.org/abs/1907.04833.

[161] Jakob Robnik and Uroš Seljak. "Kepler Data Analysis: Non-Gaussian Noise and Fourier Gaussian Process Analysis of Stellar Variability". In: *The Astronomical Journal* 159.5 (Apr. 2020), p. 224. ISSN: 1538-3881. DOI: 10.3847/1538-3881/ab8460. URL: http://dx.doi.org/10.3847/1538-3881/ab8460.

[162] Travis Robson and Neil Cornish. "Impact of galactic foreground characterization on a global analysis for the LISA gravitational wave observatory". In: *Classical and Quantum Gravity* 34.24 (Nov. 2017), p. 244002. DOI: 10.1088/1361-6382/aa9601. URL: https://dx.doi.org/10.1088/1361-6382/aa9601.

[163] Javier Roulet et al. "Binary black hole mergers from LIGO/Virgo O1 and O2: Population inference combining confident and marginal events". In: *Physical Review D* 102.12 (Dec. 2020). ISSN: 2470-0029. DOI: 10.1103/physrevd.102.123022. URL: http://dx.doi.org/10.1103/PhysRevD.102.123022.

[164] Javier Roulet et al. *On the Distribution of Effective Spins and Masses of Binary Black Holes from the LIGO and Virgo O1-O3a Observing Runs*. 2021. arXiv: 2105.10580 [astro-ph.HE].

[165] Javier Roulet et al. "Template bank for compact binary coalescence searches in gravitational wave data: A general geometric placement algorithm". In: *Phys. Rev. D* 99 (12 June 2019), p. 123022. DOI: 10.1103/PhysRevD.99.123022. URL: https://link.aps.org/doi/10.1103/PhysRevD.99.123022.

[166] Johan Samsing and Teva Ilan. "Double gravitational wave mergers". In: *Monthly Notices of the Royal Astronomical Society* 482.1 (Aug. 2018), pp. 30–39. ISSN: 0035-8711. DOI: 10.1093/mnras/sty2249. eprint: https://academic.oup.com/mnras/article-pdf/482/1/30/26145015/sty2249.pdf. URL: https://doi.org/10.1093/mnras/sty2249.

[167] Johan Samsing and Teva Ilan. "Topology of black hole binary–single interactions". In: *Monthly Notices of the Royal Astronomical Society* 476.2 (Jan. 2018), pp. 1548–1560. ISSN: 0035-8711. DOI: 10.1093/mnras/sty197. eprint: https://academic.oup.com/mnras/article-pdf/476/2/1548/24282700/sty197.pdf. URL: https://doi.org/10.1093/mnras/sty197.

[168] Johan Samsing, Morgan MacLeod, and Enrico Ramirez-Ruiz. "The Formation of Eccentric Compact Binary Inspirals and the Role of Gravitational Wave Emission in Binary–Single Stellar Encounters". In: *The Astrophysical Journal* 784.1 (Mar. 2014), p. 71. DOI: 10.1088/0004-637X/784/1/71. URL: https://dx.doi.org/10.1088/0004-637X/784/1/71.

[169] B. S. Sathyaprakash and Bernard F. Schutz. "Physics, Astrophysics and Cosmology with Gravitational Waves". In: *Living Reviews in Relativity* 12.1 (2009), p. 2. DOI: 10.12942/lrr-2009-2. URL: https://doi.org/10.12942/lrr-2009-2.

[170] Peter Scherbak and Jim Fuller. "White dwarf binaries suggest a common envelope efficiency $\alpha \sim 1/3$". In: *Monthly Notices of the Royal Astronomical Society* 518.3 (Nov. 2022), pp. 3966–3984. ISSN: 1365-2966. DOI: 10.1093/mnras/stac3313. URL: http://dx.doi.org/10.1093/mnras/stac3313.

[171] Patricia Schmidt, Mark Hannam, and Sascha Husa. "Towards models of gravitational waveforms from generic binaries: A simple approximate mapping between precessing and nonprecessing inspiral signals". In: *Physical Review D* 86.10 (Nov. 2012). ISSN: 1550-2368. DOI: 10.1103/physrevd.86.104063. URL: http://dx.doi.org/10.1103/PhysRevD.86.104063.

[172] Patricia Schmidt, Frank Ohme, and Mark Hannam. "Towards models of gravitational waveforms from generic binaries: II. Modelling precession effects with a single effective precession parameter". In: *Physical Review D* 91.2 (Jan. 2015). ISSN: 1550-2368. DOI: 10.1103/physrevd.91.024043. URL: http://dx.doi.org/10.1103/PhysRevD.91.024043.

[173] Patricia Schmidt et al. "Tracking the precession of compact binaries from their gravitational-wave signal". In: *Phys. Rev. D* 84 (2011), p. 024046. DOI: 10.1103/PhysRevD.84.024046. arXiv: 1012.2879 [gr-qc].

[174] S. Shah, G. Nelemans, and M. van der Sluys. "Using electromagnetic observations to aid gravitational-wave parameter estimation of compact binaries observed with LISA: II. The effect of knowing the sky position". In: *Astronomy & Astrophysics* 553 (May 2013), A82. ISSN: 1432-0746. DOI: 10.1051/0004-6361/201321123. URL: http://dx.doi.org/10.1051/0004-6361/201321123.

[175] S. Shah, M. van der Sluys, and G. Nelemans. "Using electromagnetic observations to aid gravitational-wave parameter estimation of compact binaries observed with LISA". In: *Astronomy & Astrophysics* 544 (Aug. 2012), A153. ISSN: 1432-0746. DOI: 10.1051/0004-6361/201219309. URL: http://dx.doi.org/10.1051/0004-6361/201219309.

[176] Feroz H. Shaik et al. "Impact of subdominant modes on the interpretation of gravitational-wave signals from heavy binary black hole systems". In: *Physical Review D* 101.12 (June 2020). ISSN: 2470-0029. DOI: 10.1103/physrevd.101.124054. URL: http://dx.doi.org/10.1103/PhysRevD.101.124054.

[177] Ken J. Shen et al. "Three Hypervelocity White Dwarfs in Gaia DR2: Evidence for Dynamically Driven Double-degenerate Double-detonation Type Ia Supernovae". In: *The Astrophysical Journal* 865.1 (Sept. 2018), p. 15. ISSN: 1538-4357. DOI: 10.3847/1538-4357/aad55b. URL: http://dx.doi.org/10.3847/1538-4357/aad55b.

[178] Rory Smith et al. *Bayesian inference for gravitational waves from binary neutron star mergers in third-generation observatories*. 2021. arXiv: 2103.12274 [gr-qc].

[179] Rory Smith et al. "Fast and accurate inference on gravitational waves from precessing compact binaries". In: *Physical Review D* 94.4 (Aug. 2016). ISSN: 2470-0029. DOI: 10.1103/physrevd.94.044031. URL: http://dx.doi.org/10.1103/PhysRevD.94.044031.

[180] Ulrich Sperhake. "The numerical relativity breakthrough for binary black holes". In: *Classical and Quantum Gravity* 32.12 (June 2015), p. 124011. DOI: 10.1088/0264-9381/32/12/124011. URL: https://dx.doi.org/10.1088/0264-9381/32/12/124011.

[181] Nicholas C. Stone, Brian D. Metzger, and Zoltán Haiman. "Assisted inspirals of stellar mass black holes embedded in AGN discs: solving the 'final au problem'". In: *Monthly Notices of the Royal Astronomical Society* 464.1 (Sept. 2016), pp. 946–954. ISSN: 0035-8711. DOI: 10.1093/mnras/stw2260. eprint: https://academic.oup.com/mnras/article-pdf/464/1/946/18512767/stw2260.pdf. URL: https://doi.org/10.1093/mnras/stw2260.

[182] R. Storn and K. Price. "Differential Evolution – A Simple and Efficient Heuristic for global Optimization over Continuous Spaces". In: *Journal of Global Optimization* 11 (1997), pp. 341–359.

[183] Stefan H. Strub et al. *Global Analysis of LISA Data with Galactic Binaries and Massive Black Hole Binaries*. 2024. arXiv: 2403.15318 [gr-qc]. URL: https://arxiv.org/abs/2403.15318.

[184] Nicola Tamanini and Camilla Danielski. "The gravitational-wave detection of exoplanets orbiting white dwarf binaries using LISA". In: *Nature Astronomy* 3 (July 2019), pp. 858–866. DOI: 10.1038/s41550-019-0807-y. arXiv: 1812.04330 [astro-ph.EP].

[185] Nicola Tamanini et al. "Peculiar acceleration of stellar-origin black hole binaries: Measurement and biases with LISA". In: *Phys. Rev. D* 101 (6 Mar. 2020), p. 063002. DOI: 10.1103/PhysRevD.101.063002. URL: https://link.aps.org/doi/10.1103/PhysRevD.101.063002.

[186] Andrew J Taylor, Kent Yagi, and Phil L Arras. "I–Love–Q relations for realistic white dwarfs". In: *Monthly Notices of the Royal Astronomical Society* 492.1 (Dec. 2019), pp. 978–992. ISSN: 1365-2966. DOI: 10.1093/mnras/stz3519. URL: http://dx.doi.org/10.1093/mnras/stz3519.

[187] Lucy M. Thomas, Patricia Schmidt, and Geraint Pratten. "New effective precession spin for modeling multimodal gravitational waveforms in the strong-field regime". In: *Physical Review D* 103.8 (Apr. 2021). ISSN: 2470-0029. DOI: 10.1103/physrevd.103.083022. URL: http://dx.doi.org/10.1103/PhysRevD.103.083022.

[188] Massimo Tinto and Sanjeev V. Dhurandhar. "Time-Delay Interferometry". In: *Living Reviews in Relativity* 8.1 (July 2005). DOI: 10.12942/lrr-2005-4. URL: https://doi.org/10.12942%2Flrr-2005-4.

[189] Avinash Tiwari et al. "Accelerated binary black holes in globular clusters: forecasts and detectability in the era of space-based gravitational-wave detectors". In: *Monthly Notices of the Royal Astronomical Society* 527.3 (Dec. 2023), pp. 8586–8597. ISSN: 0035-8711. DOI: 10.1093/mnras/stad3749. eprint: https://academic.oup.com/mnras/article-pdf/527/3/8586/54646177/stad3749.pdf. URL: https://doi.org/10.1093/mnras/stad3749.

[190] Silvia Toonen, Adrian Hamers, and Simon Portegies Zwart. "The evolution of hierarchical triple star-systems". In: *Computational Astrophysics and Cosmology* 3.1 (2016), p. 6. DOI: 10.1186/s40668-016-0019-0. URL: https://doi.org/10.1186/s40668-016-0019-0.

[191] Vijay Varma, Maximiliano Isi, and Sylvia Biscoveanu. "Extracting the Gravitational Recoil from Black Hole Merger Signals". In: *Physical Review Letters* 124.10 (Mar. 2020). ISSN: 1079-7114. DOI: 10.1103/physrevlett.124.101104. URL: http://dx.doi.org/10.1103/PhysRevLett.124.101104.

[192] Vijay Varma et al. "Surrogate models for precessing binary black hole simulations with unequal masses". In: *Physical Review Research* 1.3 (Oct. 2019). ISSN: 2643-1564. DOI: 10.1103/physrevresearch.1.033015. URL: http://dx.doi.org/10.1103/PhysRevResearch.1.033015.

[193] Tejaswi Venumadhav et al. "New search pipeline for compact binary mergers: Results for binary black holes in the first observing run of Advanced LIGO". In: *Phys. Rev. D* 100.2 (2019), p. 023011. DOI: 10.1103/PhysRevD.100.023011. arXiv: 1902.10341 [astro-ph.IM].

[194] Aditya Vijaykumar et al. "Waltzing Binaries: Probing the Line-of-sight Acceleration of Merging Compact Objects with Gravitational Waves". In: *The Astrophysical Journal* 954.1 (Aug. 2023), p. 105. DOI: 10.3847/1538-4357/acd77d. URL: https://dx.doi.org/10.3847/1538-4357/acd77d.

[195] J. Weber. "Gravitational Radiation". In: *Phys. Rev. Lett.* 18 (13 Mar. 1967), pp. 498–501. DOI: 10.1103/PhysRevLett.18.498. URL: https://link.aps.org/doi/10.1103/PhysRevLett.18.498.

[196] B. Willems et al. "Eccentric Double White Dwarfs as LISA Sources in Globular Clusters". In: *The Astrophysical Journal* 665.1 (July 2007), pp. L59–L62. ISSN: 1538-4357. DOI: 10.1086/521049. URL: http://dx.doi.org/10.1086/521049.

[197] B. Willke et al. "The GEO 600 gravitational wave detector". In: *Class. Quant. Grav.* 19 (2002). Ed. by D. G. Blair, pp. 1377–1387. DOI: 10.1088/0264-9381/19/7/321.

[198] D. E. Winget et al. "A measurement of secular evolution in the pre-white dwarf star PG 1159-035." In: *Astrophysical Journal* 292 (May 1985), pp. 606–613. DOI: 10.1086/163193.

[199] Anna Wolz et al. "Measuring individual masses of binary white dwarfs with space-based gravitational-wave interferometers". In: *Monthly Notices of the Royal Astronomical Society: Letters* 500.1 (Nov. 2020), pp. L52–L56. ISSN: 1745-3933. DOI: 10.1093/mnrasl/slaa183. URL: http://dx.doi.org/10.1093/mnrasl/slaa183.

[200] Kaze W K Wong, Vishal Baibhav, and Emanuele Berti. "Binary radial velocity measurements with space-based gravitational-wave detectors". In: *Monthly Notices of the Royal Astronomical Society* 488.4 (July 2019), pp. 5665–5670. ISSN: 0035-8711. DOI: 10.1093/mnras/stz2077. eprint: https://academic.oup.com/mnras/article-pdf/488/4/5665/29191166/stz2077.pdf. URL: https://doi.org/10.1093/mnras/stz2077.

[201] Zeyuan Xuan, Peng Peng, and Xian Chen. "Degeneracy between mass and peculiar acceleration for the double white dwarfs in the LISA band". In: *Monthly Notices of the Royal Astronomical Society* 502.3 (Feb. 2021), pp. 4199–4209. ISSN: 0035-8711. DOI: 10.1093/mnras/stab331. eprint: https://academic.oup.com/mnras/article-pdf/502/3/4199/36338765/stab331.pdf. URL: https://doi.org/10.1093/mnras/stab331.

[202] Y. Yang et al. "AGN Disks Harden the Mass Distribution of Stellar-mass Binary Black Hole Mergers". In: *The Astrophysical Journal* 876.2 (May 2019), p. 122. DOI: 10.3847/1538-4357/ab16e3. URL: https://dx.doi.org/10.3847/1538-4357/ab16e3.

[203] Peter Yoachim et al. *LSST/rubin_sim: V1.3.3*. Oct. 2023. URL: https://zenodo.org/records/10028614.

[204] Nicolás Yunes, M. Coleman Miller, and Jonathan Thornburg. "Effect of massive perturbers on extreme mass-ratio inspiral waveforms". In: *Phys. Rev. D* 83 (4 Feb. 2011), p. 044030. DOI: 10.1103/PhysRevD.83.044030. URL: https://link.aps.org/doi/10.1103/PhysRevD.83.044030.

[205] Barak Zackay, Liang Dai, and Tejaswi Venumadhav. *Relative Binning and Fast Likelihood Evaluation for Gravitational Wave Parameter Estimation*. 2018. arXiv: 1806.08792 [astro-ph.IM].

[206] Barak Zackay, Liang Dai, and Tejaswi Venumadhav. "Relative Binning and Fast Likelihood Evaluation for Gravitational Wave Parameter Estimation". In: *arXiv e-prints*, arXiv:1806.08792 (June 2018), arXiv:1806.08792. DOI: 10.48550/arXiv.1806.08792. arXiv: 1806.08792 [astro-ph.IM].

[207] Barak Zackay et al. "Detecting gravitational waves in data with non-stationary and non-Gaussian noise". In: *Phys. Rev. D* 104 (6 Sept. 2021), p. 063034. DOI: 10.1103/PhysRevD.104.063034. URL: https://link.aps.org/doi/10.1103/PhysRevD.104.063034.

[208] Barak Zackay et al. "Highly spinning and aligned binary black hole merger in the Advanced LIGO first observing run". In: *Phys. Rev. D* 100.2 (2019), p. 023007. DOI: 10.1103/PhysRevD.100.023007. arXiv: 1902.10331 [astro-ph.HE].